arXiv:2509.02663v2 [cond-mat.str-el] 25 Feb 2026

Semi-Dirac spin liquids and frustrated quantum magnetism on the trellis lattice

Sourin Chatterjee,[1] Atanu Maity,[2,1] Janik Potten,[2] Tobias Müller,[2] Andreas Feuerpfeil,[2] Ronny Thomale,[2,1] Karlo Penc,[3,1] Harald O. Jeschke,[4,1] Rhine Samajdar,[5,6,*] and Yasir Iqbal[1,†]

[1] *Department of Physics and Quantum Centre of Excellence for Diamond and Emergent Materials (QuCenDiEM), Indian Institute of Technology Madras, Chennai 600036, India*

[2] *Institut für Theoretische Physik und Astrophysik and Würzburg-Dresden Cluster of Excellence ct.qmat, Julius-Maximilians-Universität Würzburg, Am Hubland, Campus Süd, Würzburg 97074, Germany*

[3] *Institute for Solid State Physics and Optics, HUN-REN Wigner Research Centre for Physics, P.O. Box 49, H-1525 Budapest, Hungary*

[4] *Research Institute for Interdisciplinary Science, Okayama University, Okayama 700-8530, Japan*

[5] *Department of Physics, Princeton University, Princeton, New Jersey 08544, USA*

[6] *Princeton Center for Theoretical Science, Princeton University, Princeton, New Jersey 08544, USA*

(Dated: February 26, 2026)

Geometrical frustration in quantum magnets provides a fertile setting for unconventional phases of matter, including quantum spin liquids (QSLs). The trellis lattice, with its complex site arrangements and edge-sharing triangular motifs, presents a promising platform for such physics. In this work, we undertake a comprehensive classification of all fully symmetric QSLs on the trellis lattice using the projective symmetry group approach within the Abrikosov-fermion representation. We find 7 U(1) and 25 $\mathbb{Z}_2$ short-ranged *Ansätze* and analyze the phase diagram in the mean-field parameter space, uncovering both gapped and Dirac QSLs as well as a semi-Dirac spin liquid that emerges at the level of projective symmetry group classification and mean-field band structure, in which the spinon dispersion is linear along one momentum direction but quadratic along the orthogonal one. We demonstrate that such dispersions can occur only at high-symmetry points in the Brillouin zone with C_{2v} little groups and analyze their characteristic correlation signatures. Moreover, by optimizing over all symmetry-allowed mean-field states, we map out a phase diagram—featuring six distinct phases—of the nearest-neighbor Heisenberg Hamiltonian on the trellis lattice. Among these, we find four quasi-one-dimensional QSL phases, one dimer phase, and one Dirac QSL phase. Going beyond mean field, we also assess equal-time and dynamical spin structure factors of these phases using density-matrix renormalization group and Keldysh pseudofermion functional renormalization group calculations and compare qualitative momentum-space features of these spectra with those obtained at the mean-field level. Finally, we identify four cuprate and vanadate compounds as promising experimental realizations and provide spectroscopic predictions, based on first-principles Hamiltonians, as a guide for future neutron-scattering studies on these materials.

I. INTRODUCTION

The investigation of magnetic properties of quantum materials has long been a central focus in condensed matter physics, particularly the intricate relationship between lattice topology and quantum orders [1, 2]. A key aspect of this interplay arises when specific geometric arrangements of magnetic moments give rise to *competing* interactions—an effect known as geometric frustration. Lattices containing triangular motifs serve as paradigmatic examples of such frustration, often exhibiting complex magnetic behavior such as spin-spiral states, noncoplanar orders, and, in certain cases, extensive ground-state degeneracy that suppresses conventional long-range magnetic order [3–11].

Generically, quantum fluctuations at low temperature tend to destabilize classical magnetic order, pushing the system into a quantum paramagnetic regime. When such fluctuations are sufficiently strong—as alluded to above—they can lead to exotic phases of matter known as quantum spin liquids (QSLs), characterized by the absence of any spontaneous symmetry breaking even at zero temperature [12–14]. In recent years, the study of frustrated magnets has garnered significant attention, fueled by both theoretical and experimental evidence for QSL behavior in various two- and three-dimensional lattice geometries, including kagome, triangular, and pyrochlore structures [15–21].

Two-dimensional (2D) Heisenberg antiferromagnets on Archimedean lattices provide a rich platform for exploring the influence of lattice geometry and quantum fluctuations on magnetic phases [22–25]. Of the eleven Archimedean lattices, four—namely the square [26–28], honeycomb [29, 30], square-octagon, and square-hexagon-dodecagon lattices—are unfrustrated and, as expected, support long-range magnetic order for the Heisenberg model with only nearest-neighbor interactions. The remaining seven incorporate geometrical frustration due to their corner- or edge-sharing triangular motifs. Among these, considering again nearest-neighbor antiferromagnetic couplings of equal strength,

* rhine_samajdar@princeton.edu
† yiqbal@physics.iitm.ac.in

the Shastry-Sutherland [31] and triangular [32–34] lattices maintain long-range order despite strong frustration, whereas the kagome and star lattices host magnetically disordered ground states. The remaining three lattices—maple leaf, trellis, and bounce—lie in an intermediate regime. In this list of candidates, the maple-leaf lattice, in particular, has been intensely studied in recent years [35–38], revealing a variety of exotic phases, including an exact dimerized ground state [39] and possible quantum spin liquid behavior [40–43].

In contrast, the trellis lattice has remained largely unexplored [44], despite its complex site arrangements and edge-sharing triangular connectivity that can host unconventional magnetic structures not typically found in simpler geometries. An early study employing various numerical and analytical techniques revealed a range of diverse magnetic and nonmagnetic phases on the trellis lattice [45]. It identified a nondegenerate valence-bond solid state in the dimer limit and a subextensively degenerate (gapless) Majumdar-Ghosh-like phase in the regime of weakly coupled zigzag chains, both of which have a finite singlet-triplet gap. Between these two extremes, gapless magnetically ordered phases emerge. Specifically, antiferromagnetic order appears near the honeycomb-lattice limit, while a helical state with incommensurate spin correlations develops along the chains when all three magnetic interactions compete. Extensions of this framework to include ferromagnetic couplings have also been explored [46–48]. The aforementioned gapped rung-dimer phase of the trellis lattice has been extensively investigated using perturbative methods and quantum Monte Carlo (QMC) simulations [49–52]. In particular, the dynamical structure factor (DSF)—interpreted in terms of triplon excitations—was computed in Ref. 53. Additionally, several works have examined coupled zigzag chains, which form the trellis lattice backbone, using methods such as the coupled-cluster approach [54] and the density-matrix renormalization group (DMRG) combined with linearized spin-wave analysis [55]. Notably, the trellis lattice can be regarded as a special case of a spatially anisotropic triangular lattice [56]. When third-nearest-neighbor couplings are set to zero on certain triangles of this anisotropic lattice, the system reduces to a trellis lattice antiferromagnet that supports a stripe like phase composed of alternately stacked one-dimensional (1D) spiral spin chains. These investigations already highlight the rich variety of ground states and excitation spectra that arise from the interplay between frustration, dimensional crossover, and quantum fluctuations in trellis lattice antiferromagnets. Even more interestingly, at the isotropic point, the ground state could be a quantum paramagnet [25], and possibly, a quantum spin liquid.

On the experimental front, the trellis lattice garnered significant attention following the synthesis of the layered cuprate compound $SrCu_2O_3$ [57], in which magnetic Cu^{2+} ions form spin-1/2 Heisenberg ladders weakly coupled via frustrated interladder exchanges. Strong antiferromagnetic interactions favor singlet formation on the rungs of the ladders, resulting in a spin gap in the excitation spectrum [49]. Under appropriate doping or applied pressure, related cuprate ladder systems, such as $Sr_{14-x}Ca_xCu_{24}O_{41}$, also exhibit superconductivity, suggesting an intrinsic tendency toward pair formation in these quasi-one-dimensional systems [58]. Subsequent studies extended trellis-lattice physics to layered vanadate compounds such as CaV_2O_5 [59], MgV_2O_5 [60], and $Pb_{0.55}Cd_{0.45}V_2O_5$ [61]. In these materials, V^{4+} ions form spin-1/2 planes with a trellis lattice geometry. Unlike in the cuprates, the interladder couplings in vanadates can be appreciable, as revealed by *ab initio* calculations [62, 63], magnetic susceptibility measurements [50], and Raman spectroscopy [64, 65]. More recently, quasi-one-dimensional organic magnets such as α-2-Cl-4-F-V [66] and β-2,3,5-Cl_3-V [67] have been synthesized. These molecular crystals, built from verdazyl radicals carrying spin-1/2, offer a platform for investigating quantum magnetism in low dimensions.

Despite these advances, our understanding of *nonmagnetic* phases on the trellis lattice remains limited. An important open question is whether the combined effects of geometrical frustration, quantum fluctuations, and lattice topology can stabilize exotic phases on this geometry, in particular, a quantum spin liquid at and around the isotropic point. Motivated by these considerations, our present work is devoted to a comprehensive investigation of the properties of various potential QSL ground states on the trellis lattice. Owing to their paramagnetic nature, QSLs cannot be described using the conventional Landau theory of spontaneous symmetry breaking. Instead, their classification involves internal symmetry structures governed by emergent SU(2) gauge degrees of freedom coupled to matter fields [68]. The projective symmetry group (PSG) framework [69–71] provides a powerful approach for the systematic identification and classification of distinct QSL phases by exploiting these emergent gauge structures. This formalism has been successfully employed for many 2D Archimedean lattices, including the square [69, 72], triangular [73–75], honeycomb [76, 77], kagome [78–80], star [81, 82], square-octagon [83], Shastry-Sutherland [84, 85], maple-leaf [43], and bounce [86, 87] lattices.

A. Outline of the manuscript

This paper is organized as follows. In Sec. II, we provide a brief introduction to the fermionic representation of spin-1/2 operators and outline the fundamentals of the PSG construction. Section III presents a detailed analysis of the full symmetry group of the trellis lattice, along with its projective extensions, defined up to elements of the U(1) and $\mathbb{Z}_2$ gauge groups. Focusing on the three symmetry-inequivalent nearest-neighbor bonds, we classify all distinct mean-field states corresponding

to different QSLs that arise from the projective extensions of the full symmetry group. These states, along with their associated gauge structures and flux patterns, are summarized in Sec. IV. In Sec. V, we investigate the phases that emerge as the hopping parameters are varied within the mean-field description. We also construct a phase diagram in Sec. V C based on a spin-1/2 antiferromagnetic Heisenberg model, with exchange couplings J_v, J_z, and J_h defined on the three symmetry-inequivalent nearest-neighbor bonds of the trellis lattice. The spectral properties of the various QSL states are then analyzed in Sec. VI, where we compute both the dynamical and equal-time structure factors (EQSFs) from our mean-field *Ansätze* as well as using state-of-the-art Keldysh pseudofermion functional renormalization group (pf-FRG) and DMRG calculations. Thereafter, Sec. VII provides an in-depth discussion on candidate compounds that realize the trellis lattice, using density functional theory (DFT) and Keldysh pf-FRG, thus outlining a pathway for the observation of this physics in future experiments on quantum materials. Finally, we conclude with a brief discussion of our results and their implications in Sec. VIII.

B. Summary of main results

As mentioned above, in this work, we implement the PSG construction within the Abrikosov-fermion (parton) representation of spin-1/2 operators to classify all distinct fully symmetric QSL states at the mean-field level that can be realized on the trellis lattice. Subsequently, we analyze the corresponding fermionic band structures and map out the associated phase diagram. Besides fully gapped and Dirac QSLs, we discover an intriguing *semi*-Dirac spin liquid state [88–105], for which the spinon dispersion is observed to be linear along one momentum direction but quadratic in the direction orthogonal to it.

For itinerant electrons, semi-Dirac dispersions have recently attracted considerable attention, as they arise from the merging of multiple Dirac points into a single one [89]. Semi-Dirac fermions naturally display strongly anisotropic characteristics: Along one direction the dispersion is quadratic, reflecting Galilean invariance, while along the orthogonal direction it remains linear, reflecting Lorentz invariance. A direct consequence of this anisotropy is the unconventional Landau-level scaling of $B^{2/3}$ with a magnetic field B, which has recently been reported in magneto-optical spectroscopy of ZrSiS and microscopically linked to nodal-line crossings in the material [88]. Thermal or charge transport, being inherently direction sensitive, offers an additional potential probe of semi-Dirac points. However, such measurements require a spectrally isolated semi-Dirac point to achieve a satisfactory signal-to-noise ratio. Despite their charge neutrality, many features of itinerant electrons can carry over to elementary spinon excitations in spin liquids, including their response to external magnetic fields [106]. In particular, thermal conductivity may serve as a probe of transport signatures from low-lying spinon excitations, although such measurements remain experimentally challenging [107–109].

Here, we demonstrate that semi-Dirac spinon dispersions can occur only at high-symmetry points in the Brillouin zone where the little group is C_{2v}, i.e., characterized by a twofold rotation symmetry and two orthogonal reflection symmetries. In contrast, momentum points in the Brillouin zone with larger little groups cannot host semi-Dirac dispersions. Scaling analysis further reveals that the equal-time spin-spin correlations in real space decay algebraically as $\sim 1/r^3$ and $\sim 1/r^6$ along the two orthogonal directions. Finally, we present both dynamical and equal-time spin structure factors, at the mean-field level, for semi-Dirac spin liquids (s-DSLs).

Within a self-consistent mean-field framework, we map out the quantum phase diagram of the most general nearest-neighbor Heisenberg antiferromagnetic Hamiltonian. This procedure entails optimizing over all symmetry-allowed U(1) and $\mathbb{Z}_2$ mean-field *Ansätze* in order to identify the energetically favored solutions. Our analysis reveals six distinct phases, characterized by correlation patterns indicative of (I) zigzag-chain, (II) zigzag-ladder, (III) rung-chain, (IV) rung-ladder, (V) ladder-dimer, and (VI) honeycomb structures. For representative points within these phases, we further assess the role of gauge fluctuations beyond mean-field: at zero temperature using DMRG, and at finite temperature via Keldysh pf-FRG. These calculations reveal significant redistribution of spectral weight in particular within the ladder-dimer and honeycomb phases.

Furthermore, we identify four candidate materials—two cuprates and two vanadates—that can be modeled to good accuracy as two-dimensional systems with dominant Heisenberg interactions along the ladder (J_v), rung (J_h), and zigzag (J_z) bonds. Using DFT combined with an energy-mapping approach, we extract the effective model parameters for $CaCu_2O_3$, $SrCu_2O_3$, MgV_2O_5, and CaV_2O_5. In these compounds, the Cu^{2+} and V^{4+} magnetic ions host $S = 1/2$ moments forming the underlying magnetic lattice, which takes the form of a flat trellis lattice in $SrCu_2O_3$ and a buckled trellis lattice in the other three compounds. The hierarchy of couplings places $CaCu_2O_3$ in close proximity to a one-dimensional limit, while $SrCu_2O_3$ and CaV_2O_5 reduce to coupled two-leg ladder systems, with the latter exhibiting substantially stronger rung couplings. In contrast, MgV_2O_5 displays comparable rung and chain couplings. These effective Hamiltonians are then analyzed using Keldysh pf-FRG, enabling the computation of dynamical spin structure factors at finite temperature. For $CaCu_2O_3$, we find excellent agreement between our calculated spectral functions and previously reported neutron scattering data, thereby validating our effective Hamiltonian. For $SrCu_2O_3$ and CaV_2O_5, the dynamical and equal-

time structure factors closely resemble those expected for the rung-ladder and ladder-dimer phases, respectively, while MgV_2O_5 shows clear signatures of magnetic ordering. Our predictions for the dynamical structure factors of $SrCu_2O_3$ and CaV_2O_5 provide concrete benchmarks for future inelastic neutron scattering experiments.

II. THEORETICAL FRAMEWORK

In this section, we outline the generic theoretical framework employed to investigate quantum spin liquid phases. We begin with the Heisenberg Hamiltonian,

$$\hat{\mathcal{H}} = \sum_{\langle ij \rangle} J_{ij} \hat{\mathbf{S}}_i \cdot \hat{\mathbf{S}}_j, \tag{1}$$

where $\hat{\mathbf{S}}_i$ denotes the spin operator at site i and J_{ij} represents the exchange coupling between sites i and j.

To capture the fractionalized nature of excitations characteristic of QSLs, we introduce charge-neutral, spin-1/2 quasiparticles known as spinons or partons. These quasiparticles can obey either bosonic or fermionic statistics. In this work, we adopt the fermionic representation, which conveniently allows for a unified treatment of both gapped and gapless QSLs. In the Abrikosov fermion formalism, the spin operators are expressed as [110, 111]

$$\hat{S}_i^\alpha = \frac{1}{2} \sum_{\sigma\sigma'} \hat{f}_{i\sigma}^\dagger \tau^\alpha_{\sigma\sigma'} \hat{f}_{i\sigma'}, \tag{2}$$

where $\alpha = x, y, z$, $\sigma, \sigma' \in \{\uparrow, \downarrow\}$, and τ^α are the usual Pauli matrices.

While this representation captures the essence of fractionalization, it enlarges the local Hilbert space. The physical spin Hilbert space at each site has dimension 2, corresponding to spin-up and spin-down states. However, in the fermionic representation, the local Hilbert space includes four states: two singly occupied (physical), and one each of doubly occupied and empty (unphysical). To project back to the physical Hilbert space, we impose the following local constraints:

$$\sum_\sigma \hat{f}_{i\sigma}^\dagger \hat{f}_{i\sigma} = 1, \quad \sum_{\sigma,\sigma'} \hat{f}_{i\sigma} \hat{f}_{i\sigma'} \varepsilon_{\sigma\sigma'} = 0, \tag{3}$$

where $\varepsilon_{\sigma\sigma'}$ is the rank-2 antisymmetric tensor.

The fermionic parton construction naturally gives rise to an emergent SU(2) gauge symmetry. This becomes explicit by introducing the SU(2) doublet field

$$\hat{\psi}_i = \begin{bmatrix} \hat{f}_{i\uparrow} & \hat{f}_{i\downarrow}^\dagger \\ \hat{f}_{i\downarrow} & -\hat{f}_{i\uparrow}^\dagger \end{bmatrix}, \tag{4}$$

in terms of which the spin operators can be compactly written as

$$\hat{S}_i^\alpha = \frac{1}{2} \mathrm{Tr} \left[\hat{\psi}_i^\dagger \tau^\alpha \hat{\psi}_i \right]. \tag{5}$$

This representation reveals the invariance of spin operators under local SU(2) gauge transformations $\hat{\psi}_i \to \hat{\psi}_i W_i$, with $W_i \in \mathrm{SU}(2)$.

Substituting Eq. (2) into the Heisenberg Hamiltonian (1) results in a quartic fermionic interaction term. To obtain a solvable theory, we perform a mean-field decoupling in the spin-singlet channel, which is appropriate for describing spin-rotation-invariant states. The relevant mean-field parameters are the singlet hopping, χ_{ij}, and singlet pairing, Δ_{ij}, fields, defined as

$$\chi_{ij} = \left\langle \sum_\sigma \hat{f}_{i\sigma}^\dagger \hat{f}_{j\sigma} \right\rangle, \tag{6}$$

$$\Delta_{ij}^\dagger = -\left\langle \sum_{\sigma,\sigma'} \hat{f}_{i\sigma} \hat{f}_{j\sigma'} \varepsilon_{\sigma\sigma'} \right\rangle. \tag{7}$$

The resulting mean-field Hamiltonian takes the form

$$\hat{H}_{\mathrm{MF}} = \frac{3}{8} \sum_{i,j} J_{ij} \left[\frac{1}{2} \mathrm{Tr}(u_{ij}^\dagger u_{ij}) - \mathrm{Tr} \left(\hat{\psi}_i u_{ij} \hat{\psi}_j^\dagger + \mathrm{h.c.} \right) \right] + \sum_{i,\mu} a_\mu(i) \, \mathrm{Tr} \left[\hat{\psi}_i \tau^\mu \hat{\psi}_i^\dagger \right], \tag{8}$$

where u_{ij} is the SU(2) matrix-valued link field associated with the bond $\langle ij \rangle$, given by

$$u_{ij} = \begin{bmatrix} \chi_{ij}^\dagger & \Delta_{ij} \\ \Delta_{ij}^\dagger & -\chi_{ij} \end{bmatrix}. \tag{9}$$

The last term in Eq. (8) imposes the single-occupancy constraint (3) at the mean-field level using Lagrange multipliers $a_\mu(i)$ for $\mu = 1, 2, 3$. Together, the combination $\{u_{ij}, a_\mu(i)\}$ defines a mean-field *Ansatz* characterizing a quantum paramagnetic state.

Now, it is straightforward to verify that the mean-field Hamiltonian in Eq. (8) is invariant under local SU(2) gauge transformations of the form

$$\hat{\psi}_i \to \hat{\psi}_i W_i \,, \quad u_{ij} \to W_i^\dagger u_{ij} W_j \,, \quad a_\alpha \tau^\alpha \to a_\alpha W_i^\dagger \tau^\alpha W_i \,, \tag{10}$$

where $W_i \in \mathrm{SU}(2)$ is a local gauge transformation matrix.

The physical implication of this gauge redundancy is that a given mean-field *Ansatz* $\{u_{ij}, a_\alpha\}$ and its gauge-transformed counterpart $\{u'_{ij}, a'_\alpha\}$ describe the same physical spin liquid state. In other words, different *Ansätze* related by local SU(2) gauge transformations are physically equivalent, whereas those not connected by such transformations correspond to distinct quantum paramagnetic phases. This redundancy can be exploited to classify and characterize QSL phases using projective symmetry considerations, as we elaborate on next.

An important consequence of the SU(2) gauge structure is that global and lattice symmetries may act on the fermionic operators in a *projective* manner. To illustrate this, consider a symmetry operation $\mathcal{O}$ from the

lattice space group. Its naive action on the mean-field variables is to map $u_{ij} \to u_{\mathcal{O}(i)\mathcal{O}(j)}$. If it happens that $u_{ij} \neq u_{\mathcal{O}(i)\mathcal{O}(j)}$, one might incorrectly conclude that the *Ansatz* breaks the symmetry $\mathcal{O}$. However, the symmetry can still be preserved projectively if there exists a local SU(2) gauge transformation $W_{\mathcal{O}}(i)$ associated with $\mathcal{O}$ such that

$$W^{\dagger}_{\mathcal{O}}(\mathcal{O}(i))\, u_{\mathcal{O}(i)\mathcal{O}(j)}\, W_{\mathcal{O}}(\mathcal{O}(j)) = u_{ij}. \tag{11}$$

In this case, the combined operation of the lattice symmetry $\mathcal{O}$ and the corresponding gauge transformation $W_{\mathcal{O}}$ leaves the *Ansatz* invariant. The full set of such symmetry-gauge combinations $\{\mathcal{O}, W_{\mathcal{O}}\}$ defines the PSG. The PSG provides a classification scheme for QSLs, playing a role analogous to that of symmetry groups in the Landau paradigm of symmetry-breaking phases.

Within the PSG framework, one can also define an analog of the identity operation. Specifically, we define the invariant gauge group (IGG) as the subgroup of SU(2) gauge transformations $\mathcal{G}_i$ that leave the mean-field *Ansatz* invariant:

$$\mathcal{G}_i^{\dagger} u_{ij} \mathcal{G}_j = u_{ij}, \qquad \mathcal{G}_i \in \mathrm{SU}(2). \tag{12}$$

The IGG thus characterizes the residual gauge freedom of the *Ansatz* and corresponds to the projective realization of the identity element in the symmetry group.

Although the IGG describes, in general, a *local* symmetry operation, one can always choose a gauge such that the IGG only involves *global* elements of either SU(2) or its subgroups, U(1), or $\mathbb{Z}_2$. For such a gauge choice, the *Ansatz* is said to be in its canonical form, and its IGG structure becomes manifest. To make this explicit, we parametrize the SU(2) link variable u_{ij} in terms of four real numbers λ^{μ}_{ij} as

$$u_{ij} = i\lambda^0_{ij}\tau^0 + \sum_{\mu=1}^{3} \lambda^{\mu}_{ij}\tau^{\mu}. \tag{13}$$

Based on this parametrization, different IGG structures emerge:

(a) If $\lambda^{\mu}_{ij} = 0$ for $\mu = 1, 2, 3$, then the IGG is global SU(2).

(b) If $\lambda^1_{ij} = \lambda^2_{ij} = 0$ and $\lambda^3_{ij} \neq 0$, then the IGG is global U(1).

(c) If $\lambda^{\mu}_{ij} \neq 0 \,\forall\, \mu$, then the IGG is $\mathbb{Z}_2$.

Since the IGG is a gauge-invariant property of the *Ansatz*, it is conventional to label the *Ansätze* according to their IGG structure [e.g., U(1) QSL, $\mathbb{Z}_2$ QSL, etc.], thereby identifying the type of emergent gauge theory associated with each QSL phase.

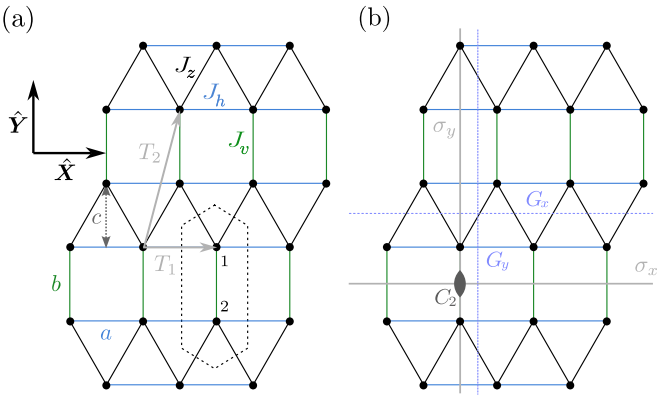


FIG. 1. (a) Trellis lattice with exchange couplings J_v (green), J_z (black), and J_h (blue). The unit cell contains two sites labeled "1" and "2." The lattice parameters are denoted by a, b, and c. (b) Illustration of the lattice space-group symmetries. C_2 represents a twofold rotation about an axis perpendicular to the lattice plane. σ_x and σ_y denote reflections about the horizontal and vertical solid lines, respectively. G_x is a glide symmetry consisting of a reflection about the horizontal dashed line followed by a translation $\frac{a}{2}\hat{\boldsymbol{X}} = \frac{1}{2}\boldsymbol{T}_1$. Similarly, G_y combines a reflection along the vertical dashed line with a translation $(b+c)\hat{\boldsymbol{Y}} = -\frac{1}{2}\boldsymbol{T}_1 + \boldsymbol{T}_2$.

III. SYMMETRIES AND PROJECTIVE REALIZATIONS

A. Lattice and time-reversal symmetries

On the trellis lattice, any site can be described by the position vector $\boldsymbol{r} = x\boldsymbol{T}_1 + y\boldsymbol{T}_2 + \boldsymbol{\epsilon}_u$, where we choose the lattice vectors in the Cartesian basis as $\boldsymbol{T}_1 = a\hat{\boldsymbol{X}}$ and $\boldsymbol{T}_2 = (a/2)\hat{\boldsymbol{X}} + (b+c)\hat{\boldsymbol{Y}}$, with a, b, and c denoting the bond lengths as illustrated in Fig. 1. The vectors $\boldsymbol{\epsilon}_u$ represent the positions of the sublattices within the unit cell. The unit cell consists of two sites located at $\boldsymbol{\epsilon}_1 = (b/2)\hat{\boldsymbol{Y}}$ and $\boldsymbol{\epsilon}_2 = -(b/2)\hat{\boldsymbol{Y}}$.

The symmetry group of the trellis lattice corresponds to the nonsymmorphic wallpaper group *cmm*, which can be generated by two translations (T_1 and T_2), a twofold rotation (C_2), two mirror reflections (σ_x and σ_y), and two glide reflections (G_x and G_y). A pictorial representation of these symmetry elements is provided in Fig. 1(b). The action of each symmetry operation on a lattice site labeled by (x, y, u)—where (x, y) denotes the unit cell coordinate and u specifies the sublattice index—is given by

$$\begin{aligned}
&T_1(x,y,u) \to (x+1, y, u),\\
&T_2(x,y,u) \to (x, y+1, u),\\
&C_2(x,y,u) \to (-x, -y, \bar{u}),\\
&\sigma_x(x,y,u) \to (x+y, -y, \bar{u}),\\
&\sigma_y(x,y,u) \to (-x-y, y, u),\\
&G_x(x,y,u) \to (x+y, -y+1, \bar{u}),\\
&G_y(x,y,u) \to (-x-y, y+1, u),
\end{aligned} \tag{14}$$

with $\bar{u} \equiv 3 - u$.

However, one can verify that several of these symmetry operations can be expressed in terms of a minimal generating set consisting of T_2, C_2, and σ_x as

$$T_1 = G_x^2,\ G_x = T_2\sigma_x,\ G_y = T_2^2 C_2 G_x,\ \sigma_y = C_2\sigma_x. \tag{15}$$

Therefore, the minimal set of generators required for constructing symmetric *Ansätze* invariant under the entire space group comprises T_2, C_2, and σ_x. Nonetheless, we include T_1 in our analysis for convenience.

In addition to these lattice symmetries, we also incorporate time-reversal symmetry $\mathcal{T}$, given our focus on classifying fully symmetric (i.e., nonchiral) spin liquid *Ansätze*. The time-reversal operation does not alter the spatial position of the lattice sites and hence, commutes with all space-group elements. However, its action on a mean-field *Ansatz* is nontrivial [69, 80] and is given by

$$\mathcal{T}(u_{ij}, a_\mu) = -(u_{ij}, a_\mu). \tag{16}$$

Accordingly, the projective symmetry condition in Eq. (11) implies that the time-reversal symmetry imposes

$$G_{\mathcal{T}}^\dagger(i) u_{ij} G_{\mathcal{T}}(j) = -u_{ij}, \quad \text{for } \mathcal{O} = \mathcal{T}. \tag{17}$$

Taken together with Eq. (14), this completely specifies the full symmetry group relevant for the trellis lattice.

Last, we note that there exist specific combinations of symmetry operations under which any given lattice site remains invariant. These combinations effectively act as the identity and are summarized below:

$$T_1 T_2 T_1^{-1} T_2^{-1} = \mathcal{I}, \tag{18}$$
$$T_1 C_2^{-1} T_1 C_2 = \mathcal{I}, \tag{19}$$
$$T_2 C_2^{-1} T_2 C_2 = \mathcal{I}, \tag{20}$$
$$T_1^{-1}\sigma_x^{-1} T_1 \sigma_x = \mathcal{I}, \tag{21}$$
$$T_1^{-1} T_2 \sigma_x^{-1} T_2 \sigma_x = \mathcal{I}, \tag{22}$$
$$C_2\sigma_x C_2 \sigma_x = \mathcal{I}, \tag{23}$$
$$C_2^2 = \mathcal{I}, \tag{24}$$
$$\sigma_x^2 = \mathcal{I}, \tag{25}$$
$$T_1^{-1} T_2 \sigma_x T_1 \sigma_x^{-1} T_2^{-1} = \mathcal{I}, \tag{26}$$
$$C_2 T_1 T_2^{-1} \sigma_x C_2 T_2 \sigma_x = \mathcal{I}, \tag{27}$$
$$\mathcal{T}^2 = \mathcal{I}, \tag{28}$$
$$\mathcal{T}\mathcal{O}\mathcal{T}^{-1}\mathcal{O}^{-1} = \mathcal{I}, \tag{29}$$

where $\mathcal{O} \in \{T_1, T_2, \sigma_x, C_2\}$.

B. Projective symmetry groups

To implement the projective realization of the symmetry elements $\mathcal{O} \in \{T_1, T_2, \sigma_x, C_2, \mathcal{T}\}$, each symmetry operation must be associated with a corresponding SU(2) gauge transformation. These projective gauge transformations must satisfy the same algebraic relations as the original symmetry group generators. Consequently, the symmetry relations in Eqs. (18)–(29) impose a set of constraints on the operators $W_{\mathcal{O}}$. The allowed PSG solutions are then obtained by solving the resulting algebraic conditions, as outlined in Appendix A. Different choices of the IGG lead to distinct classes of PSG solutions, which we describe below.

1. U(1) *solutions*

Given that the trellis lattice is nonbipartite, SU(2) *Ansätze* with nonvanishing mean-field parameters on all nearest-neighbor bonds are not possible. We therefore begin with the IGG set to U(1), such that the identity element is defined up to a U(1) phase. Realizing such U(1) *Ansätze* requires including only hopping terms in the mean-field Hamiltonian introduced above.

The generic form of the PSG elements in this case is given by

$$W_{\mathcal{O}} = \mathcal{F}_z(\phi_{\mathcal{O}}(x, y, u))(i\tau^x)^{w_{\mathcal{O}}}, \tag{30}$$

where $\mathcal{F}_z(\xi) \equiv \exp(i\xi\,\tau^z)$ and $w_{\mathcal{O}} \in \{0, 1\}$. This structure ensures that the *Ansätze* are in their canonical form. Importantly, the symmetry relation in Eq. (22), where T_1 appears only once, immediately excludes the possibility $w_{T_1} = 1$. Therefore, only the two cases $(w_{T_1}, w_{T_2}) = (0, 0)$ and $(0, 1)$ are allowed for arbitrary values of w_{σ_x}, w_{C_2}, and $w_{\mathcal{T}}$.

The algebraic PSG solutions are then given by the following expressions (see Appendix B for details):

a. Case I: $w_{T_1} = 0,\ w_{T_2} = 0$

$$\phi_{T_1}(x, y, u) = y\,\theta, \tag{31}$$
$$\phi_{T_2}(x, y, u) = 0, \tag{32}$$
$$\phi_{C_2}(x, y, u) = -(-1)^{w_{C_2}}(x\,\theta_{C_2T_1} + y\,\theta_{C_2T_2}) + \rho_{C_2,u}, \tag{33}$$
$$\phi_{\sigma_x}(x, y, u) = -(-1)^{w_{\sigma_x}}(x\,\theta_{\sigma_xT_1} + y\,\theta_{\sigma_xT_2}) + (-1)^{w_{\sigma_x}}\frac{1}{2}y(y-1)\theta + \rho_{\sigma_x,u}, \tag{34}$$
$$\phi_{\mathcal{T}}(x, y, u) = y\,\theta_{\mathcal{T}T_2} + \rho_{\mathcal{T},u}. \tag{35}$$

b. Case II: $w_{T_1} = 0,\ w_{T_2} = 1$

$$\phi_{T_1}(x, y, u) = (-1)^y\theta, \tag{36}$$
$$\phi_{T_2}(x, y, u) = 0, \tag{37}$$
$$\phi_{C_2}(x, y, u) = (-1)^{w_{C_2}}(\zeta_y\,\theta_{C_2T_2}) + \rho_{C_2,u}, \tag{38}$$
$$\phi_{\sigma_x}(x, y, u) = (-1)^{w_{\sigma_x}}(\zeta_y\,\theta_{\sigma_xT_2} - y\,\theta) + \rho_{\sigma_x,u}, \tag{39}$$
$$\phi_{\mathcal{T}}(x, y, u) = \zeta_y\,\theta_{\mathcal{T}T_2} + \rho_{\mathcal{T},u}, \tag{40}$$

PSG No.	w_{T_2}	w_{C_2}	w_{σ_x}	$w_{\mathcal{T}}$	θ	$\theta_{C_2T_1}$	$\theta_{C_2T_2}$	$\theta_{\sigma_xT_1}$	$\theta_{\sigma_xT_2}$	$\theta_{\mathcal{T}T_2}$	$\rho_{C_2,u}$	$\rho_{\sigma_x,u}$	No. of PSGs
1	0	0	0	0	$n\pi$	0	0	$n\pi$	$n_{\sigma_xT_2}+n\pi/2$	$n\pi$	0	$\{0,n_{\sigma_x}\pi\}$	2^3
2	0	0	1	0	θ	0	0	0	$n_{\sigma_xT_2}\pi-\theta/2$	$n\pi$	0	$\{0,n_{\sigma_x}\pi\}$	2^3
3	0	1	0	0	$n\pi$	$n\pi$	$n_{C_2T_2}\pi$	$n\pi$	0	$n\pi$	$\{0,n_{C_2}\pi\}$	$\{0,\theta_{\sigma_x}\}$	2^3
4	0	1	1	0	$n\pi$	$n\pi$	$n_{C_2T_2}\pi$	$n\pi$	0	$n\pi$	$\{0,n_{C_2}\pi\}$	$\{0,n_{\sigma_x}\pi\}$	2^4
5	0	0	0	1	$n\pi$	$n\pi$	$n_{TT_2}\pi$	$n\pi$	$n_{TT_2}\pi+n_{\sigma_xT_2}\pi$	0	$\{0,n_{C_2}\pi\}$	$\{0,n_{\sigma_x}\pi\}$	2^5
6	0	0	1	1	$n\pi$	$n\pi$	$n_{TT_2}\pi$	$n\pi$	$n_{\sigma_xT_2}\pi$	0	$\{0,n_{C_2}\pi\}$	$\{0,n_{\sigma_x}\pi\}$	2^5
7	0	1	0	1	$n\pi$	$n\pi$	$n_{C_2T_2}\pi$	$n\pi$	0	0	$\{0,n_{C_2}\pi\}$	$\{0,\theta_{\sigma_x}\}$	2^3
8	0	1	1	1	$n\pi$	$n\pi$	$n_{C_2T_2}\pi$	$n\pi$	0	0	$\{0,n_{C_2}\pi\}$	$\{0,n_{\sigma_x}\pi\}$	2^4
9	1	0	0	0	$n\pi$	0	$n_{C_2T_2}\pi$	0	$n_{\sigma_xT_2}\pi$	$n_{\mathcal{T}T_2}\pi$	$\{0,\theta_{C_2}\}$	$\{0,\theta_{\sigma_x}\}$	2^4
10	1	0	1	0	$n\pi$	0	$n_{C_2T_2}\pi$	0	0	$n_{\mathcal{T}T_2}\pi$	$\{0,n_{C_2}\pi\}$	$\{0,n_{\sigma_x}\pi\}$	2^5
11	1	1	0	0	$n\pi$	0	0	0	$n_{\sigma_xT_2}\pi$	$n_{\mathcal{T}T_2}\pi$	$\{0,n_{C_2}\pi\}$	$\{0,n_{\sigma_x}\pi\}$	2^5
12	1	1	1	0	$n\pi$	0	0	0	$n_{\sigma_xT_2}\pi$	$n_{\mathcal{T}T_2}\pi$	$\{0,n_{C_2}\pi\}$	$\{0,n_{\sigma_x}\pi\}$	2^5
13	1	0	0	1	$n\pi$	0	$n_{C_2T_2}\pi$	0	$n_{\sigma_xT_2}\pi$	$\theta_{\mathcal{T}T_2}\pi$	$\{0,\theta_{C_2}\}$	$\{0,\theta_{\sigma_x}\}$	$2^3\times2$
14	1	0	1	1	$n\pi$	0	$n_{C_2T_2}\pi$	0	0	$n_{\mathcal{T}T_2}\pi$	$\{0,n_{C_2}\pi\}$	$\{0,n_{\sigma_x}\pi\}$	$2^5\times2$
15	1	1	0	1	$n\pi$	0	0	0	$n_{\sigma_xT_2}\pi$	$n_{\mathcal{T}T_2}\pi$	$\{0,n_{C_2}\pi\}$	$\{0,n_{\sigma_x}\pi\}$	$2^5\times2$
16	1	1	1	1	$n\pi$	0	0	0	$n_{\sigma_xT_2}\pi$	$n_{\mathcal{T}T_2}\pi$	$\{0,n_{C_2}\pi\}$	$\{0,n_{\sigma_x}\pi\}$	$2^5\times2$

TABLE I. PSG solutions for the trellis lattice with invariant gauge group U(1). For rows 1–4 and 9–12, $\rho_{\mathcal{T},u}=\{0,\pi\}$; for rows 5–8, $\rho_{\mathcal{T},u}=0$; and for rows 13–16, $\rho_{\mathcal{T},u}=\{0,n_{\mathcal{T}}\pi\}$. In total, 448 gauge-inequivalent PSG solutions exist for the trellis lattice with IGG U(1).

PSG no.	$\mathcal{W}_{C_2,u}$	$\mathcal{W}_{\mathcal{T},u}$	No. of PSGs
1	$\{\tau^0,\eta_{C_2}\tau^0\}$	$\{\tau^0,-\tau^0\}$	$2^4\times2$
2	$\{\tau^0,\eta_{C_2}\tau^0\}$	$\{i\tau^y,\eta_{\mathcal{T}}i\tau^y\}$	$2^4\times2^2$
3	$\{i\tau^z,\eta_{C_2}i\tau^z\}$	$\{\tau^0,-\tau^0\}$	$2^4\times2$
4	$\{i\tau^z,\eta_{C_2}i\tau^z\}$	$\{i\tau^z,\eta_{\mathcal{T}}i\tau^z\}$	$2^4\times2^2$
5	$\{i\tau^z,\eta_{C_2}i\tau^z\}$	$\{i\tau^y,\eta_{\mathcal{T}}i\tau^y\}$	$2^4\times2^2$

TABLE II. $\mathcal{W}_{\mathcal{O},u}$ matrices, which, together with η_{T_1}, $\eta_{C_2T_2}$, η_{σ_x}, and $\eta_{\mathcal{T}x}$, yield a total of 256 gauge-inequivalent PSG solutions.

where $\zeta_y=\frac{1}{2}(1+(-1)^y)$.

All allowed U(1) phase parameters θ and ρ for each choice of $\{w_{T_2},w_{\sigma_x},w_{C_2},w_{\mathcal{T}}\}$ are enumerated in Table I. Thus, any U(1) PSG solution can be uniquely identified by three binary integers $\{w_{C_2},w_{\sigma_x},w_{\mathcal{T}}\}$ and nine U(1) phases: $\left\{\theta,\theta_{C_2T_1},\theta_{C_2T_2},\theta_{\sigma_xT_1},\theta_{\sigma_xT_2},\theta_{\mathcal{T}T_2},\rho_{C_2,u},\rho_{\sigma_x,u},\rho_{\mathcal{T},u}\right\}$, each taking values in $[0,2\pi)$. However, these parameters are not all independent due to gauge redundancy. The gauge-inequivalent combinations of θ and ρ for various choices of $\{w_{C_2},w_{\sigma_x},w_{\mathcal{T}}\}$ are summarized in Table I, enlisting a total of 448 distinct U(1) PSGs. Hence, the full symmetry group of the trellis lattice admits 448 inequivalent U(1) projective symmetry group realizations.

2. $\mathbb{Z}_2$ solutions

Breaking down the IGG from U(1) to $\mathbb{Z}_2$ necessitates the inclusion of both hopping and pairing amplitudes in the link fields, thereby requiring the most general form of mean-field *Ansätze*. Within this framework, projective realizations of the symmetry group are defined up to $\mathbb{Z}_2$ gauge transformations, i.e., global signs ±1. Solving the associated algebraic constraints (see Appendix C), we obtain a total of 256 gauge-inequivalent $\mathbb{Z}_2$ PSG solutions. These can be summarized as follows:

$$W_{T_1}(x,y,u)=\eta_{T_1}^{y}\tau^0, \tag{41}$$
$$W_{T_2}(x,y,u)=\tau^0, \tag{42}$$
$$W_{C_2}(x,y,u)=\eta_{C_2T_2}^{y}\eta_{T_1}^{x}\mathcal{W}_{C_2,u}, \tag{43}$$
$$W_{\sigma_x}(x,y,u)=\eta_{T_1}^{-y(y-1)/2+x}\eta_{\sigma_x}^{u}\tau^0, \tag{44}$$
$$W_{\mathcal{T}}(x,y,u)=\eta_{\mathcal{T}y}^{y}\mathcal{W}_{\mathcal{T},u}, \tag{45}$$

where all the parameters $\eta_{\dots}$ take values ±1. The sublattice-dependent PSG elements $\mathcal{W}_{C_2,u}$ and $\mathcal{W}_{\mathcal{T},u}\in$ SU(2) are naturally constrained by the gauge-enriched algebraic relations imposed by the symmetry group. All gauge-inequivalent choices for these sublattice-dependent elements are provided in Table II. From the enumeration

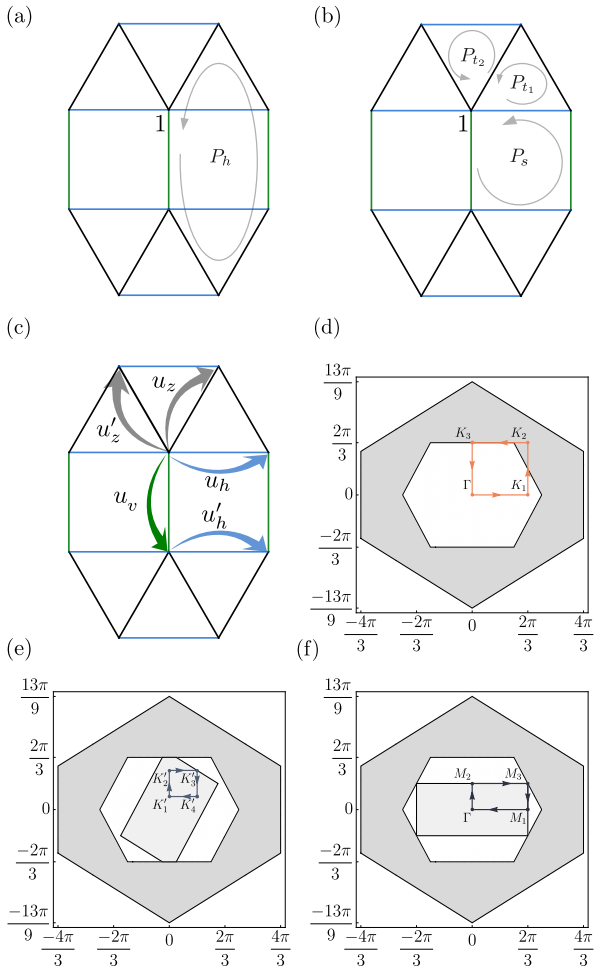


FIG. 2. (a), (b) Graphical illustration of the SU(2) flux operators on the trellis lattice with the base site labeled "1." Loop operators P_h, P_s, and P_t correspond to hexagonal, square, and triangular plaquettes, respectively. (c) Definitions of reference bonds within the unit cell at $(x, y) = (0, 0)$. (d)–(f) The white (gray) hexagons denote the first (extended) Brillouin zones for lattice parameters $b = 1$, $c = 1/2$, and $a = 3/2$, with the extended zone obtained by a scaling factor of 3. Panels (d)–(f) indicate the paths along which dispersions are plotted for the U(1) *Ansätze*: (d) U1 and U2, (e) U3 and U4, where the light gray region shows the reduced Brillouin zone for doubling along $\boldsymbol{T}_1$, and (f) U5 and U6, with the reduced Brillouin zone for doubling along $\boldsymbol{T}_2$. $\boldsymbol{T}_1$ and $\boldsymbol{T}_2$ are defined in Fig. 1.

therein, we see that when the IGG is set to $\mathbb{Z}_2$, the full symmetry group admits 256 distinct projective realizations.

IV. SHORT-RANGED MEAN-FIELD ANSÄTZE

Given the PSG solutions obtained in Secs. III B 1 and III B 2, we now turn to the construction of mean-field *Ansätze* for QSL states by imposing symmetry constraints on the link fields. The detailed derivation of symmetry-allowed forms for the link variables is presented in Appendix D. While our algebraic analysis yielded 448 U(1) and 256 $\mathbb{Z}_2$ PSG classes, the number of distinct realizable short-ranged *Ansätze* on the trellis lattice is significantly fewer. This reduction arises from restricting the link fields to nonzero values on only the three symmetry-inequivalent nearest-neighbor bonds—J_h, J_v, and J_z.

Within this short-range framework, we find a total of $6 + 1$ U(1) *Ansätze*, where "+1" corresponds to an infinite class of gauge-inequivalent states stemming from a continuous U(1) degree of freedom associated with the PSG class given in the second row of Table I. Additionally, we identify 25 distinct $\mathbb{Z}_2$ *Ansätze*. In this section, we present and discuss the structure and classification of these short-ranged mean-field states.

Before proceeding further, it is useful to introduce an SU(2) flux operator, which provides additional gauge-invariant characterization of the *Ansätze*, beyond the PSG labels. Defined for a closed loop $\mathcal{C}_i$ based at site i, the SU(2) flux or loop operator is given by

$$\mathcal{P}_{\mathcal{C}_i} = u_{ij}u_{jl}\ldots u_{ki}. \tag{46}$$

Under a local SU(2) gauge transformation W_i, this operator transforms as

$$\mathcal{P}_{\mathcal{C}_i} \to W_i^\dagger \mathcal{P}_{\mathcal{C}_i} W_i\,, \tag{47}$$

implying that the commutation or anticommutation relations between loop operators based at the same site remain invariant under such a rotation. Hence, the flux structure around various plaquettes becomes a powerful tool to distinguish between different *Ansätze*.

In general, a loop operator around a q-sided plaquette takes the form [80]

$$P_{\mathcal{C}_i}(\varphi_{\mathcal{C}_i}) \propto g_i \mathcal{F}_z(i\varphi_{\mathcal{C}_i})(\tau^z)^q g_i^\dagger, \quad g_i \in \mathrm{SU}(2), \tag{48}$$

where $\varphi_{\mathcal{C}_i}$ represents the effective flux piercing the loop $\mathcal{C}_i$.

On the trellis lattice, we consider a representative base site, labeled as "1" without loss of generality, as shown in Figs. 2(a) and 2(b). Starting from this site, we define one hexagonal loop P_h, one square loop P_s, and two triangular loops P_{t_1} and P_{t_2}, each associated with fluxes φ_h, φ_s, φ_{t_1}, and φ_{t_2}, respectively. In the case of a U(1) IGG, these fluxes commute, and their additive structure permits the identification of the total flux threading a hexagonal plaquette as the sum of the fluxes through its constituent triangular and square subloops. The corresponding flux configurations for each U(1) *Ansatz* are illustrated in Fig. 3.

A. U(1) *Ansätze*

In this section, we present the different symmetric U(1) mean-field *Ansätze* that are realizable under the con-

Label	u_v	u_h,$u_h^{'}$	u_z,$u_z^{'}$	$a_{\mu,u}$	Parent U(1)
Z1	$\{\tau^z\}$	$\{\tau^x,\tau^z\}$,$\{\tau^x,\tau^z\}$	$\{\tau^x,\tau^z\}$,$\{\tau^x,\tau^z\}$	$\{\tau^x,\tau^z\}$,$\{\tau^x,\tau^z\}$	U1,U5
Z2	$\{\tau^z\}$	$\{\tau^x,\tau^z\}$,$\{\tau^x,\tau^z\}$	$\{\tau^y\}$,$\{\tau^y\}$	$\{\tau^x,\tau^z\}$,$\{\tau^x,\tau^z\}$	U5
Z3	$\{\tau^z\}$	$\{\tau^x,\tau^z\}$,$\{-\tau^x,-\tau^z\}$	$\{\tau^x,\tau^z\}$,$\{-\tau^x,-\tau^z\}$	$\{\tau^x,\tau^z\}$,$\{\tau^x,\tau^z\}$	U3
Z4	$\{\tau^z\}$	$\{\tau^x,\tau^z\}$,$\{-\tau^x,-\tau^z\}$	$\{\tau^y\}$,$\{-\tau^y\}$	$\{\tau^x,\tau^z\}$,$\{\tau^x,\tau^z\}$	A
Z5	$\{\tau^z\}$	$\{\tau^x,\tau^z\}$,$\{\tau^x,\tau^z\}$	$\{i\tau^0\}$,$\{-i\tau^0\}$	$\{\tau^x,\tau^z\}$,$\{\tau^x,\tau^z\}$	U1
Z6	$\{\tau^z\}$	$\{\tau^x,\tau^z\}$,$\{-\tau^x,-\tau^z\}$	$\{i\tau^0\}$,$\{i\tau^0\}$	$\{\tau^x,\tau^z\}$,$\{\tau^x,\tau^z\}$	U3
Z7	$\{\tau^z\}$	$\{\tau^x,\tau^z\}$,$\{\tau^x,-\tau^z\}$	$\{\tau^z\}$,$\{\tau^z\}$	$\{\tau^x,\tau^z\}$,$\{\tau^x,-\tau^z\}$	U2
Z8	$\{\tau^z\}$	$\{\tau^x,\tau^z\}$,$\{-\tau^x,\tau^z\}$	$\{\tau^z\}$,$\{-\tau^z\}$	$\{\tau^x,\tau^z\}$,$\{\tau^x,-\tau^z\}$	U4
Z9	$\{\tau^z\}$	$\{\tau^x,\tau^z\}$,$\{-\tau^x,\tau^z\}$	$\{\tau^z\}$,$\{\tau^z\}$	$\{\tau^x,\tau^z\}$,$\{-\tau^x,\tau^z\}$	U1
Z10	$\{\tau^z\}$	$\{\tau^x,\tau^z\}$,$\{\tau^x,-\tau^z\}$	$\{\tau^z\}$,$\{-\tau^z\}$	$\{\tau^x,\tau^z\}$,$\{-\tau^x,\tau^z\}$	U3
Z11	$\{\tau^z\}$	$\{\tau^x,\tau^z\}$,$\{\tau^x,-\tau^z\}$	$\{-\tau^x\}$,$\{\tau^x\}$	$\{\tau^x,\tau^z\}$,$\{\tau^x,-\tau^z\}$	U6
Z12	$\{\tau^z\}$	$\{\tau^x,\tau^z\}$,$\{-\tau^x,\tau^z\}$	$\{\tau^x\}$,$\{-\tau^x\}$	$\{\tau^x,\tau^z\}$,$\{-\tau^x,\tau^z\}$	U5
Z13	$\{\tau^z\}$	$\{\tau^x,\tau^z\}$,$\{\tau^x,-\tau^z\}$	$\{\tau^x\}$,$\{\tau^x\}$	$\{\tau^x,\tau^z\}$,$\{-\tau^x,\tau^z\}$	A
Z14	$\{\tau^z\}$	$\{\tau^x,\tau^z\}$,$\{-\tau^x,\tau^z\}$	$\{-i\tau^0,-\tau^y\}$,$\{i\tau^0,\tau^y\}$	$\{\tau^x,\tau^z\}$,$\{-\tau^x,\tau^z\}$	U1,U5
Z15	$\{\tau^z\}$	$\{\tau^x,\tau^z\}$,$\{-\tau^x,\tau^z\}$	$\{i\tau^0,-\tau^y\}$,$\{-i\tau^0,\tau^y\}$	$\{\tau^x,\tau^z\}$,$\{\tau^x,-\tau^z\}$	U4
Z16	$\{\tau^z\}$	$\{\tau^x,\tau^z\}$,$\{\tau^x,-\tau^z\}$	$\{i\tau^0,-\tau^y\}$,$\{i\tau^0,-\tau^y\}$	$\{\tau^x,\tau^z\}$,$\{\tau^x,-\tau^z\}$	U2, U6
Z17	$\{\tau^z\}$	$\{\tau^x,\tau^z\}$,$\{\tau^x,-\tau^z\}$	$\{i\tau^0,\tau^y\}$,$\{i\tau^0,\tau^y\}$	$\{\tau^x,\tau^z\}$,$\{-\tau^x,\tau^z\}$	U3
Z18	$\{\tau^z\}$	$\{\tau^z\}$,$\{\tau^z\}$	$\{i\tau^0,\tau^y\}$,$\{-i\tau^0,\tau^y\}$	$\{\tau^z\}$,$\{\tau^z\}$	U1
Z19	$\{\tau^z\}$	$\{\tau^z\}$,$\{-\tau^z\}$	$\{i\tau^0,\tau^y\}$,$\{i\tau^0,-\tau^y\}$	$\{\tau^z\}$,$\{\tau^z\}$	U3,U5
Z20	$\{\tau^z\}$	$\{\tau^z\}$,$\{-\tau^z\}$	$\{i\tau^0,\tau^y\}$,$\{i\tau^0,-\tau^y\}$	$\{\tau^z\}$,$\{-\tau^z\}$	U2, U6
Z21	$\{\tau^z\}$	$\{\tau^z\}$,$\{\tau^z\}$	$\{-i\tau^0,\tau^y\}$,$\{i\tau^0,\tau^y\}$	$\{\tau^z\}$,$\{-\tau^z\}$	U4
Z22	$\{\tau^z\}$	$\{\tau^z\}$,$\{-\tau^z\}$	$\{-\tau^x,\tau^z\}$,$\{\tau^x,\tau^z\}$	$\{\tau^z\}$,$\{-\tau^z\}$	U2, U6
Z23	$\{\tau^z\}$	$\{\tau^z\}$,$\{\tau^z\}$	$\{\tau^x,\tau^z\}$,$\{\tau^x,-\tau^z\}$	$\{\tau^z\}$,$\{-\tau^z\}$	U4
Z24	$\{\tau^z\}$	$\{\tau^z\}$,$\{\tau^z\}$	$\{\tau^x,\tau^z\}$,$\{-\tau^x,\tau^z\}$	$\{\tau^z\}$,$\{\tau^z\}$	U1,U5
Z25	$\{\tau^z\}$	$\{\tau^z\}$,$\{-\tau^z\}$	$\{\tau^x,\tau^z\}$,$\{\tau^x,-\tau^z\}$	$\{\tau^z\}$,$\{\tau^z\}$	U3

TABLE III. Symmetry-allowed mean-field parameters for different $\mathbb{Z}_2$ *Ansätze*. The reference bonds are illustrated in Fig. 2(c). The parent U(1) states corresponding to each $\mathbb{Z}_2$ *Ansatz* are also indicated. $\mathbb{Z}_2$ *Ansätze* that directly descend from a parent SU(2) state are labeled as class A, with an SU(2) flux of π threading the hexagonal loop. The associated PSGs of these *Ansätze* are listed in Table X.

straint of having nonzero mean-field amplitudes only on the three types of nearest-neighbor bonds.

We classify the *Ansätze* into four distinct classes—A, B, C, and D—based on the flux ϕ_h threading the hexagonal plaquette ($\theta = 0$ or π), and the spatial modulation of the mean-field amplitudes, which determines whether the unit cell must be enlarged. All the U(1) Ansätze are graphically illustrated in Fig. 3 and the corresponding PSGs are enlisted in appendix (Table IX).

1. Class A

Class A *Ansätze* are characterized by a vanishing flux through the hexagonal plaquettes, i.e., $\phi_h = 0$. There are two U(1) *Ansätze* in this class. The labeling of the bonds is defined in Fig. 2(c), and the graphical representations of these *Ansätze* are provided in Figs. 3(a) and 3(b).

These *Ansätze* can be further distinguished by the fluxes threading the square and triangular loops. In the U1 family, all loop fluxes vanish, i.e., $\phi_s = 0$ and $(\phi_{t_1}, \phi_{t_2}) = (0, 0)$. In contrast, the U2 states are characterized by $\phi_s = \pi$ and $(\phi_{t_1}, \phi_{t_2}) = (0, \pi)$.

2. Class B

Class B *Ansätze* feature a π-flux through the hexagonal plaquettes, i.e., $\phi_h = \pi$. Their realization necessitates a doubling of the unit cell along the T_1 direction, due to sign-alternating mean-field amplitudes on the zigzag bonds. Explicitly, denoting the zigzag bonds within the

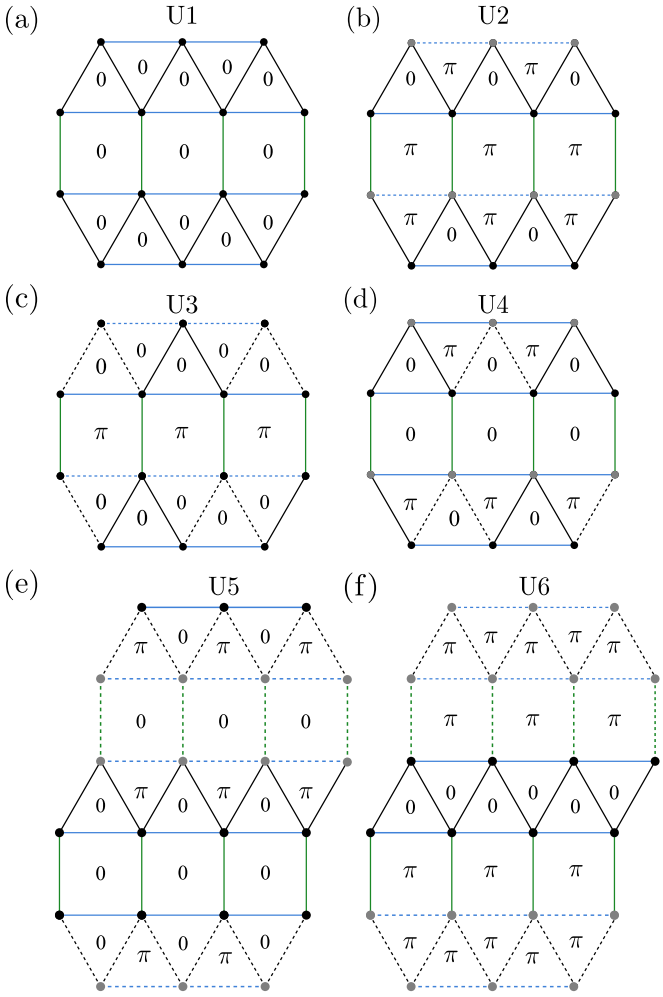


FIG. 3. Schematic representation of the class A, B, and C *Ansätze*, described in Secs. IV A 1, IV A 2, and IV A 3, respectively. Solid (dashed) lines indicate hoppings with positive (negative) signs. The green, blue, and black lines correspond to $\chi_v\tau^z$, $\chi_h\tau^z$, and $\chi_z\tau^z$, respectively. Black (gray) points represent positive (negative) onsite hoppings. The associated PSGs of these *Ansätze* are listed in Table IX.

(x, y) unit cell as $u_z(x, y)$ and $u'_z(x, y)$, their modulation follows:

$$u_z(x, y) = (-1)^x u_z, \tag{49}$$
$$u'_z(x, y) = (-1)^x u'_z. \tag{50}$$

This class contains two *Ansätze*, labeled U3 and U4, illustrated in Fig. 3(c) and 3(d), respectively. For U3, $\phi_s = \pi$ and $(\phi_{t_1}, \phi_{t_2}) = (0, 0)$, whereas for U4, $\phi_s = 0$ and $(\phi_{t_1}, \phi_{t_2}) = (0, \pi)$.

3. Class C

Class C *Ansätze* also exhibit zero flux through the hexagonal plaquettes, but differ from class A in the spatial modulation of the amplitudes. In this case, the unit cell is doubled along the T_2 direction, with the mean-field amplitudes modulated as

$$u_{v,h,z}(x, y) = (-1)^y u_{v,h,z}, \tag{51}$$
$$u'_{h,z}(x, y) = (-1)^y u'_{h,z}, \tag{52}$$
$$a'_{\mu,u} = (-1)^y a_{\mu,u}. \tag{53}$$

This class includes two *Ansätze*, labeled U5 and U6, depicted in Fig. 3(e) and 3(f). For U5, the square flux vanishes and the triangular fluxes alternate with the unit cell's position along T_2: $(\phi_{t_1}, \phi_{t_2}) = (0, \pi)$ or $(\pi, 0)$. For U6, $\phi_s = \pi$, and $(\phi_{t_1}, \phi_{t_2}) = (0, 0)$ or (π, π) depending on the T_2 position.

4. Class D

In Class D, the size of the unit cell depends on the value of the phase $\theta \notin \{0, \pi\}$. While the amplitudes on the J_v and J_h bonds remain translationally invariant, the zigzag bond amplitudes vary spatially as

$$u_z(x, y) = \mathcal{F}_z(-x\theta)u_z, \tag{54}$$
$$u'_z(x, y) = \mathcal{F}_z(-x\theta)u'_z, \tag{55}$$

where, as before, $\mathcal{F}_z(\xi) = \exp(i\xi\tau^z)$. This modulation is periodic only when $\theta = p\pi/q$ for integers p and q. The corresponding *Ansatz* then requires an enlarged unit cell of size q along T_1. For example, $\theta = \pi/3$ implies a tripled unit cell, while $\theta = \pi/4$ requires quadrupling.

The associated flux through the hexagonal loop is $\phi_h = p\pi/q$, which is one realization of the $\mathrm{U1}^p_q$ PSGs, leading to an infinite number of $\mathrm{U1}^p_q$ *Ansätze* [69]. As the horizontal bond amplitudes vanish in these *Ansätze*, no square or triangular fluxes exist. Although the resulting fluxes differ from 0 or π — the usual values for time-reversal–invariant hoppings with real amplitudes— these fractional fluxes, in appropriate gauges, alternate in sign between up and down spins, thereby preserving time-reversal symmetry [80]. It is worth noting that a chiral spin liquid is realized when nontrivial (not 0 or π) fluxes thread odd-sided loops.

B. $\mathbb{Z}_2$ *Ansätze*

All gauge-inequivalent *Ansätze* with IGG $\simeq \mathbb{Z}_2$ are enumerated in Table III, yielding a total of 25 distinct $\mathbb{Z}_2$ mean-field *Ansätze*.

The emergence of $\mathbb{Z}_2$ *Ansätze*, as descendants from different parent states, can occur through two mechanisms: (1) the first route involves adding symmetry-allowed pairing terms to an existing U(1) *Ansatz*, thereby modifying the IGG from U(1) to $\mathbb{Z}_2$; (2) alternatively, $\mathbb{Z}_2$ *Ansätze* can be obtained via directly breaking the symmetry down from an SU(2) IGG to $\mathbb{Z}_2$. The associated PSGs are

tabulated in Table X. In this case, two distinct SU(2) parent states are possible, characterized by 0- and π-flux threading the hexagonal plaquettes. These states feature vanishing mean-field amplitudes on the horizontal bonds and are continuously connected to the 0- and π-flux SU(2) spin liquids previously studied on the honeycomb lattice [77, 112].

Out of all the possible PSG solutions, No. 17 and No. 8 *Ansätze* arise from the PSG classes corresponding to the second and fifth rows of Table II, respectively. The remaining PSG classes do not permit a full reduction of the SU(2) IGG down to $\mathbb{Z}_2$, and thus do not yield viable $\mathbb{Z}_2$ spin liquids within our short-range framework. The Z1 state in Table III corresponds to the nonprojective (linear) representation of the space group with s-wave hoppings and pairings, and is a fully gapped $\mathbb{Z}_2$ QSL.

The last column of Table III documents the U(1) or SU(2) parent state from which each $\mathbb{Z}_2$ *Ansatz* descends. Entries labeled with "A" refer to the SU(2) π-flux state, which are obtained via mechanism (2).

V. QUANTUM SPIN LIQUID PHASES

It is important to note that the PSG classification and the subsequent analysis of mean-field band structures address a question that is logically distinct from energetic stabilization in a specific microscopic Hamiltonian. The PSG framework enumerates all symmetry-allowed quantum spin liquid *Ansätze* on the trellis lattice, independent of their variational energies, and thereby identifies the full landscape of possible fractionalized phases. Within this space, the semi-Dirac spin liquid emerges as a distinct symmetry-allowed state characterized by a linear-quadratic spinon dispersion at high-symmetry points in the Brillouin zone. Whether such a state is realized as the ground state of a particular spin Hamiltonian is a separate, model-dependent question that requires energetic optimization or unbiased numerical methods. In the present work, we find that the nearest-neighbor Heisenberg model on the trellis lattice does not energetically stabilize the semi-Dirac spin liquid, which therefore remains a phase realized at the level of PSG classification and mean-field parameter space rather than in the optimized phase diagram of the physical spin model. This distinction is generic to PSG-based studies and does not diminish the conceptual significance of the semi-Dirac spin liquid as a symmetry-allowed quantum spin liquid with characteristic universal properties. This separation between PSG classification and energetic selection is standard in parton-based approaches [69, 78, 113].

The properties of the *Ansätze* identified above depend on the choice of mean-field parameters, which are, in turn, determined by minimizing the energy with respect to a specific Hamiltonian. Consequently, the physical characteristics of each *Ansatz* are inherently model dependent. In this section, however, instead of initially focusing on such microscopic details, we choose to first analyze the *general* features of the six U(1) *Ansätze*. Thereafter, we relate these findings to the physics of the nearest-neighbor Heisenberg model with $J_h - J_v - J_z$ couplings via a fully self-consistent calculation.

A. Mean-field phase diagrams

The unit cell of the trellis lattice contains three inequivalent bonds, each characterized by a hopping amplitude: χ_h, χ_v, and χ_z. By independently varying these parameters, we uncover a rich variety of phases, including both gapped and gapless states exhibiting Fermi surfaces (FSs), nodal lines, semi-Dirac and Dirac points. We now present a detailed discussion of these phases for all six U(1) *Ansätze* as well as their associated band structures. For clarity, we set $\chi_h = 1$ throughout the analysis.

Among the six U(1) *Ansätze*, the U1 family exhibits the most intricate phase diagram, as shown in Fig. 4(a). Specifically, we observe extended windows of Dirac spin liquid (DSL), FS, and gapped phases, delineated in the parameter space defined by χ_z and χ_v. Each phase is distinguished by its band structure and excitation spectrum near the Fermi energy, illustrated in Fig. 4(d) for representative parameter values marked by colored dots in the phase diagram. Here, the phase boundary between the DSL and FS phases is specified by $\chi_v = -2\chi_z + \chi_z^2$, while the boundary between the FS and gapped phases is given by $\chi_v = 2 + \chi_z + \chi_z^2/8$.

Additional noteworthy features appear at the DSL's boundaries. For instance, the blue circle at $\chi_v = 0$ marks a nodal-line spin liquid phase. Moreover, along a segment of the line $\chi_v = 2\chi_z$, we find a *semi-Dirac* spin liquid (labeled s-DSL) [114]. In this semi-Dirac phase, the bands touch at the point $K_3 = (0, 2\pi/3)$, at which the dispersion is linear along one momentum direction and quadratic along the orthogonal one[1]. Consequently, quasiparticles are effectively massive in one direction, while exhibiting massless Dirac-like behavior in the other. Notably, the semi-Dirac point acts as a precursor to the Dirac points that characterize the DSL phase (as discussed in Sec. V B below; see also Fig. 5). Here, we note that this U1 *Ansatz* includes the semi-Dirac dispersion observed in the tight-binding honeycomb model of Refs. [121, 122]. This connection is established by including further-neighbor amplitudes on the trellis lattice –namely, the diagonal links within the square plaquettes and the longest vertical link within the hexagonal plaquette –in addition to those shown in Fig. 3(a). The s-DSL nodes emerge when $\chi_v = \chi_z = \chi$, $\chi_h = 0$, and the hopping amplitude

[1] Interestingly, similar band structures also appear in other contexts [115] including in studies of Kitaev spin liquids [116], and topological materials [117–120].

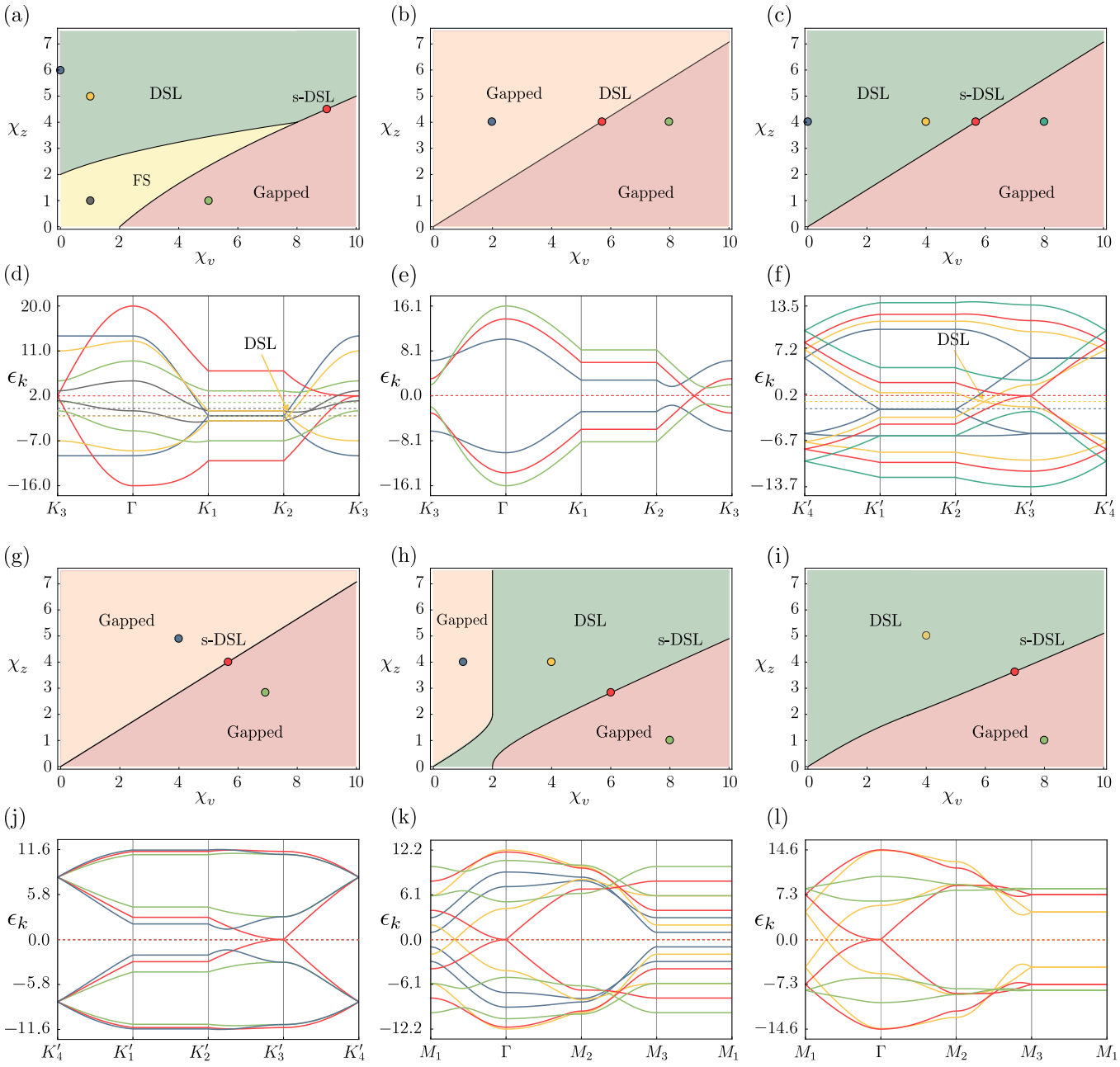


FIG. 4. Phase diagrams of the six U(1) *Ansätze* (a) U1, (b) U2, (c) U3, (g) U4, (h) U5, and (i) U6 in the (χ_v, χ_z) parameter space, with $\chi_h = 1$ fixed. The corresponding band structures for representative points, indicated by colored circles, are shown in panels (d)–(f) and (j)–(l), respectively. (d), (e) The energy dispersions are plotted along a high-symmetry path $K_3 \to \Gamma \to K_1 \to K_2 \to K_3$ in the Brillouin zone, where $K_3 = (0, 2\pi/3)$, $\Gamma = (0, 0)$, $K_1 = (2\pi/3, 0)$, and $K_2 = (2\pi/3, 2\pi/3)$. (f), (j) The band dispersions are plotted along a path that connects the momenta $K_4' = (\pi/3, \pi/6)$, $K_1' = (0, \pi/6)$, $K_2' = (0, \pi/2)$, $K_3' = (\pi/3, \pi/2)$, and back to K_4'. (k), (l) The spectra are displayed along the path $M_1 \to \Gamma \to M_2 \to M_3 \to M_1$, with $M_1 = (2\pi/3, 0)$, $\Gamma = (0, 0)$, $M_2 = (0, \pi/3)$, and $M_3 = (2\pi/3, \pi/3)$. In all cases, dashed lines indicate the Fermi energy.

on these further-neighbor links is set to $\chi/3$. The DSL, FS, s-DSL, and gapped phases all meet at a multicritical point $(\chi_v, \chi_z) = (8, 4)$.

Proceeding along the same lines, the phase diagram for the U2 *Ansatz* is shown in Fig. 4(b). It features two gapped phases separated by a gapless Dirac spin liquid phase, which lies along the line $\chi_v = \sqrt{2}\chi_z$. Representative band structures at selected points of this phase diagram are displayed in Fig. 4(e). In this case, the Dirac point lies along the momentum path between the $K_2 = (2\pi/3, 2\pi/3)$ and K_3 points in reciprocal space.

Next, Fig. 4(c) showcases the phase diagram for the U3 *Ansatz*. At $\chi_v = 0$, this exhibits a nodal-line phase, with the nodal line itself stretching between $K_1' = (0, \pi/6)$ and

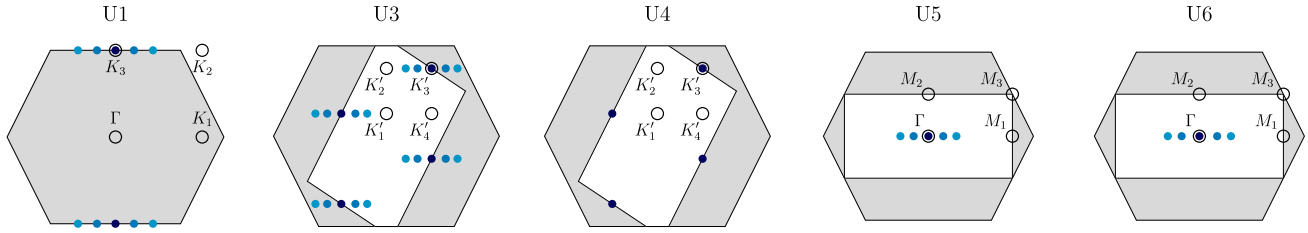


FIG. 5. Evolution of the Dirac points as the system approaches the s-DSL phase from the DSL phase for the *Ansätze* U1, U3, U4, U5, and U6 (see Fig. 3). The color intensity increases with progression toward the s-DSL, where two Dirac points merge to form the s-DSL. Each pair of dots with identical color corresponds to a particular value of the hopping parameter close to the s-DSL transition (see Fig. 4). The U4 s-DSL state is separated from the others by two intermediate gapped phases. Hollow circles mark the momentum-space path along which the dispersions are displayed in Fig. 4.

$K_2' = (0, \pi/2)$. Upon increasing χ_v, a Dirac spin liquid appears but with a tilted cone located along the path between K_2' and $K_3' = (\pi/3, \pi/2)$, [123, 124]. As χ_v is increased even further, an s-DSL phase emerges that subsequently transitions into a gapped phase. The semi-Dirac spin liquid located along the line $\chi_v = \sqrt{2}\chi_z$ thus separates the DSL and gapped phases. It is characterized by a linear-quadratic dispersion centered at K_3', and the tilted Dirac cone of the DSL phase in fact originates from the semi-Dirac point (see Sec. V B below). The corresponding band structures are all plotted in Fig. 4(f).

Similarly, the U4 *Ansatz*'s phase diagram is shown in Fig. 4(g). It comprises two distinct gapped phases separated by a semi-Dirac spin liquid phase (black line) occurring, as before, along $\chi_v = \sqrt{2}\chi_z$. The associated band structures are presented in Fig. 4(j). Unlike for the U1 *Ansatz*, the semi-Dirac point here does not split into a pair of Dirac points and the spectrum remains gapped on either side of the s-DSL; however, such a splitting could be induced by incorporating further-neighbor hopping terms.

Continuing with our sequence of U(1) QSLs, Fig. 4(h) presents the phase diagram for the U5 *Ansatz*, wherein a DSL region is enclosed between two gapped phases. The DSL phase is bounded by the curves

$$\begin{aligned} \chi_v &= \frac{\chi_z}{2}\sqrt{8-\chi_z^2} \quad (\text{for } \chi_z < 2), \\ \chi_v &= 2, \qquad\qquad\quad (\text{for } \chi_z \geq 2), \\ \chi_v &= 2\sqrt{1+\chi_z^2}. \end{aligned} \tag{56}$$

At the boundary between the DSL and the gapped phase below it, we once again find semi-Dirac dispersion. The related band structures are illustrated in Fig. 4(k).

Finally, the phase diagram for the U6 *Ansatz* is shown in Fig. 4(i). The topology of the phase diagram closely resembles that for the U3 case, and an s-DSL phase separates the DSL and gapped phases. The phase boundaries for the semi-Dirac region are defined by

$$\chi_v = \frac{\chi_z}{2}\sqrt{8+\chi_z^2} \quad (\text{for } \chi_z < 2), \tag{57}$$

$$\chi_z = \frac{1}{2}\sqrt{4+\chi_v^2} \quad (\text{for } \chi_z \geq 2). \tag{58}$$

The associated spinon dispersions for this *Ansatz* are sketched in Fig. 4(l).

The s-DSL boundaries for all the *Ansätze* are tabulated in Table IV.

Ansatz	s-DSL boundaries
U1	$\chi_v = 2\chi_z$ for $\chi_z > 4$
U3	$\chi_v = \sqrt{2}\chi_z$
U4	$\chi_v = \sqrt{2}\chi_z$
U5	$\chi_v = 2\sqrt{1+\chi_z^2}$
U6	$\begin{cases} \chi_v = \frac{\chi_z}{2}\sqrt{8+\chi_z^2} & \text{for } \chi_z < 2 \\ \chi_z = \frac{1}{2}\sqrt{4+\chi_v^2} & \text{for } \chi_z \geq 2 \end{cases}$

TABLE IV. The equations for the phase boundaries realizing s-DSL for each of the U(1) *Ansätze*.

While our analysis of the semi-Dirac *Ansätze* has focused on a U(1) gauge structure, one can also realize $\mathbb{Z}_2$ semi-Dirac *Ansätze* since their origin is rooted in the lattice (point group) symmetry.

B. Properties of the semi-Dirac spin liquid state

1. *Origin and symmetry considerations*

To better understand the transition from the DSL to the s-DSL identified above, we analyze the motion of the Dirac points in the *Ansätze* labeled U1, U3, U4, U5, and U6 in Fig. 3. As the hopping parameters are tuned, the Dirac points shift gradually in momentum space, as represented by the increasing intensity of color in Fig. 5. This continuous motion ultimately drives two distinct Dirac points to merge, giving rise to the s-DSL. Each pair of identically colored dots in Fig. 5 corresponds to a specific choice of hopping parameter close to the critical

Ansatz (sign structure)	No. of s-DSL points / BZ	Positions within EBZ	$\boldsymbol{q}$-vectors connecting s-DSL points
U1 (Fig. 3(a))	1	$(0,\pm\frac{2\pi}{3}),(\pm\frac{4\pi}{3},0)$	$(0,\pm\frac{4\pi}{3}),(\pm\frac{8\pi}{3},0),(\pm\frac{4\pi}{3},\pm\frac{2\pi}{3})$
U3 (Fig. 3(c))	2	$\pm(\frac{\pi}{3},\frac{\pi}{2}),\ \pm(-\frac{\pi}{3},\frac{\pi}{6})$	$\pm(\frac{2\pi}{3},\pi),\ \pm(-\frac{2\pi}{3},\frac{\pi}{3}),\ \pm(\frac{2\pi}{3},\frac{\pi}{3}),\ \pm(0,\frac{2\pi}{3})$
U4 (Fig. 3(d))	2	$\pm(\frac{\pi}{3},\frac{\pi}{2}),\ \pm(-\frac{\pi}{3},\frac{\pi}{6})$	$\pm(\frac{2\pi}{3},\pi),\ \pm(-\frac{2\pi}{3},\frac{\pi}{3}),\ \pm(\frac{2\pi}{3},\frac{\pi}{3}),\ \pm(0,\frac{2\pi}{3})$
U5 (Fig. 3(e))	1	$(0,0)$	$(0,\pm\frac{2\pi}{3}),(\pm\frac{4\pi}{3},0),(\pm\frac{4\pi}{3},\pm\frac{2\pi}{3})$
U6 (Fig. 3(f))	1	$(0,0)$	$(0,\pm\frac{2\pi}{3}),(\pm\frac{4\pi}{3},0),(\pm\frac{4\pi}{3},\pm\frac{2\pi}{3})$

TABLE V. Summary of the observations from Fig. 5. For each U(1) *Ansatz* shown in Fig. 3, we list the number of s-DSL points within the Brillouin zone, their positions in the extended Brillouin zone (EBZ), and the corresponding $\boldsymbol{q}$-vectors connecting them.

regime where the s-DSL emerges (see Fig. 4). The observations such as the number of s-DSL points within the extended Brillouin zone (EBZ) and the corresponding q-vectors connecting them (see Fig. 5) are summarised in Table V.

In general, as underscored by Fig. 5, the merger of two Dirac nodes gives rise to a semi-Dirac node [91, 121]. Here, we demonstrate that a key requirement for this mechanism to work is that the *little* group at the band-touching momentum is the C_{2v} point group; i.e., it has twofold rotational symmetry and two orthogonal reflection planes. Let us consider a two-band Hamiltonian in the sublattice basis, which can be parameterized as

$$H(\boldsymbol{k}) = a(\boldsymbol{k})\varsigma^0 + \vec{d}(\boldsymbol{k})\cdot\vec{\varsigma}, \tag{59}$$

where ς^0 is the 2×2 identity matrix and $\vec{\varsigma}=\{\varsigma^x,\varsigma^y,\varsigma^z\}$ are Pauli matrices that act on the two sublattices. The C_{2v} point group consists of two mirror reflections, σ_x and σ_y, and a C_2 rotation. Under these operations, the Hamiltonian transforms as

$$\mathcal{U}_{\mathcal{O}}H(\boldsymbol{k})\mathcal{U}_{\mathcal{O}}^{\dagger} = H(\mathcal{O}(\boldsymbol{k})) \quad \text{for} \quad \mathcal{O}\in\{M_x,M_y,C_2\}, \tag{60}$$

with the corresponding sublattice transformation matrices

$$\mathcal{U}_{\sigma_x}=\varsigma^x, \quad \mathcal{U}_{\sigma_y}=\varsigma^0, \quad \mathcal{U}_{C_2}=\varsigma^x. \tag{61}$$

The σ_x symmetry constrains the Hamiltonian's coefficients as follows:

$$\begin{aligned} d_x(k_x,-k_y) &= d_x(k_x,k_y),\\ d_y(k_x,-k_y) &= -d_y(k_x,k_y),\\ d_z(k_x,-k_y) &= -d_z(k_x,k_y), \end{aligned} \tag{62}$$

implying that $d_x(\boldsymbol{k})$ is even in k_y, while $d_y(\boldsymbol{k})$ and $d_z(\boldsymbol{k})$ are odd in k_y. Similarly, for $\mathcal{O}=\sigma_y$, Eq. (59) yields $H(-k_x,k_y)=H(k_x,k_y)$, implying that all components of $\vec{d}(\boldsymbol{k})$ are even in k_x. The C_2 operation imposes no additional constraints since $C_2=\sigma_x\sigma_y$. The scalar function $a(\boldsymbol{k})$ is always even in both k_x and k_y.

With these symmetry constraints in place, we construct a minimal model that yields a semi-Dirac nodal structure. Keeping only the leading symmetry-allowed terms consistent with a single mirror-protected linear dispersion along k_y, we choose

$$\begin{aligned} d_x(\boldsymbol{k}) &= m - m_0k_x^2,\\ d_y(\boldsymbol{k}) &= vk_y,\\ d_z(\boldsymbol{k}) &= a(\boldsymbol{k}) = 0. \end{aligned} \tag{63}$$

The resulting minimal Hamiltonian is

$$H(\boldsymbol{k}) = (m-m_0k_x^2)\sigma^x + vk_y\sigma^y, \tag{64}$$

with spectrum

$$E(\boldsymbol{k}) = \pm\sqrt{v^2k_y^2+(m-m_0k_x^2)^2}. \tag{65}$$

For $m_0>0$, there exist three distinct regimes:

1. $m>0$: Two Dirac nodes appear at $k_y=0$ and $k_x=\pm k_0=\pm\sqrt{m/m_0}$. Expanding around $k_x=\pm k_0$ yields $m-m_0(k_0+\delta k_x)^2\approx -2m_0k_0\delta k_x$, showing that each node is a Dirac point with velocities $(v_x,v_y)=(2m_0k_0,v)$.

2. $m=0$: The two Dirac nodes merge, producing the dispersion

$$E(\boldsymbol{k}) = \pm\sqrt{v^2k_y^2+m_0^2k_x^4}\sim \pm vk_y,\ \pm m_0k_x^2. \tag{66}$$

   At $m=0$, the two Dirac cones merge into a semi-Dirac node, exhibiting quadratic dispersion along k_x and linear dispersion along k_y.

3. $m<0$: No nodal points exist, and a gap opens.

This minimal model thus captures the essential mechanism underlying the transition from a Dirac spin liquid to a gapped spin liquid through an intermediate semi-Dirac spin liquid. In particular, this mechanism accounts for the transitions observed in the U1, U3, U5, and U6 *Ansätze*.

In contrast, higher little-group symmetries such as C_{3v}, C_{4v}, or C_{6v} are incompatible with the realization of semi-Dirac dispersions. To illustrate this, let us focus on C_{4v}. In this case, the presence of a term such as $vk_y\sigma^y$ would,

by virtue of C_4 rotational symmetry, require the existence of an equivalent linear term along the k_x direction, thereby enforcing full Dirac-like dispersions in both momentum directions. To formalize this argument, we generalize the matrices $\mathcal{U}_{\mathcal{O}}$ to pseudospin representations. These pseudospin matrices must be consistent with how the underlying physical degrees of freedom (e.g., spin, orbital, sublattice) transform under the operations of the point group, while simultaneously respecting the group multiplication rules (up to projective phases). For C_{4v}, the symmetry group is generated by σ_x and C_4, for which we adopt the representation

$$\mathcal{U}_{\sigma_x} = \varsigma^x, \quad \mathcal{U}_{C_4} = ie^{i\frac{\pi}{4}\varsigma^z}. \tag{67}$$

Since $\mathcal{U}_{\sigma_x}$ coincides with the choice made in the C_{2v} case, it imposes the same constraints as Eq. (62), leading to the low-energy expansion

$$\begin{aligned} d_x(\boldsymbol{k}) &= a_x k_x + b_x k_y^2 + O(k_x^2) + O(k_y^4), \\ d_y(\boldsymbol{k}) &= b_y k_y + O(k_y^3), \\ d_z(\boldsymbol{k}) &= b_z k_y + O(k_y^3). \end{aligned} \tag{68}$$

The additional constraints from C_4 symmetry read

$$\begin{aligned} d_x(-k_y, k_x) &= -d_y(k_x, k_y), \\ d_y(-k_y, k_x) &= d_x(k_x, k_y), \\ d_z(-k_y, k_x) &= d_z(k_x, k_y). \end{aligned} \tag{69}$$

The first two conditions enforce $a_x = b_y$, while simultaneously requiring $d_z = 0$. Consequently, the presence of a linear $b_y k_y$ term in d_y necessitates the appearance of an equivalent $b_y k_x$ term in d_x. This enforces linear dispersions along both momentum directions, thereby ruling out the semi-Dirac scenario. An analogous argument applies to other little groups with higher symmetries, such as C_{6v}. We thus conclude that C_{2v} constitutes a special case: It provides precisely the symmetry constraints necessary to stabilize semi-Dirac nodes, whereas higher point-group symmetries inevitably restore full Dirac dispersions.

2. *Spin-spin correlation functions*

Having established the origin of the s-DSL state, we now turn to its correlation functions. To compute equal-time spin-spin correlations, it is convenient to rewrite the spins using the Abrikosov-fermion representation of Eq. (2). In this formulation, the Heisenberg exchange becomes a four-fermion term, which we decouple at the mean-field level in the hopping channel, yielding a quadratic spinon Hamiltonian. Diagonalizing this mean-field Hamiltonian gives the spinon eigenmodes $\psi_n(i)$ and their energies. The mean-field ground state is then obtained by filling the lowest half of these modes, from which we construct the single-particle Green's function

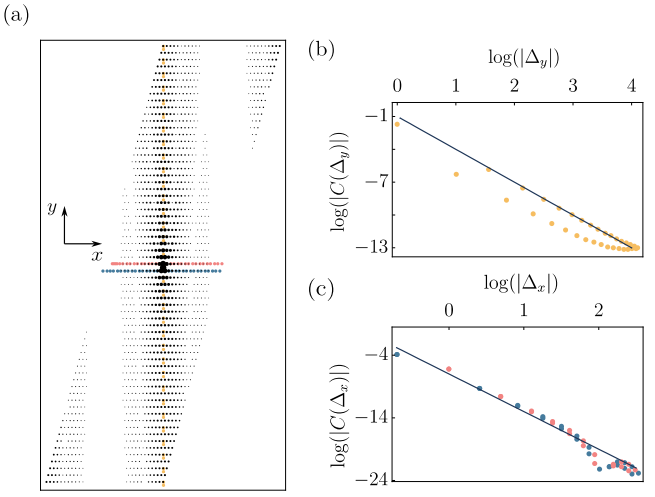


FIG. 6. (a) Real-space two-spin correlation decay for the U1 *Ansatz* in the s-DSL phase at the mean-field level. The colored vertical and horizontal lines mark the directions analyzed in panels (b) and (c). The displacement variables are defined as $\Delta_y = y - y_0$ and $\Delta_x = x - x_0$, with (x_0, y_0) labeling the reference site. The functions $C(\Delta_y)$ and $C(\Delta_x)$ denote the spin-spin correlations along the vertical and horizontal directions, respectively. (b) Along the vertical (y) direction, correlations decay with exponent ≈ 3. (c) Along the two horizontal slices, correlations decay faster, with exponent ≈ 6.

$G_{ij} = \sum_{n\in\text{occ}} \psi_n^*(i)\psi_n(j)$. Wick's theorem allows us to express the physical spin–spin correlator entirely in terms of G_{ij} as $\langle \hat{\mathbf{S}}_i \cdot \hat{\mathbf{S}}_j \rangle \sim -|G_{ij}|^2$, so that the spatial decay of the spin correlations follows directly from the numerically evaluated $|G_{ij}|^2$.

Figure 6 presents the real-space decay of the spin-spin correlations for the U1 *Ansatz* in the s-DSL phase with hopping parameters $\chi_h = 1.0$, $\chi_v = 9.0$, and $\chi_z = 4.5$ (see Figs. 3 and 4). In panel (a), the radius of the black disks represents the correlation strength, while the colored vertical and horizontal lines indicate the directions analyzed in panels (b) and (c). Panel (b) shows that correlations along the vertical (y) direction decay with exponent ≈ 3, whereas panel (c) demonstrates that correlations along the two horizontal cuts decay much more rapidly, with exponent ≈ 6.

These exponents could be understood as follows. In the long-wavelength limit, the dispersion of the s-DSL can be approximated as

$$E(\boldsymbol{k}) = mk_1^2 + k_2. \tag{70}$$

The corresponding low-energy effective theory is obtained by adding a quadratic anisotropic term (mass) to the massless Dirac Lagrangian in $(1+1)$D:

$$\mathcal{L} = \bar{\psi}\left(i\gamma^\mu \partial_\mu - m\,\partial_1^2\right)\psi, \tag{71}$$

where $\mu = 0, 2$ and $\bar{\psi} = \gamma^0\psi^\dagger$. In $(2+1)$D, the Green's function satisfies

$$\left(i\gamma^\mu \partial_\mu - m\,\partial_1^2\right)\mathcal{G}(\boldsymbol{r} - \boldsymbol{r}') = \delta^3(\boldsymbol{r} - \boldsymbol{r}'). \tag{72}$$

Here, we temporarily use the notation $\boldsymbol{r} \equiv (r_0, r_1, r_2)$ to denote a three-vector in which the first component is a time coordinate and the other two are Cartesian coordinates. Using the Fourier transform

$$\mathcal{G}(\boldsymbol{r}-\boldsymbol{r}') = \int \frac{d^3\boldsymbol{k}}{(2\pi)^3} e^{i\boldsymbol{k}\cdot(\boldsymbol{r}-\boldsymbol{r}')} G(\boldsymbol{k}), \tag{73}$$

we obtain the Green's function in momentum space:

$$G(\boldsymbol{k}) = \frac{1}{\gamma^\mu k_\mu + m k_1^2} = \frac{\gamma^\mu k_\mu - m k_1^2}{k_\mu^2 - m^2 k_1^4}. \tag{74}$$

To analyze the spatial decay of correlations, we consider the real-space Green's function $\mathcal{G}(\boldsymbol{r})$, obtained by Fourier transforming over spatial components:

$$\mathcal{G}(\boldsymbol{r}) = \int \frac{d^2q\, dk_1}{(2\pi)^3} e^{i\boldsymbol{k}\cdot\boldsymbol{r}} \frac{\gamma^\mu q_\mu - m k_1^2}{q_\mu^2 - m^2 k_1^4}, \tag{75}$$

where $\boldsymbol{k} = (q_0, k_1, q_2)$ separates the $\mu = 0, 2$ components [the (1+1)D Dirac piece] from the anisotropic momentum k_1.

We can now carry out a simple scaling analysis that proves informative. In order to ascertain the asymptotic behavior of $\mathcal{G}(x, y)$ at large distances, we employ the anisotropic scaling: $r_0 \sim \tilde{r}_0 \Lambda$, $r_1 \sim \tilde{r}_1 \Lambda^{1/2}$, and $r_2 \sim \tilde{r}_2 \Lambda$. With the rescaling $k_0 \to \tilde{k}_0/\Lambda$, $k_1 \to \tilde{k}_1/\Lambda^{1/2}$, and $k_2 \to \tilde{k}_2/\Lambda$, Eq. (75) becomes

$$\mathcal{G}(\Lambda\tilde{r}_0, \Lambda^{1/2}\tilde{r}_1, \Lambda\tilde{r}_2) = \Lambda^{-3/2}\mathcal{G}(\tilde{r}_0, \tilde{r}_1, \tilde{r}_2). \tag{76}$$

For equal-time correlations, we set $r_0 = 0$, yielding

$$\mathcal{G}(\Lambda^{1/2}\tilde{r}_1, \Lambda\tilde{r}_2) = \Lambda^{-3/2}\mathcal{G}(\tilde{r}_1, \tilde{r}_2). \tag{77}$$

The dependence along the two directions can then be straightforwardly extracted. Along r_1, we set $r_2 = 0$ and choose $\Lambda = r_1^2$, such that $\tilde{r}_1 = 1$. This gives $\mathcal{G}(r_1, 0) \sim r_1^{-3}$. Likewise, along r_2, we set $r_1 = 0$ and choose $\Lambda = r_2$, such that $\tilde{r}_2 = 1$; this shows that $\mathcal{G}(0, r_2) \sim r_2^{-3/2}$.

The equal-time correlator is defined as

$$\begin{aligned}\mathcal{S}_{+-}(\boldsymbol{r}-\boldsymbol{r}') &= \langle S^+(\boldsymbol{r}) S^-(\boldsymbol{r}')\rangle \\ &= \left\langle f_\uparrow^\dagger(\boldsymbol{r}) f_\downarrow(\boldsymbol{r}) f_\downarrow^\dagger(\boldsymbol{r}') f_\uparrow(\boldsymbol{r}')\right\rangle \\ &= -\left\langle f_\uparrow^\dagger(\boldsymbol{r}) f_\uparrow(\boldsymbol{r}')\right\rangle \left\langle f_\downarrow^\dagger(\boldsymbol{r}) f_\downarrow(\boldsymbol{r}')\right\rangle^\star, \end{aligned} \tag{78}$$

where, in the last step, we use Wick's theorem. Defining the equal-time two-point correlator as $\mathcal{G}_\sigma(\boldsymbol{r}-\boldsymbol{r}') = \langle f_\sigma^\dagger(\boldsymbol{r}) f_\sigma(\boldsymbol{r}')\rangle$, we can write

$$\mathcal{S}_{+-}(\boldsymbol{r}-\boldsymbol{r}') = \mathcal{G}_\uparrow(\boldsymbol{r}-\boldsymbol{r}')\mathcal{G}_\downarrow^\star(\boldsymbol{r}-\boldsymbol{r}'). \tag{79}$$

By virtue of spin-rotation symmetry, this reduces to

$$\mathcal{S}_{+-}(\boldsymbol{r}-\boldsymbol{r}') = -|\mathcal{G}(\boldsymbol{r}-\boldsymbol{r}')|^2, \tag{80}$$

implying

$$\mathcal{S}_{+-}(\boldsymbol{r}-\boldsymbol{r}') \sim \begin{cases} |r_1 - r_1'|^{-6}, & \text{if } r_2 - r_2' = 0; \\ |r_2 - r_2'|^{-3}, & \text{if } r_1 - r_1' = 0. \end{cases} \tag{81}$$

This reproduces the decay observed in Fig. 6. To fully capture all the fine oscillatory features of the spin–spin correlation function, it is necessary to evaluate the complete integral over the Brillouin zone in Eq. (75). A detailed analysis of this behavior is left for future work. We note that all along the phase boundary separating the DSL and gapped state shown in Fig.4(a), we realize a semi-Dirac spinon dispersion including at the multicritical point. These mean-field exponents should be compared with those in other gapless phases, such as a spinon Fermi surface state ($\sim r^{-3}$) [125–127] and Dirac spin liquid ($\sim r^{-4}$) [128]. Since the semi-Dirac dispersion originates from a merger of two Dirac cones that introduces a length scale, i.e., the inverse of the distance between the two Dirac cones, it would be interesting to explore how the $\sim r^{-4}$ decay of the Dirac spin liquid transforms into the anisotropic exponents of the semi-Dirac state.

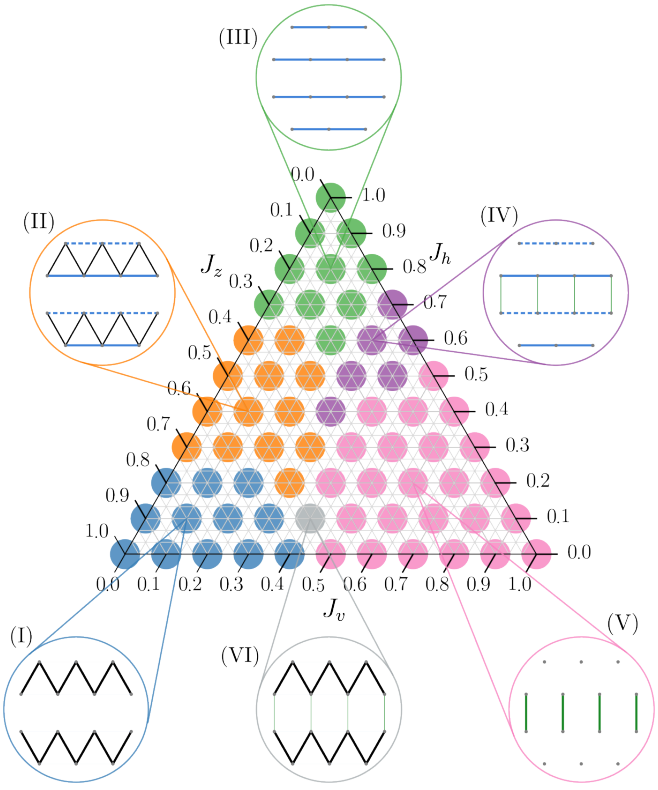


FIG. 7. The ternary phase diagram of the nearest-neighbor Heisenberg model on the trellis lattice with antiferromagnetic couplings J_h, J_v, and J_z as illustrated in Fig. 1(a), subject to $J_h + J_v + J_z = 1$. The six distinct regions colored here correspond to (I) zigzag-chain, (II) zigzag-ladder, (III) rung-chain, (IV) rung-ladder, (V) ladder-dimer, and (VI) honeycomb phases. Representative saddle-point structures are shown for selected points within each phase.

C. Ternary phase diagram of the Heisenberg model

Building on our analysis of the generic features of the *Ansätze*, we now investigate the phase diagram obtained from saddle-point solutions of a nearest-neighbor antiferromagnetic Heisenberg model with exchange couplings J_v along the vertical ladder legs, J_h along the horizontal rungs, and J_z on the zigzag interladder bonds, as depicted in Fig. 1(a). The analysis is performed by self-consistently determining all mean-field amplitudes.

The saddle-point solutions of six U(1) *Ansätze*, considered up to a doubling of the unit cell, are summarized in Fig. 7. Within the ternary parameter space, six distinct phases (I–VI) emerge. The graphical representation in Fig. 7 directly highlights the saddle-point structures of the *Ansätze*, with bond widths scaled according to the self-consistently determined mean-field amplitudes at representative points.

- In phase I (blue), the amplitudes on the J_v and J_h bonds are negligible for all *Ansätze*, resulting in an effective 1D zigzag chain structure. A representative point here is $(J_z, J_h, J_v) = (0.8, 0.1, 0.1)$ with optimized mean-field parameters $(\chi_z, \chi_h, \chi_v) = (0.642, -0.009, 0.003)$.

- In phase II (orange), realized by the *Ansätze* U2, U4, and U5 with 0- and π-staggered fluxes through triangular plaquettes, the amplitudes on the legs dominate, producing an effective zigzag ladder structure. At the point $(J_z, J_h, J_v) = (0.5, 0.4, 0.1)$, the optimized values are $(0.583, 0.352, -0.012)$.

- Phase III (green) corresponds to a rung-chain structure dominated by J_h bonds, with negligible amplitudes on J_v and J_z. For couplings $(J_z, J_h, J_v) = (0.1, 0.8, 0.1)$, the corresponding mean-field values are $(0.001, 0.636, 0.013)$.

- In phase IV (purple), a π-flux rung-ladder state appears, realized by the U2, U3, and U6 *Ansätze*. For $(0.1, 0.6, 0.3)$, the optimized amplitudes are $(0.000, 0.630, 0.192)$.

- In phase V (pink), all *Ansätze* collapse to a ladder-dimer phase due to vanishingly small χ_z and χ_h. At $(0.2, 0.2, 0.6)$, the optimized parameters are $(-0.004, -0.009, 0.999)$.

- Finally, at the junction of phases I, II, and V, a zero-flux honeycomb resonating-valence-bond-like state (phase VI) governs the low-energy behavior. Here, $\chi_h \sim -0.009$ is nearly zero, while $(\chi_z, \chi_v) \sim (0.636, -0.153)$. The relevant parent states include U1, U2, U5, and U6.

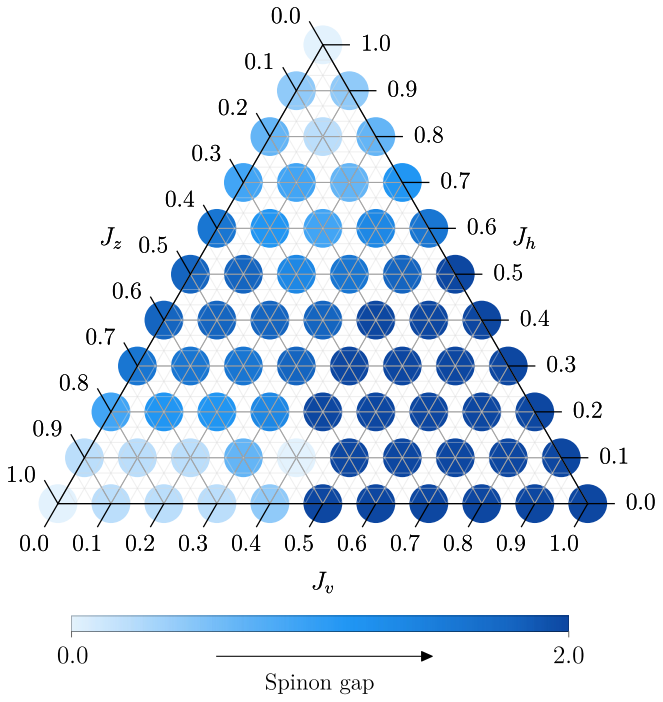


FIG. 8. Spinon excitation gap across the ternary phase diagram shown in Fig. 7. The color intensity represents the magnitude of the spinon gap, with the lowest intensity indicating gapless regions and higher intensity corresponding to an increasing excitation gap.

The isotropic point in the phase diagram, $J_z = J_h = J_v$ features a ladder-dimer state (phase V). In Fig. 8, we show the spinon-gap profile across the ternary phase diagram in Fig. 7. Although the effective low-energy states in phases (I) and (III)—which reduce to isolated one-dimensional chains—are expected to be gapless, we find a finite gap except at the special points $J_v = J_h = 0$ and $J_z = J_v = 0$ in these two phases, respectively. This is because, in addition to the dominant mean-field parameters χ_z and χ_h in phases (I) and (III), respectively, the remaining mean-field parameters remain small but nonzero. As a result, a finite gap emerges.

In our self-consistent mean-field analysis, we also considered all $\mathbb{Z}_2$ *Ansätze* but found them either to be higher

Phase	Couplings (J_z, J_h, J_v)	Hopping parameters (χ_z, χ_h, χ_v)
Zigzag chain (I)	$(0.8, 0.1, 0.1)$	$(0.642, -0.009, 0.003)$
Zigzag ladder (II)	$(0.5, 0.4, 0.1)$	$(0.583, 0.352, -0.012)$
Rung chain (III)	$(0.1, 0.8, 0.1)$	$(0.001, 0.636, 0.013)$
Rung ladder (IV)	$(0.1, 0.6, 0.3)$	$(0.000, 0.630, 0.192)$
Ladder dimer (V)	$(0.2, 0.2, 0.6)$	$(-0.004, -0.009, 0.999)$
Honeycomb (VI)	$(0.5, 0.1, 0.4)$	$(0.636, -0.009, -0.153)$

TABLE VI. Representative coupling strengths (J_z, J_h, J_v) and self-consistent hopping parameters (χ_z, χ_h, χ_v) for the points marked in the ternary phase diagram of Fig. 7.

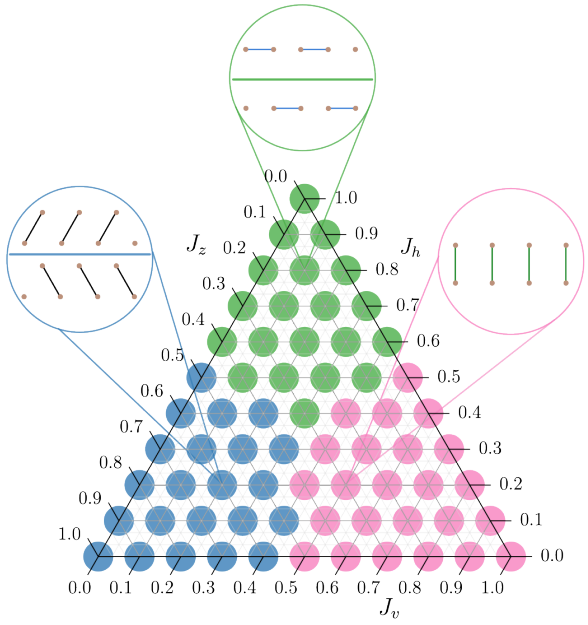


FIG. 9. Ternary phase diagram after symmetry reduction, consisting of three dimerized phases: Majumdar-Ghosh, rung dimer, and ladder-dimer phases, shown in blue, green, and pink, respectively. Realization of the Majumdar-Ghosh phase requires breaking σ_x, while the rung-dimer phase requires breaking T_1.

in energy than the corresponding U(1) states or to exhibit vanishing optimized pairing amplitudes (which are responsible for the $\mathbb{Z}_2$ gauge structure in the first place), thereby flowing back to their parent U(1) states. It would be interesting to assess their variational energetics after Gutzwiller projection and investigate whether the $\mathbb{Z}_2$ states are stabilized in some region of the phase diagram.

It is important to emphasize that the saddle-point phases described above assume full lattice and time-reversal symmetry. Certain paramagnetic phases, such as the Majumdar-Ghosh state [45], fall outside this fully symmetric framework. To capture these, one must consider symmetry-reduced versions of the *Ansätze*. For example, breaking σ_x yields a dimerized state with singlets on the zigzag bonds, corresponding to the Majumdar-Ghosh phase, which is twofold degenerate per zigzag ladder and is indicated in blue in Fig. 9. Similarly, breaking translational symmetry T_1 gives rise to a rung-dimer phase with singlets on the horizontal rungs, also twofold degenerate per rung, shown in green in Fig. 9. The ladder-dimer phase remains stable within its domain. Overall, we identify three distinct dimerized quantum paramagnetic phases.

VI. SPECTRAL PROPERTIES

To further characterize the quantum spin liquid states, we examine the time- and momentum-resolved spin-spin correlation function, namely, the DSF, defined as

$$\mathcal{S}^{\mu\nu}(\boldsymbol{q},\omega) = \int \frac{d\tau\, e^{i\omega\tau}}{2\pi N} \sum_{\langle i,j\rangle} e^{i\boldsymbol{q}\cdot(\boldsymbol{r}_i-\boldsymbol{r}_j)} \langle \mathbf{S}_i^{\mu}(\tau)\mathbf{S}_j^{\nu}(0)\rangle, \tag{82}$$

with $\mu,\nu = x,y,z$. The DSF is directly accessible in inelastic neutron scattering experiments and serves as a key probe of the spectral signatures of fractionalized excitations in QSLs.

In the following, we compute the DSF (and, where relevant, its frequency-integrated equal-time counterpart) using both mean-field theory (Figs. 10 and 11) and beyond-mean-field approaches (Fig. 12), including Keldysh pf-FRG and DMRG.

Before presenting the results, we clarify the scope of the comparison between mean-field and numerical approaches. We emphasize that the dynamical structure factors computed from the fermionic mean-field Ansätze should be interpreted as qualitative probes of the underlying parton band structures rather than as quantitative predictions for the physical spin model [69]. Although the microscopic exchange couplings (J_v, J_h, J_z) are fixed, the mean-field excitation spectrum is governed by *Ansatz*-dependent bond parameters that set the spinon bandwidth and are not uniquely determined by the bare exchanges alone. More fundamentally, the unprojected Abrikosov-fermion mean-field state relaxes the single-occupancy constraint and therefore does not reside in the physical spin Hilbert space; as a consequence, its dynamical correlators do not, in general, satisfy the exact sum rules of the spin Hamiltonian, including frequency-moment sum rules that relate moments of the dynamical structure factors to equal-time correlators and exchange couplings [1, 129]. By contrast, DMRG evaluates spin correlations strictly within the physical Hilbert space, while pf-FRG incorporates self-energy and vertex renormalizations derived from the microscopic Hamiltonian [130]. For this reason, absolute energy scales, spectral weights, and detailed line shapes obtained at the mean-field level are not expected to quantitatively match those of pf-FRG or DMRG, even when expressed in units of J. Throughout, we therefore restrict comparisons to qualitative momentum-space features and trends, which nevertheless provide valuable insight into the symmetry properties and structure of the underlying fractionalized excitations.

A. Mean-field results

Owing to SU(2) spin-rotation symmetry, it suffices to compute only the longitudinal component of the DSF

$$\mathcal{S}^{zz}(\boldsymbol{q},\omega) = \int_{-\infty}^{+\infty} \frac{d\tau\, e^{i\omega\tau}}{2\pi N} \sum_{i,j} e^{i\boldsymbol{q}\cdot\boldsymbol{r}_{ij}} \langle \hat{S}_i^z(\tau)\hat{S}_j^z(0)\rangle, \tag{83}$$

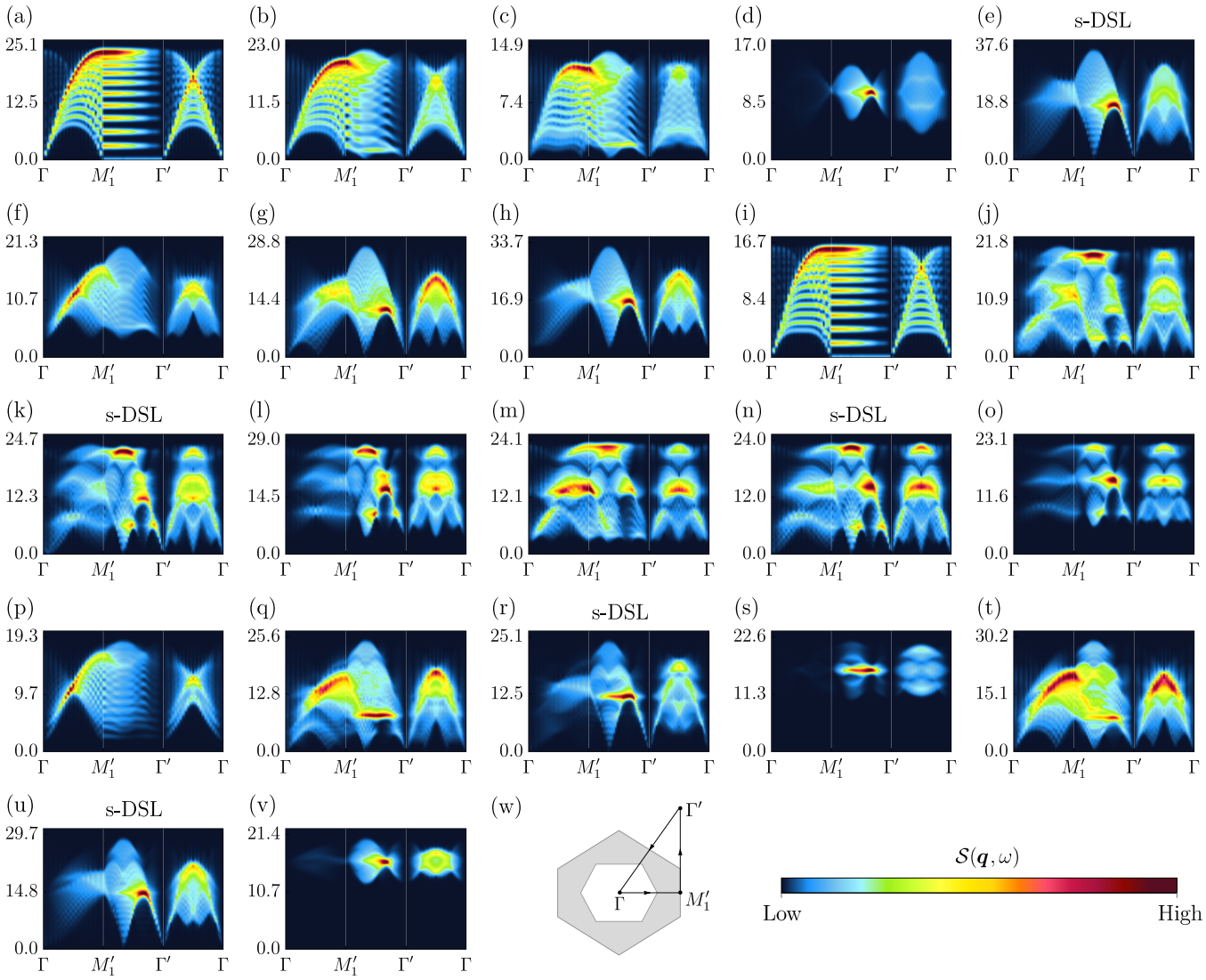


FIG. 10. Dynamical spin structure factors plotted along the momentum-space path $\Gamma \to M_1' \to \Gamma' \to \Gamma$, where the high-symmetry points are defined as $\Gamma = (0,0)$, $M_1' = (4\pi/3, 0)$, and $\Gamma' = (4\pi/3, 2\pi)$. The calculations are performed on a system of size $24 \times 24 \times 2$. The panels correspond to the following *Ansätze*: (a)–(e) U1, (f)–(h) U2, (i)–(l) U3, (m)–(o) U4, (p)–(s) U5, and (t)–(v) U6. The hopping amplitude χ_h is fixed to 1 in all cases. For the U1 *Ansatz*, shown in panels (a)–(e), the remaining mean-field parameters (χ_v, χ_z) are set to (a) $(0, 6)$, yielding a nodal-line spin liquid; (b) $(1, 5)$, corresponding to a Dirac spin liquid; (c) $(1, 1)$, giving a spinon Fermi surface; (d) $(5, 1)$, resulting in a fully gapped spin liquid; and (e) $(9, 4.5)$, which produces a semi-Dirac spin liquid. These phases correspond to the band structures shown in Fig. 4(d). For the U2 *Ansatz* [Fig. 4(e)], panels (f)–(h) show results for (f) $(2, 4)$: a gapped phase; (g) $(4\sqrt{2}, 4)$: the DSL phase; and (h) $(8, 4)$: the second gapped phase. Here, the DSL phase occurs along a critical line separating two gapped regimes. For the U3 *Ansatz* [Fig. 4(f)], panels (i)–(l) correspond to (i) $(0, 4)$: a nodal-line phase; (j) $(4, 4)$: a DSL phase; (k) $(4\sqrt{2}, 4)$: a semi-Dirac spin liquid; and (l) $(8, 4)$: a gapped phase. For the U4 *Ansatz* [Fig. 4(j)], panels (m)–(o) show the DSF for (m) $(4, 4\sqrt{3/2})$: a gapped phase; (n) $(4\sqrt{2}, 4)$: an s-DSL phase; and (o) $(4\sqrt{3}, 4/\sqrt{2})$: another gapped phase. In this case, the s-DSL phase again separates two distinct gapped regions. For the U5 *Ansatz* [Fig. 4(k)], panels (p)–(r) represent (p) $(1, 4)$: a gapped phase; (q) $(4, 4)$: a DSL phase; (r) $(6, 2.83)$: a state with s-DSL phase; and (s) $(8, 1)$: the other gapped phase. Finally, for the U6 *Ansatz* [Fig. 4(l)], panels (t)–(v) correspond to (t) $(4, 5)$: the DSL phase; (u) $(7, 3.64)$: the s-DSL phase; (v) $(8, 1)$: a gapped phase and (w) shows the high-symmetry path along which the structure factors are plotted.

where $\boldsymbol{r}_{ij} = \boldsymbol{r}_i - \boldsymbol{r}_j$ and N denotes the total number of sites. Inserting the Heisenberg time evolution of $\hat{S}_i^z(\tau) = e^{i\hat{H}\tau}\hat{S}_i^z e^{-i\hat{H}\tau}$ and expressing the spin operators in terms of fermionic spinons recasts Eq. (83) into the form

$$\mathcal{S}^{zz}(\boldsymbol{q},\omega) = \int_{-\infty}^{+\infty} \frac{d\tau\, e^{i\omega\tau}}{8\pi N} \sum_{i,j} e^{i\boldsymbol{q}\cdot\boldsymbol{r}_{ij}} \tau^z_{\alpha\alpha}\tau^z_{\beta\beta}$$

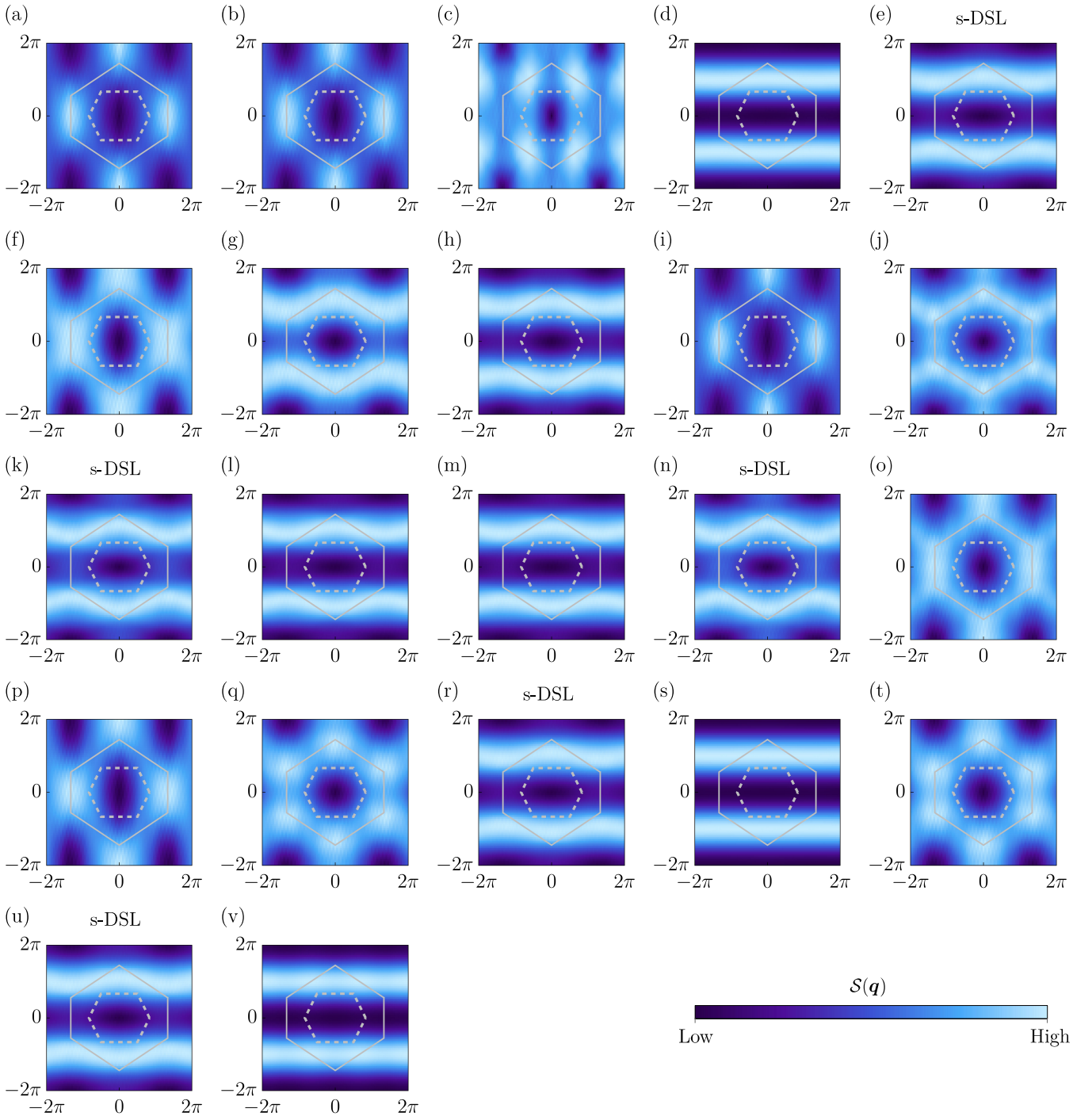


FIG. 11. Equal-time structure factors shown for the same points as Fig. 10. The solid (dashed) hexagon marks the extended (first) Brillouin zones.

$$\times \sum_{\alpha,\beta} \langle e^{i\hat{H}\tau} \hat{f}^{\dagger}_{i,\alpha} \hat{f}_{i,\alpha} e^{-i\hat{H}\tau} \hat{f}^{\dagger}_{j,\beta} \hat{f}_{j,\beta} \rangle. \tag{84}$$

For U(1) *Ansätze*, given the absence of pairing terms, the spin-up and spin-down sectors decouple, allowing us to work in a basis consisting solely of annihilation operators in each spin sector, i.e., $\hat{f}^{\dagger}_{\alpha} = (\hat{f}^{\dagger}_{1,\alpha}, \hat{f}^{\dagger}_{2,\alpha}, \cdots, \hat{f}^{\dagger}_{N,\alpha})$. Consequently, the Hamiltonian takes the form

$$\hat{H} = \sum_{\alpha=\uparrow,\downarrow} \hat{f}^{\dagger}_{\alpha} \hat{\mathcal{H}} \hat{f}_{\alpha}. \tag{85}$$

We now perform a unitary transformation $\hat{f}_{\alpha} = U\hat{c}_{\alpha}$ such that $U^{\dagger}\hat{\mathcal{H}}U = \mathrm{diag}(\epsilon_1, \epsilon_2, \ldots, \epsilon_N)$. Substituting into Eq. (84), we obtain

$$\mathcal{S}^{zz}(\boldsymbol{q},\omega)=\int_{-\infty}^{+\infty}\frac{d\tau\, e^{i\omega\tau}}{8\pi N}\sum_{i,j,\mu,\mu',\nu,\nu'}e^{i\boldsymbol{q}\cdot\boldsymbol{r}_{ij}}\tau^z_{\alpha\alpha}\tau^z_{\beta\beta}\,U^*_{i,\mu}U_{i,\mu'}U^*_{j,\nu}U_{j,\nu'}\sum_{\alpha,\beta}\langle e^{i\hat{H}\tau}\hat{c}^\dagger_{\mu,\alpha}\hat{c}_{\mu',\alpha}e^{-i\hat{H}\tau}\hat{c}^\dagger_{\nu,\beta}\hat{c}_{\nu',\beta}\rangle. \tag{86}$$

The DSF involves contributions from processes in which a fermion is annihilated in an initially occupied state (ν',β) and a fermion is simultaneously created in an unoccupied state (ν,β) at $\tau=0$. This particle-hole excitation persists until time τ, when it is annihilated. This leads to the simplification

$$\langle e^{i\hat{H}\tau}\hat{c}^\dagger_{\mu,\alpha}\hat{c}_{\mu',\alpha}e^{-i\hat{H}\tau}\hat{c}^\dagger_{\nu,\beta}\hat{c}_{\nu',\beta}\rangle=e^{-i(\epsilon_\nu-\epsilon_{\nu'})\tau}\delta_{\nu',\mu}\delta_{\mu',\nu}\delta_{\alpha,\beta}\langle\hat{c}^\dagger_{\mu,\alpha}\hat{c}_{\nu',\beta}\rangle\langle\hat{c}_{\mu',\alpha}\hat{c}^\dagger_{\nu,\beta}\rangle, \tag{87}$$

which, upon substitution into Eq. (86), yields

$$\mathcal{S}^{zz}(\boldsymbol{q},\omega)=\frac{1}{2N}\sum_{i,j,\mu,\nu}e^{i\boldsymbol{q}\cdot\boldsymbol{r}_{ij}}\delta(\omega-\epsilon_\nu+\epsilon_\mu)U^*_{i,\mu}U_{i,\nu}U^*_{j,\nu}U_{j,\mu}n_\mu(1-n_\nu), \tag{88}$$

where the fermionic occupation number is given by $n_i=[\exp(\beta(\epsilon_i-\epsilon_F)+1]^{-1}$, with ϵ_F denoting the Fermi energy.

In the zero-temperature limit, the Fermi distribution becomes a step function, and Eq. (88) simplifies to

$$\mathcal{S}^{zz}(\boldsymbol{q},\omega)=\frac{1}{2N}\sum_{i,j,\mu,\nu}e^{i\boldsymbol{q}\cdot\boldsymbol{r}_{ij}}\delta(\omega-\epsilon_\nu+\epsilon_\mu)U^*_{i,\mu}U_{i,\nu}U^*_{j,\nu}U_{j,\mu}\Theta(\epsilon_F-\epsilon_\mu)\Theta(\epsilon_\nu-\epsilon_F), \tag{89}$$

where $\Theta(x)$ is the Heaviside step function.

Following this calculation, Fig. 10 presents the dynamical spin structure factors (DSFs) along high-symmetry momentum paths for the same representative points as in Fig. 4. All the DSFs exhibit broad continua instead of sharp dispersive features, a hallmark of fractionalized excitations. The distribution of the dominant spectral intensity, however, varies significantly depending on the *Ansatz* and the specific phase under consideration, appearing at different energies and momenta across the various cases. This sensitivity of the DSF profile offers a concrete experimental handle to distinguish between competing quantum spin liquid states and provides predictions for future experiments on, e.g., the candidate trellis lattice compounds discussed in Sec. VII. It is worth mentioning that since our parton framework is strictly SU(2) spin-rotation invariant (as we do not include an antiferromagnetic order parameter), sharp modes can only appear beyond a mean-field treatment once fermion-fermion interactions are included, e.g., within the random phase approximation (RPA) that has recently been successful in accurately obtaining dynamical spin structure factors [131, 132].

We also explicitly calculate the DSF for the six specific points in the mean-field phase diagram shown in Fig. 7. For these points, the self-consistent solutions yield vanishing hopping amplitudes in certain directions, which allows for a transparent interpretation of the $\mathcal{S}^{zz}(\boldsymbol{q},\omega)$ spectra in Fig. 12.

- Phase I: Here, χ_v and χ_h are vanishingly small compared to χ_z, resulting in effectively decoupled one-dimensional zigzag chains. The spectrum is dispersionless along k_y between M' and Γ'. Along k_x (Γ–M'), $\mathcal{S}^{zz}(\boldsymbol{q},\omega)$ exhibits the characteristic particle-hole continuum of a one-dimensional cosinelike band.

- Phase II: In this regime, χ_z and χ_h dominate while χ_v is negligible. The triangular plaquettes carry staggered 0 and π fluxes, producing alternating χ_h hopping amplitudes. The system organizes into decoupled one-dimensional chains with uniform nearest-neighbor and alternating next-nearest-neighbor hoppings. This alternation opens a band gap, yielding a gapped $\mathcal{S}^{zz}(\boldsymbol{q},\omega)$. The spectrum remains dispersionless along k_y.

- Phase III: When χ_z and χ_v are small compared to χ_h, the system reduces to decoupled horizontal chains with cosinelike parton dispersions. In this case, we observe a full particle-hole continuum along k_x and a dispersionless response along k_y.

- Phase IV: This π-flux decoupled ladder phase arises when the hopping amplitudes along the upper and lower horizontal chains acquire opposite signs, leading to a band gap of $\Delta=2\chi_v$. The horizontal chains thus exhibit gapped cosinelike dispersions, producing a $\mathcal{S}^{zz}(\boldsymbol{q},\omega)$ similar to phase III, but shifted by the gap. Additionally, finite dispersionless spectral weight emerges between M' and Γ' along k_y.

- Phase V: In this limit, horizontal and zigzag hoppings are negligible relative to vertical hopping, reducing the system to a lattice of fully decoupled dimers. The bonding-antibonding energy splitting of the dimers is $2\chi_v$, giving rise to a finite $\mathcal{S}^{zz}(\boldsymbol{q},\omega)$ only at $\omega=2\chi_v$.

- Phase VI: With finite χ_z and χ_v, the system forms a two-dimensional honeycomb lattice featuring Dirac points in the band structure. Consequently, $\mathcal{S}^{zz}(\boldsymbol{q},\omega)$ is gapless, with dispersive features along both k_x and k_y.

Additionally, we calculate the equal-time momentum-resolved spin-spin correlation function, also known as the EQSF, which is relevant to elastic neutron scattering. This quantity can be obtained from Eq. (82) by summing the DSF over all frequencies: $\mathcal{S}^{zz}(\boldsymbol{q}) \equiv \sum_\omega \mathcal{S}^{zz}(\boldsymbol{q},\omega)$, leading to the final expression

$$\mathcal{S}^{zz}(\boldsymbol{q}) = \frac{1}{2N}\sum_{i,j,\mu,\nu} e^{i\boldsymbol{q}\cdot\boldsymbol{r}_{ij}} U^*_{i,\mu}U_{i,\nu}U^*_{j,\nu}U_{j,\mu} \times \Theta(\epsilon_F-\epsilon_\mu)\Theta(\epsilon_\nu-\epsilon_F). \tag{90}$$

The resulting EQSFs are shown in Fig. 11, evaluated at the same representative parameter points used for the dispersions in Fig. 4 and the DSF plots in Fig. 10. Once again, we observe a smooth distribution of spectral weight in the Brillouin zone and an absence of sharp Bragg peaks, as expected for quantum paramagnetic states.

B. Keldysh pf-FRG analysis

To complement the mean-field results for the dynamical and equal-time spin structure factors, we employ the recently developed Keldysh extension [85, 133] of the pf-FRG [134]. The core idea of this method is to formulate a renormalization group flow for the frequency-dependent effective interactions and onsite self-energies of the Abrikosov pseudofermions, as defined in Eq. (2), by introducing a cutoff scale Λ that suppresses low-energy dynamics. At large Λ, the system is described by the bare microscopic Hamiltonian, while gradually lowering Λ drives the flow toward the fully interacting regime, which is recovered at $\Lambda = 0$.

By utilizing the Keldysh formalism—originally developed for nonequilibrium systems—in an equilibrium setting at finite temperature T, the method provides direct access to the real-frequency structure of the interaction vertices. This circumvents the need for an ill-conditioned analytical continuation from imaginary (Matsubara) frequencies, as would be required in conventional equilibrium formulations.

From the flowing pf-FRG vertices and self-energies, we compute both the dynamical and equal-time spin structure factors for the full spin-1/2 system. It is important to note that within this formalism, excitations near the Γ point are naturally suppressed, particularly in regimes close to long-range magnetic order [133].

For the numerical calculations, we set the inverse temperature to $\beta = 1/T = 10/J$, where $J = J_z + J_h + J_v$ defines the overall energy scale of the system. Correlations are computed up to a spatial extent of 4 lattice spacings along the $\boldsymbol{T}_1$ direction and 2 along the $\boldsymbol{T}_2$ direction, resulting in a total of 41 symmetry-inequivalent lattice sites. The frequency axis is discretized using a linear-logarithmic mesh comprising 43 non-negative frequencies.

All pf-FRG flows remain smooth down to $\Lambda = 0$, except for the ladder phase, where a kink in the flow at $\Lambda_c = 0.05$ signals the onset of long-range magnetic order. Accordingly, for this case, we present the spin structure factor at Λ_c, while for all other cases the structure factors are shown in the fully renormalized ($\Lambda \to 0$) limit.

The DSFs and EQSFs thus obtained from our analysis are arrayed in Fig. 12 for the six phases identified in the fully symmetric ternary phase diagram, alongside the corresponding mean-field results. In most cases, we find excellent qualitative agreement between the EQSFs derived from our PSG *Ansätze* and those obtained from the beyond-mean-field Keldysh approach.

For the DSFs, however, qualitative differences arise between the mean-field and Keldysh results. These discrepancies can be traced to two principal limitations of the Keldysh pf-FRG [133]: (1) Its inability to resolve spectral gaps when the associated order parameter is not explicitly included in the flow and (2) the absence of downward-dispersing branches toward $q = 0$ in systems with antiferromagnetic order. The first limitation is generic to FRG approaches: If an order parameter is not explicitly incorporated into the flow equations, it cannot acquire a finite value, leading in practice to gapless spectra. Implementing a general order parameter that captures spectral gaps is nontrivial, as it cannot be introduced in a system-independent manner [133]. The second limitation is more severe and stems from the systematic suppression of long-range order within pf-FRG. In this framework, transitions from the initial paramagnetic state to an ordered phase are always accompanied by a diverging susceptibility, which would necessitate a divergence in the vertex function. Since the Keldysh pf-FRG relies on avoiding divergences to fully remove cutoff dependences, one is constrained to remain in the initial paramagnetic regime, preventing the correct reproduction of long-range features. Furthermore, the fermionic decomposition of spin operators introduces additional inaccuracies, as discussed in detail in Ref. 133. Despite these caveats, the Keldysh pf-FRG remains a powerful method for resolving the dominant low-energy excitations around the ground state. This makes it particularly well suited for spin liquid candidates, where long-range order is absent and alternative approaches may fail.

Taking these limitations into account, we find that phases I and III show good agreement in terms of the principal low-energy excitations. Phases II and IV also display the expected qualitative features, aside from the absence of a spectral gap, which follows directly from limitation (1). More significant deviations from PSG-based expectations appear in phases V and VI. A comparison of the dynamical structure factors together with

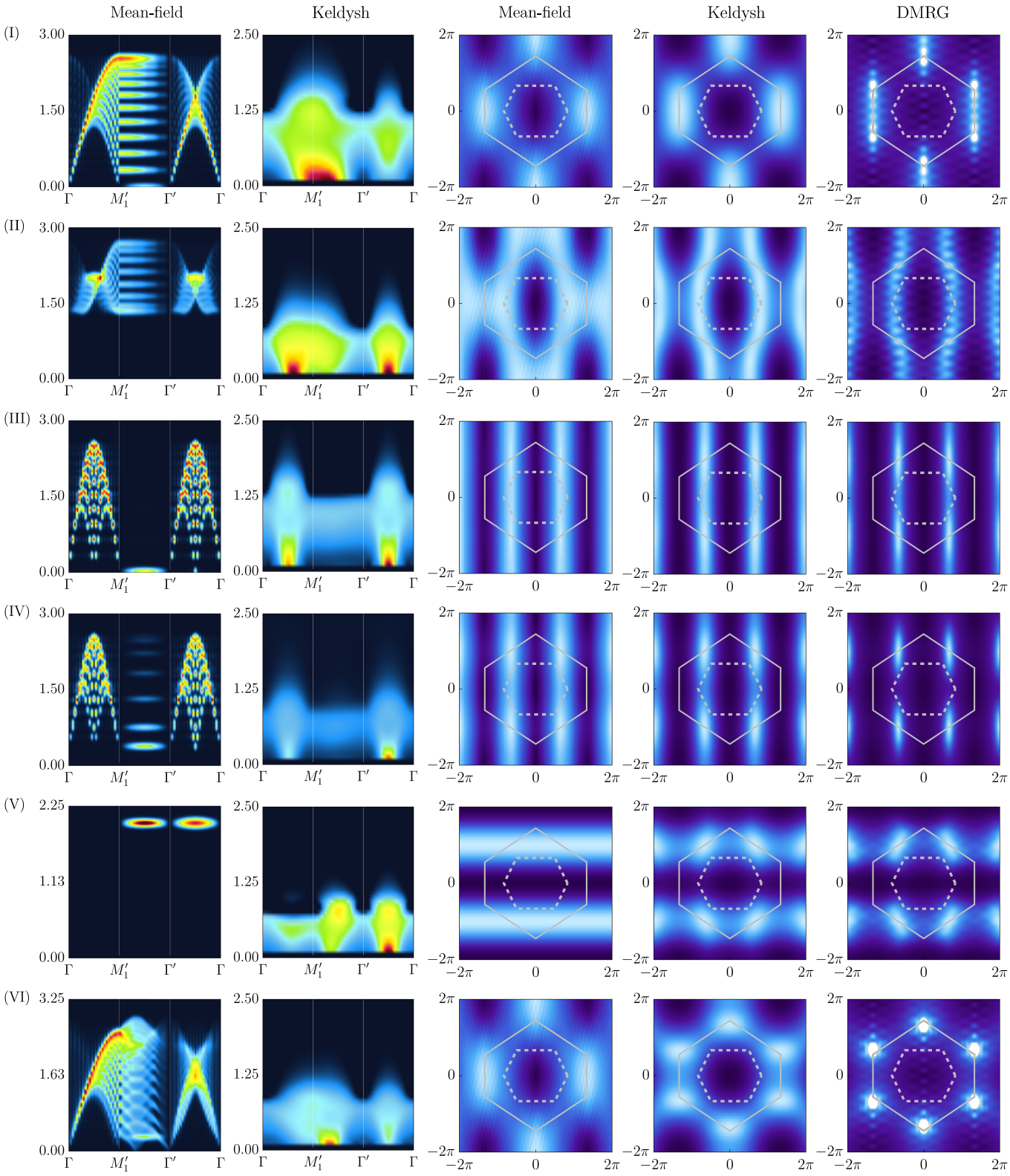


FIG. 12. Equal-time and dynamical structure factors obtained within mean-field theory, the Keldysh pf-FRG formalism, and DMRG for the six phases (I)–(VI) defined in Fig. 7. For the mean-field results, the y-axis of the dynamical structure factors denotes the frequency ω whose scale depends on the χ parameters optimized with respect to (J_z, J_h, J_v); for the Keldysh results, the y axis is labeled by ω/J, where $J = J_z + J_h + J_v$.

the equal-time spin structure factors with mean-field results suggests that (1) either beyond–mean-field corrections could account for these discrepancies, such as by incorporating fermion-fermion interactions, e.g., within an RPA framework [131, 132] or treating gauge fluctuations via Gutzwiller projection, or (2) these could be signatures of incipient magnetic orders that are captured in DMRG and Keldysh pf-FRG.

In summary, while the Keldysh pf-FRG has intrinsic limitations, it remains a valuable tool for characterizing the main low-energy excitations beyond mean-field theory, provided that the above constraints are properly considered.

C. DMRG calculations

Another unbiased approach for the calculation of spin correlation functions is DMRG [135–137]. Unlike Keldysh pf-FRG computations, which operate at small but finite temperatures, DMRG directly accesses the zero-temperature ground-state properties of the system.

Our DMRG calculations are, in practice, based on the variational optimization of a matrix product state (MPS) wave function. Once such an MPS representation of the ground state is obtained for a given set of Hamiltonian parameters, the spin correlation functions can be readily computed. DMRG is particularly powerful for one-dimensional systems, for which it is known to provide extremely accurate results. In our context, this is advantageous for certain phases (e.g., I, III, and IV in the mean-field phase diagram of Fig. 7), which become effectively quasi-one-dimensional due to the reduced couplings along some directions (refer to Table VI).

Here, we simulate the trellis lattice system on a cylindrical geometry with open boundary conditions along $\boldsymbol{T}_1$ and periodic boundary conditions along the $\boldsymbol{T}_2$ direction[2]. A well-known limitation of two-dimensional DMRG is that the number of states required grows exponentially with the system width [137], which restricts accessible system sizes. In this work, we consider a 10×5 system (i.e., with up to 10 sites in the periodic direction), with a maximum MPS bond dimension of 2400. Our sweeping strategy involves starting with many sweeps at relatively small bond dimensions and gradually increasing the bond dimension until convergence is achieved. Convergence is defined as the point where the truncation error falls below 10^{-5}, which is typically satisfied after $\mathcal{O}(10^2)$ sweeps. To facilitate the buildup of long-range correlations, we also add a small noise term to the density matrix during the early sweeps, which is subsequently turned off [138].

[2] Fully periodic boundaries would require a quadratic increase in the number of states needed for the same accuracy, making the computation prohibitively expensive.

The resulting equal-time structure factors, shown in the rightmost column of Fig. 12, display excellent agreement with the Keldysh pf-FRG results across all six phases (I–VI). In particular, the DMRG calculations capture features that lie beyond mean-field theory, which are also visible in the pf-FRG spectra, albeit broadened due to the finite temperatures intrinsic to the latter formalism.

VII. MATERIAL REALIZATIONS

The rich physics of magnetic frustration on the trellis lattice that we have discussed so far can also, in principle, be explored in solid-state materials. To this end, we introduce four compounds—$SrCu_2O_3$, $CaCu_2O_3$, MgV_2O_5, and CaV_2O_5—that are known to realize the trellis lattice geometry. Both Cu^{2+} and V^{4+} ions carry spin-1/2. To avoid confusion, we label the exchange couplings in order of strictly increasing distances between magnetic sites. In the various realizations of the trellis lattice, the three main couplings—namely, the chain (J_h), rung (J_v), and sawtooth (J_z) interactions—are realized through different intersite distances depending on the compound. In Fig. 13, the colors purple, light blue, and blue are used to denote J_h, J_v, and J_z, respectively.

A. Density functional theory

For the four materials, we apply a DFT-based energy-mapping approach that has been successfully used to understand many low-dimensional copper-based quantum magnets [139–141]. Our approach employs all electron electronic structure calculations using the full potential local orbital basis set [142] with a generalized gradient approximation exchange correlation potential [143]. Strong electronic correlations on Cu^{2+} and V^{4+} $3d$ orbitals are treated with a DFT+U correction [144]. This correction has two parameters, the on-site interaction U and the Hund's coupling J_{H}. As the latter is not expected to be strongly material dependent, we fix it to be $J_{\mathrm{H}} = 1\,\mathrm{eV}$ for Cu [145] and $J_{\mathrm{H}} = 0.68\,\mathrm{eV}$ for V [146]. The interaction strength U determines the energy scale of the magnetic interactions and is taken from experimental Curie-Weiss temperatures whenever possible. For the energy mapping, we classify all spin configurations in low-symmetry supercell structures and map large sets of DFT+U total energies to the Heisenberg Hamiltonian written as $\hat{\mathcal{H}} = \sum_{i<j} J_{ij} \hat{\mathbf{S}}_i \cdot \hat{\mathbf{S}}_j$, where every bond is counted only once. Rather than making assumptions about an important subset of exchange couplings, we calculate between 9 and 12 interactions for each of the four materials, and the result flags the important couplings in an unbiased fashion; in most cases, we also gather information about exchange paths coupling the trellis layers, which are important for possible magnetic orders.

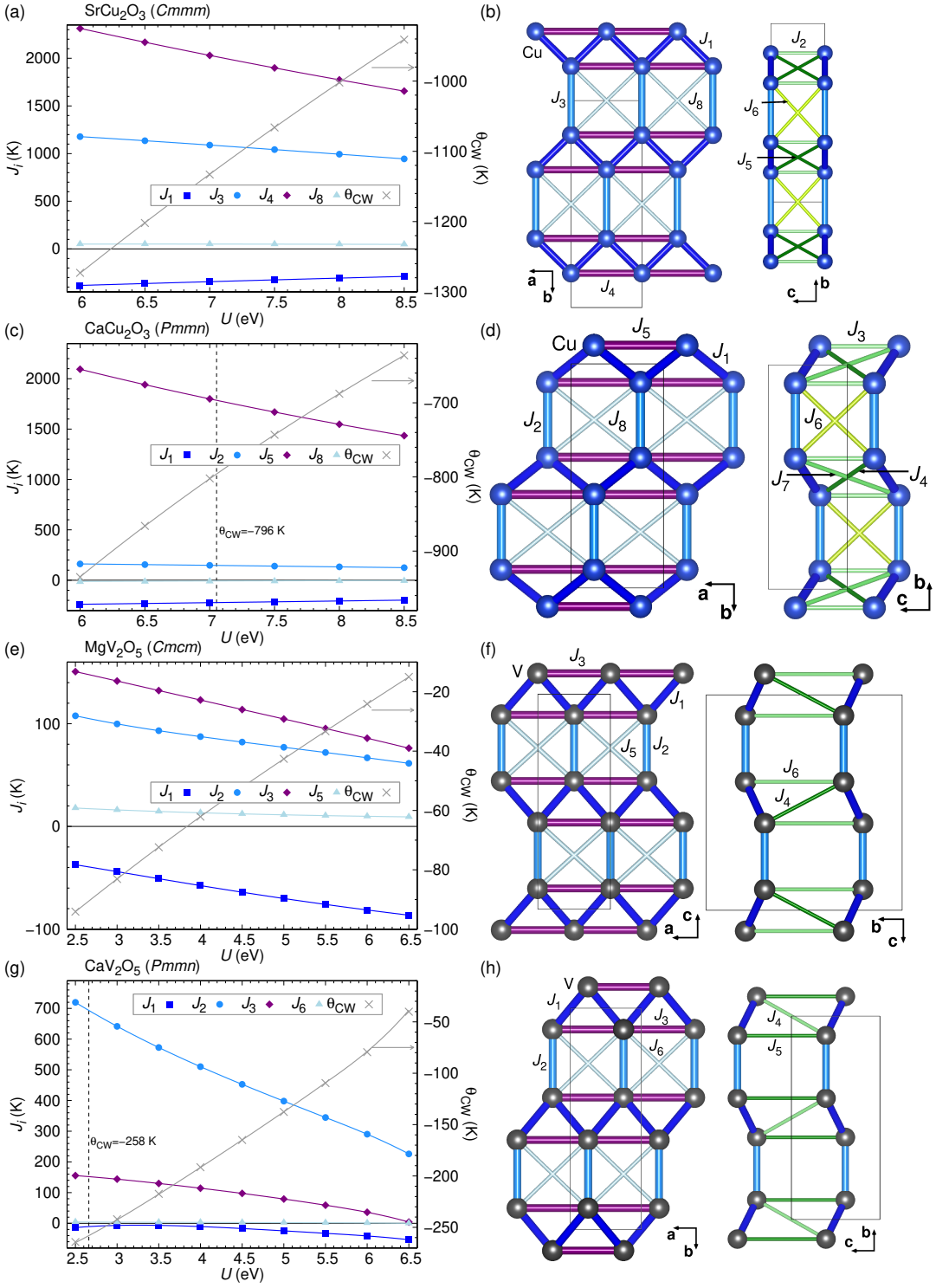


FIG. 13. DFT energy mapping results and Curie-Weiss fits for the trellis lattice compounds (a), (b) $SrCu_2O_3$, (c), (d) $CaCu_2O_3$, (e), (f) MgV_2O_5, and (g), (h) CaV_2O_5.

$SrCu_2O_3$ is a cuprate compound exhibiting a flat trellis lattice [Fig. 13(b)], with couplings identified as $J_h \equiv J_4$, $J_v \equiv J_3$, and $J_z \equiv J_1$. We perform our calculations using the $T = 100\,\mathrm{K}$ structure with $Cmmm$ space group, as determined by single-crystal x-ray diffraction [147]. The DFT energy mapping reveals a system composed of robust two-leg J_h-J_v ladders, with $J_h \approx 2J_v$. The zigzag coupling J_z is found to be weaker and ferromagnetic. Reported spin gap values include $\Delta = 420\,\mathrm{K}$ based on susceptibility data [57], and $\Delta = 680\,\mathrm{K}$ from

Cu NMR [148]. The susceptibility presented in Ref. 57 is challenging to interpret via a traditional Curie-Weiss fit, as χ^{-1} exhibits a negative slope at high temperatures. Using the refined Curie-Weiss fitting procedure from Ref. 149, we obtain $\theta_{\rm CW} = -626\,{\rm K}$; however, this result is unreliable due to the limited temperature range (data only extend to 650 K). Efforts to determine accurate Hamiltonian parameters have employed simplified models, such as the two-leg ladder approximation [150–152]. Among the computed Hamiltonians, the one obtained with $U = 8.5\,{\rm eV}$ appears most consistent with the expectation that J_h should be approximately twice the spin gap, i.e., around 1400 K. The extracted values are $J_h = J_4 = 1656(14)\,{\rm K}$, $J_v = J_3 = 945(16)\,{\rm K}$, and $J_z = J_1 = -289(27)\,{\rm K}$. Besides the three trellis lattice couplings, we obtain the diagonal coupling in the ladder $J_8 = 48(14)\,{\rm K}$ as well as interlayer couplings $J_2 = 41(22)\,{\rm K}$, $J_5 = -9(23)\,{\rm K}$, $J_6 = 14(9)\,{\rm K}$ and $J_7 = -17(13)\,{\rm K}$ that are small compared to the dominant interaction. For the rung-to-chain ratio J_v/J_h, we have $J_v/J_h = 0.57$, which compares well to the value $J_v/J_h = 0.5$ favored by Johnston [152] after weighing various experimental facts. Our result can be compared with an early *ab initio* study [153] that reports $J_h = 1870\,{\rm K}$, $J_v = 1670\,{\rm K}$, $J_1 = -145\,{\rm K}$ and thus a rather large rung-to-chain ratio of $J_v/J_h = 0.89$. On the other hand, our results are in good agreement with local density approximation+U (LDA+U) calculations reported in Ref. 50 yielding $J_h = 1795\,{\rm K}$, $J_v = 809\,{\rm K}$, $J_1 = -200\,{\rm K}$.

$CaCu_2O_3$ exhibits a buckled trellis lattice [Fig. 13(d)]. We use the $T = 10\,{\rm K}$ structure with *Pnma* space group obtained via neutron diffraction [156]. Here, the exchange couplings are given by $J_h \equiv J_5$, $J_v \equiv J_2$, and $J_z \equiv J_1$. Energy mapping shows that the antiferromagnetic chain coupling J_h dominates over the other two. Using the Curie-Weiss fitting method of Ref. 149 to fit the susceptibility from Ref. 156 [see Fig. 13(c)], we find $\theta_{\rm CW} = -796\,{\rm K}$. In contrast, a conventional χ^{-1} fit misleadingly suggests $\theta_{\rm CW} \approx 0$, inconsistent with the estimated spin chain scale $J_h \equiv J_\parallel = 2000(300)\,{\rm K}$ [156]. At this significant antiferromagnetic Curie-Weiss temperature, indicated by the dashed line in Fig. 13(c), the extracted couplings are $J_h = J_5 = 1786(9)\,{\rm K}$, $J_v = J_2 = 130(16)\,{\rm K}$, and $J_z = J_1 = -228(15)\,{\rm K}$. These results are consistent with the previous estimate of $J_\parallel$ within error bars. An inelastic neutron scattering study by Lake *et al.* [154] determined $J_h = 1880\,{\rm K}$, supporting earlier quantum chemistry predictions [157, 158] that J_v is significantly smaller than J_h. To account for the incommensurate magnetic order observed at $T_{\rm N} = 25\,{\rm K}$ [156], interlayer couplings would be important, but in the present study, at $J_3 = -7(9)\,{\rm K}$, $J_4 = -6(17)\,{\rm K}$, and $J_6 = -12(9)\,{\rm K}$, we have not been able to suppress the error bars sufficiently.

MgV_2O_5 is another material that realizes a buckled trellis lattice. Our calculations are based on the $T = 83\,{\rm K}$ powder x-ray diffraction structure with *Cmcm* space group [159]. In this case, the relevant couplings are $J_h \equiv J_3$, $J_v \equiv J_2$, and $J_z \equiv J_1$ [Fig. 13(f)]. DFT energy mapping indicates a two-leg ladder model, with the rung coupling J_v being comparable in strength to the chain coupling J_h, and with the sawtooth coupling J_z being ferromagnetic. The Curie-Weiss temperature has been reported as $\theta_{\rm CW} = -174\,{\rm K}$, although this value is sensitive to the choice of the constant van-Vleck contribution χ_0. Varying χ_0 between 0 and $0.7\times10^{-5}\,{\rm emu/mol}$ yields $\theta_{\rm CW}$ values ranging from $-205\,{\rm K}$ to $-77\,{\rm K}$, with all χ^{-1} fits appearing equally satisfactory. Since onsite Coulomb interaction values much below $U = 2.5\,{\rm eV}$ are difficult to justify for V^{4+}, we consider the $U = 3\,{\rm eV}$ set of couplings: $J_h = J_3 = 147(1)\,{\rm K}$, $J_v = J_2 = 100(1)\,{\rm K}$, and $J_z = J_1 = -44(1)\,{\rm K}$ (corresponding to $\theta_{\rm CW} = -83\,{\rm K}$ and a rung-to-chain ratio $J_v/J_h = 0.68$). Alternatively, for $U = 2.5\,{\rm eV}$, we find $J_h = J_3 = 151(1)\,{\rm K}$, $J_v = J_2 = 108(1)\,{\rm K}$, and $J_z = J_1 = -37(1)\,{\rm K}$, with $\theta_{\rm CW} = -94\,{\rm K}$ and $J_v/J_h = 0.72$. A perturbation-theory estimate of the couplings based on LDA+U within the linear muffin-tin orbital basis [62, 63] reported $J_h = 144\,{\rm K}$, $J_v = 92\,{\rm K}$, $J_z = 60\,{\rm K}$ which is very similar for the ladder but has a different sign for the zigzag coupling.

The fourth compound that we analyze is CaV_2O_5, which also realizes a buckled trellis lattice. We base our calculations on the room-temperature x-ray powder diffraction structure with *Pmmn* space group [160] [Fig. 13(h)]. Here, the relevant couplings are $J_h \equiv J_3$, $J_v \equiv J_2$, and $J_z \equiv J_1$. Fitting the susceptibility data from Ref. 160 using the Curie-Weiss approach of Ref. 149 [Fig. 13(g)], we obtain $\theta_{\rm CW} = -258\,{\rm K}$. This result suggests, similarly to MgV_2O_5, that a relatively small U is appropriate for this compound. The resulting couplings are $J_h = J_3 = 152(3)\,{\rm K}$, $J_v = J_2 = 693(3)\,{\rm K}$, and $J_z = J_1 = -11(3)\,{\rm K}$. This places CaV_2O_5 in the regime of a two-leg ladder with very strong rungs, characterized by $J_v/J_h = 4.5$, consistent with the scenario proposed by Millet *et al.* [159]. A perturbative estimate [62, 63] was reported to be $J_h = 122\,{\rm K}$, $J_v = 602\,{\rm K}$, $J_z = -28\,{\rm K}$ which has a rung-to-chain ratio $J_v/J_h = 4.9$. Various other models have been suggested, usually also in the strong-rung limit [161–163]. A QMC study [51] arrived at a set of interactions $J_h = 135\,{\rm K}$, $J_v = 665\,{\rm K}$, and $J_z = -25\,{\rm K}$ which is quite close to our *ab initio* result. As far as subleading couplings are concerned, the diagonals in the ladder $J_6 = 18(4)\,{\rm K}$ are the most important, and interlayer couplings such as $J_4 = 1(2)\,{\rm K}$ and $J_7 = 4(2)\,{\rm K}$ are below 1% of the dominant interaction. This makes CaV_2O_5 a good approximation of a two-dimensional material.

B. Keldysh pf-FRG

In this section, we employ the Keldysh formalism combined with the DFT-derived couplings to analyze the materials discussed above.

We begin with $CaCu_2O_3$, which—due to its weak in-

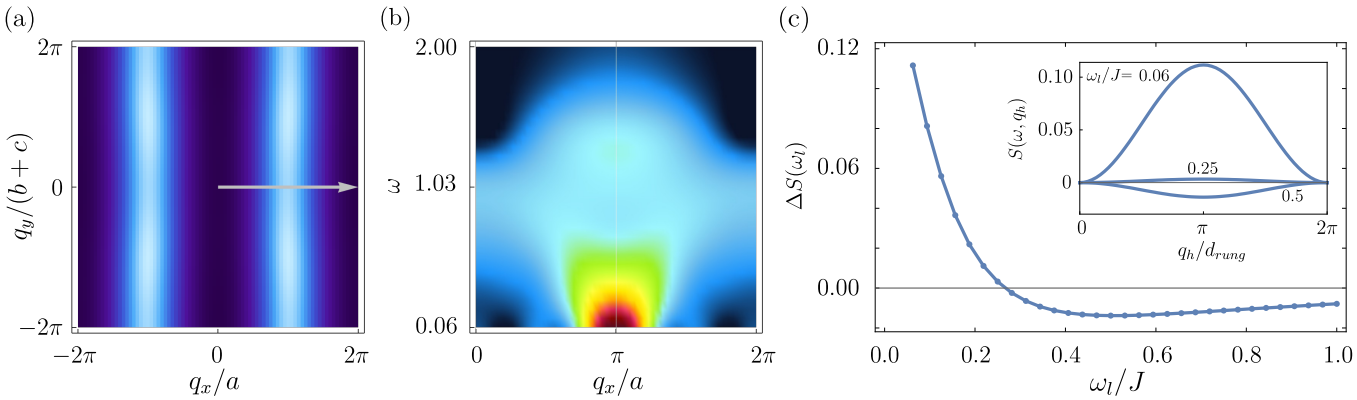


FIG. 14. Keldysh pf-FRG results for $CaCu_2O_3$ obtained for the DFT model Hamiltonian with $J_h = 1786(9)\,\mathrm{K}$, $J_v = 130(16)\,\mathrm{K}$, and $J_z = -228(15)\,\mathrm{K}$. (a) Equal-time spin structure factor with a, b, and c defined in Fig. 1. The nearly uniform behavior in the $q_y \equiv q_h$ (horizontal) direction supports a description in terms of one-dimensional chains along $\boldsymbol{T}_1$. (b) Dynamical spin structure factor along the q_x direction. The fractionalization dome of the spin chain is reproduced up to the branch at $q = 0$, which the Keldysh pf-FRG cannot resolve. (c) Confinement analysis following Ref. 154, calculated using Eq. (91). The modulation is controlled by $1/q_{\mathrm{rung}}$ and rapidly decays to zero. Inset: q-resolved modulation for selected data points. For $\omega_l > 0.27$, the amplitude becomes negative, shifting the q_y modulation to $q_y = 0$, corresponding to an enhancement of the bonding susceptibility channel [154, 155].

terchain couplings $J_2 \equiv J_z$ and $J_3 \equiv J_v$—is close to being a one-dimensional material. This interpretation is supported by the equal-time spin structure factor in Fig. 14, which exhibits nearly uniform behavior along q_y. Consequently, the system effectively realizes one-dimensional chains along $\boldsymbol{T}_1$. The cyclic exchange J_{cycl} [164] cannot be modeled here, as it requires quartic spin interactions that lie beyond the truncation of the FRG. While this four-spin term frustrates the spin chains, its strength in $CaCu_2O_3$ is relatively weak ($J_{\mathrm{cycl}} = 4\,\mathrm{meV}$ [154]) compared to the approximate threshold $J_{\mathrm{cycl}}/J_1 \approx 0.25$ for disrupting binding [164], implying that neglecting it should introduce only minor discrepancies. The dynamical spin structure factor in Fig. 14(b) qualitatively matches the experiment results [154]. The absence of the $q = 0$ branch, a limitation of the Keldysh formalism, is not critical, since this feature is typically unresolved experimentally as well. Up to an expected mismatch in the frequency scale—intrinsic to qualitative methods such as pf-FRG—our description is broadly consistent with the data.

To further test this agreement, we investigate the measured difference between strongly and weakly coupled regimes of the spin chains. Strong coupling produces a modulation along the interchain direction at $1/Q_{\mathrm{rung}}$, which should vanish in the weak-coupling case. Lake *et al.* [154] introduced integrated frequency slices to quantify deviations from the expected $(1 + \cos(Q_{\mathrm{rung}}))\chi_b + (1 - \cos(Q_{\mathrm{rung}}))\chi_{ab}$ form, dominated experimentally by the anti-bonding susceptibility χ_{ab}. Since we cannot disentangle bonding (χ_b) and anti-bonding (χ_{ab}) susceptibilities directly, we interpret the full excitation spectrum instead. Figure 14(c) shows the integrated dynamical susceptibility,

$$\Delta S(\omega_l) = \int_{\omega_l}^{\omega_u} \Big[S(\omega, q_{h,\max}) - S(\omega, q_{h,\min}) \Big]\, \mathrm{d}\omega, \quad (91)$$

with a constant offset removed. Here, we use $q_{h,\max} = (\pi, \pi/d_{\mathrm{rung}})^T$, $q_{h,\min} = (\pi, 0)^T$, and $\omega_u = 5J$ sets the upper frequency cutoff. This choice captures the essential modulation falloff without relying on arbitrary frequency windows. The correlations decay rapidly to zero around $\omega \approx 0.27$, followed by a sign reversal at larger ω/J, indicating that χ_b eventually dominates over χ_{ab}. We interpret this as a remnant of strong chain interactions persisting at higher frequencies, with a small amplitude, potentially enhancing the singlet channel. Nevertheless, the Keldysh pf-FRG is, in principle, capable of capturing triplons that induce χ_b-dominated modulation at low frequencies, extending beyond mean-field analyses.

For the remaining trellis lattice materials, no experimental benchmarks for the dynamical spin structure factor $\mathcal{S}(\boldsymbol{q}, \omega)$ yet exist. We therefore use the Keldysh pf-FRG calculations to make predictions. As discussed in Ref. 133, it should be kept in mind that potential gaps and exponentially suppressed branches at $q = 0$ are not resolved, restricting our predictions to the low-energy sector.

For $SrCu_2O_3$, the strongest couplings are again along the chains, but significant interchain couplings convert the system into coupled two-leg ladders [165]. This is reflected in the equal-time spin structure factor shown in Fig. 15(a), which exhibits two distinct maxima along q_y, consistent with phase IV in Fig. 12. The experimentally known gap of $E_{\mathrm{gap}} \sim 36\,\mathrm{meV}$ [57] lies far below the Keldysh resolution ($E_{\mathrm{gap}}/J \approx 0.015$). Moreover, doping rapidly introduces in-gap states and suppresses singlet-

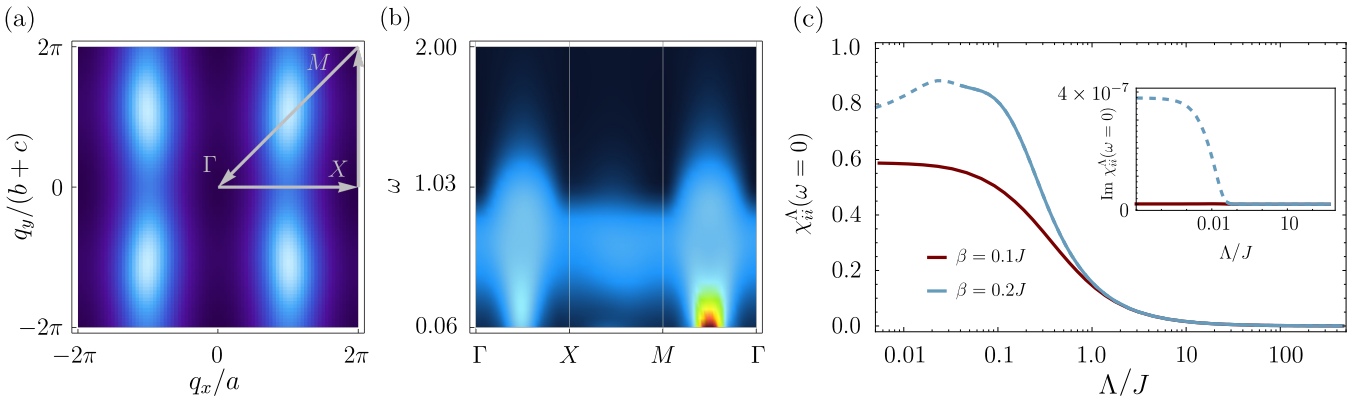


FIG. 15. Keldysh pf-FRG results for $SrCu_2O_3$. (a) Equal-time spin structure factor, with a, b, and c defined in Fig. 1. The result captures the two-legged ladder structure and resembles phase (IV) in Fig. 12. (b) Dynamical spin structure factor, similar to that of the rung ladder. (c) FRG flow of the largest susceptibility component, showing a weak tendency toward magnetic ordering at $\beta = 0.1J$. Both the kink in the flow and the symmetry violation in the imaginary part are small compared to magnetically ordered systems [133].

triplet excitations [166]. We therefore consider the influence of the gap to be small and expect the remaining excitation features to be well captured by the Keldysh pf-FRG. The dynamical spin structure factor Fig. 15(b) closely resembles that of the rung-ladder phase (phase IV in Fig. 7). Its mean-field counterpart corresponds to a quadratic hopping Hamiltonian with π-flux per square plaquette, obtained as a saddle point of the parent U(1) *Ansätze* U2, U3, and U6 in Fig. 3.

It is worth noting that the Keldysh FRG flow does not monotonically continue to vanishing cutoff scales. Instead, as shown in Fig. 15(c), the imaginary part of the susceptibility begins to grow precisely at the position of the kink, which we regard as a signal to terminate the flow, since it should vanish by symmetry. In the pf-FRG framework, such a breakdown serve as an indicator for the onset of magnetic ordering: The FRG cannot flow into a symmetry-broken phase and therefore, the susceptibility diverges at the corresponding phase boundary [134, 167]. This behavior can also occur in the vicinity of symmetry-broken phases—even though a purely two-dimensional model should not order at finite temperature as dictated by the Hohenberg-Mermin-Wagner theorem—which is why we observe these ordering tendencies. Compared to strongly ordered systems, however, the kink seen here is relatively small. This interpretation is supported by the fact that raising the temperature removes the kink entirely, allowing the flow to proceed down to $\Lambda = 0$. Given that the cutoff at the divergence is already small, we use the $\beta = 0.1J$ data above the nonmonotonicity for the equal-time and dynamic spin structure factors, thereby capturing both the incipient ordering tendencies and the underlying spin liquid behavior, which lie beyond the scope of a pure mean-field analysis.

For CaV_2O_5, DFT results identify a two-legged ladder, similar to $SrCu_2O_3$, but with significantly stronger rung couplings ($J_v/J_h = 4.5$). Accordingly, the equal-time spin structure factor [Fig. 16(a)] shows dominant modulation along q_y, consistent with the ladder-dimer phase V in Fig. 7. The dynamical spin structure factor [Fig. 16(b)] shares similarities with that of $SrCu_2O_3$, though the spectral weight is more broadly distributed beyond $\omega = 0$. This broadening stems from the higher breakdown scale $\Lambda \approx 0.08$, about twice that of $SrCu_2O_3$. While there is no direct correspondence between the cutoff and a transition temperature or an energy scale [134], a larger divergence scale qualitatively reflects stronger ordering tendencies. Consequently, this finite cutoff still manifests in the dynamical spin structure factor and leads to an exponential broadening of all $\omega \neq 0$ excitations, unrelated to any intrinsic signatures of spin liquid behavior.

Finally, for MgV_2O_5, we consider two viable DFT configurations, with $U = 3\,\mathrm{eV}$ and $U = 2.5\,\mathrm{eV}$. Both exhibit strong ordering tendencies within pf-FRG that persist even at elevated temperatures. We therefore refrain from presenting the dynamical spin structure factor, as ordering effects and the cutoff-related broadening reduce the applicability of the Keldysh pf-FRG beyond the typical ground-state analysis known from standard Matsubara pf-FRG (and the pseudo-Majorana functional renormalization group). The corresponding equal-time spin structure factors [Figs. 16(c) and 16(d)] appear nearly identical, suggesting similar ground-state properties. However, the flow analysis reveals that the imaginary part of susceptibility, signifying the symmetry-breaking tendency, grows 30 times larger for $U = 2.5\,\mathrm{eV}$ than for $U = 3\,\mathrm{eV}$, indicating a stronger ordering propensity. In both cases, the systems appear magnetically ordered, and further analysis should therefore employ methods such as linear spin-wave theory, which are suited for dynamic correlations on top of magnetically ordered states.

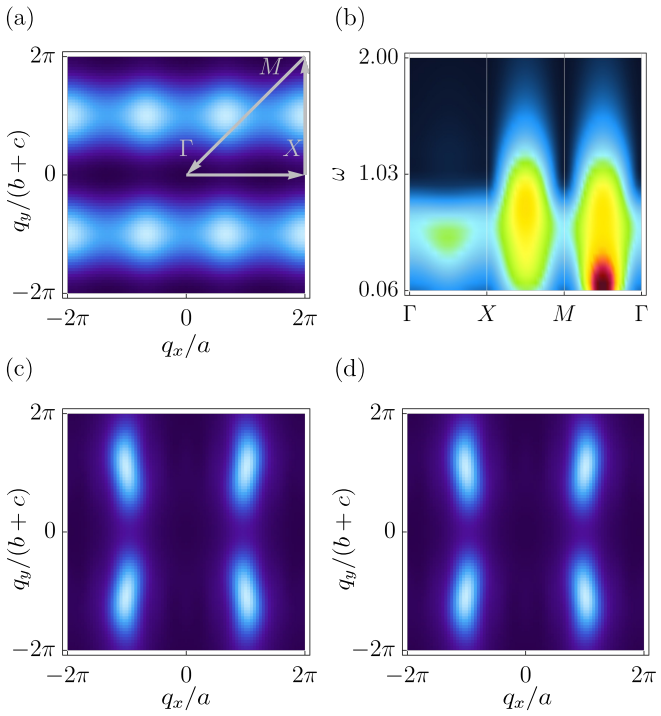


FIG. 16. (a), (b) Keldysh pf-FRG results for CaV_2O_5. (a) Equal-time spin structure factor, with a, b, and c defined in Fig. 1. Strong rung coupling ($J_v/J_h = 4.5$) leads to dominant modulation along q_y, consistent with ladder-dimer phase (V) in Fig. 7. (b) Dynamical spin structure factor, displaying a broader, more featureless spectrum compared to $SrCu_2O_3$, consistent with a higher breakdown scale $\Lambda \approx 0.08$. This broadening reflects the finite cutoff rather than fractionalization. Equal-time spin structure factors for MgV_2O_5 at (c) $U = 3\,\mathrm{eV}$ and (d) $U = 2.5\,\mathrm{eV}$. Both exhibit strong ordering tendencies persisting at finite temperature, precluding dynamical analysis. While the equal-time correlations appear similar, the flow shows much stronger growth of the symmetry-breaking channel at $U = 2.5\,\mathrm{eV}$, indicating enhanced ordering that cannot be resolved in the equal-time limit.

VIII. DISCUSSION AND OUTLOOK

Our work introduces a unique class of QSLs, namely, semi-Dirac spin liquids. The fermionic parton constructions presented here provide a foundation for studying the role of U(1) gauge fluctuations beyond the mean-field approximation. For conventional Dirac spin liquids, the impact of gauge fluctuations has been extensively analyzed, particularly on triangular and kagome lattices, where such states are regarded as excellent variational candidates for the ground state of the spin-1/2 Heisenberg antiferromagnet [4, 5, 113]. In these systems, gauge fluctuations significantly modify spectroscopic signatures [168–171], while preserving the gapless nature of excitations [5, 6, 172–174] and their disordered character without lattice or spin-rotation symmetry breaking [175, 176]. Moreover, singlet and triplet monopoles remain gapless on kagome and triangular lattices, without destabilizing the U(1) Dirac state [177, 178]. By contrast, the influence of gauge fluctuations on U(1) semi-Dirac states with neutral fermions remains unexplored, in constrast to effects of Coulomb interactions on charged fermions [179]. It is therefore important to investigate how Gutzwiller projection modifies the long-distance behavior of spin-spin correlations and the spin structure factor. Possible outcomes include renormalization of the mean-field exponents, as occurs in Dirac spin liquids [113, 180, 181], or more drastic effects such as gap opening [128] or spontaneous symmetry breaking [182]. Since, Gutzwiller projection incorporates spinon interactions in a nonperturbative manner, substantial modifications of low-energy dynamical structure factors are likely. A complementary direction is the symmetry analysis of singlet and triplet monopoles and their condensation patterns into valence-bond crystal and magnetic orders, respectively, which would yield crucial insights into the spectroscopic fingerprints of low-energy monopole excitations [183]. Constructing variational wave functions for monopole excitations and estimating their scaling dimensions would provide further guidance on their stability. Another interesting avenue would be to identify the key ingredients necessary to construct tight-binding models that yield generalized semi-Dirac dispersions, i.e., where the leading term is $\propto |\mathbf{k}|^{2N}$ (with $N > 1$) or host type-II semi-Dirac fermions wherein the spinons disperse with a combination of different momentum components away from the reciprocal lattice vectors [184].

While not stabilized for the nearest-neighbor Heisenberg model on the trellis lattice, the semi-Dirac spin liquid represents a distinct symmetry-allowed quantum spin liquid, motivating the search for microscopic spin models in which it may emerge as a viable variational ground state. At the mean-field level, these states appear only at fine-tuned phase boundaries, and it remains to be seen whether upon inclusion of quantum fluctuations the sDSL is robust against its many potential instabilities such as monopole proliferation and confinement, Higgsing of the U(1) gauge boson to $\mathbb{Z}_2$, or spontaneous symmetry breaking driven by (strong) fermion interactions [96]. In the scenario that the sDSL happens to be stable to these perturbations and is realized as a phase while being the variational ground state over a region of parameter space of the nearest-neighbor antiferromagnetic model, it would be interesting to identify additional interactions that could potentially enhance its region of stability. These include terms such as ring-exchange, XXZ anisotropy, etc., and to this effect, it would be important to map out the corresponding ground state phase diagrams using state-of-the-art many-body methods, including variational Monte Carlo, DMRG, and tensor-network approaches. It is also valuable to systematically determine which lattice and Hamiltonian symmetries are required to host semi-Dirac spectra [185–187], and to examine their feasibility across other wallpaper

groups and in three-dimensional lattices. A particularly intriguing direction is the realization of semi-Dirac QSLs in tight-binding models on two-dimensional hyperbolic lattices [188–191], a setting that remains largely unexplored.

Given the delicate competition between quantum spin liquid and weak magnetic order in the spin-1/2 nearest-neighbor Heisenberg antiferromagnet, it would be instructive to study this interplay using variational Monte Carlo. Jastrow-Slater wave functions have previously provided accurate estimates of order parameters and phase boundaries in frustrated magnets. Should the magnetic order parameter vanish in the thermodynamic limit, the U(1) and $\mathbb{Z}_2$ states classified here would constitute strong candidates for the true ground state. Comparing the variational energies of their Gutzwiller-projected wave functions would then allow one to identify the lowest-energy phase and thereby elucidate the microscopic nature of the ground state. In particular, the quantum melting of classical incommensurate spirals has been argued to give rise to gapped $\mathbb{Z}_2$ QSLs [192, 193], providing a concrete starting point for future investigations.

Finally, we note that recent advances in quantum simulation have enabled the realization of tunable Heisenberg and XXZ models on arbitrary lattice geometries, including the trellis lattice [194, 195]. Such synthetic quantum systems offer yet another pathway to probe the correlated phases discussed in this work, complementing solid-state materials. In particular, these platforms' capability for site-resolved measurements provides direct microscopic access to quantities that are typically inaccessible in bulk experiments [196]. This includes not only local spin correlations but also more refined probes such as the entanglement entropy [197, 198], thereby offering unique insights into the underlying quantum many-body physics.

ACKNOWLEDGMENTS

We thank Subhro Bhattacharjee, Titas Chanda, Andrey Chubukov, Johannes Knolle, Zohar Nussinov, Sri Raghu, and Subir Sachdev for helpful discussions. The work of K.P., R.S., and Y.I. was performed in part at the Aspen Center for Physics, which is supported by a grant from the Simons Foundation (1161654, Troyer). This research was also supported in part by grant NSF PHY-2309135 to the Kavli Institute for Theoretical Physics. S.C. acknowledges the use of the computing resources at HPCE, IIT Madras and support from the Anusandhan National Research Foundation (ANRF), India in the form of a Junior Research Fellowship via the Prime Minister Early Career Research Grant Scheme ANRF/ECRG/2024/001198/PMS. K.P, R.T., and H.O.J. thank IIT Madras for a Visiting Faculty Fellow position under the IoE program that enabled completion of this work. H.O.J. acknowledges support through JSPS KAKENHI Grants No. 24H01668 and No. 25K0846007. The work in Würzburg was supported by the Deutsche Forschungsgemeinschaft (DFG, German Research Foundation) through Project ID 258499086 — SFB 1170 and through the Würzburg-Dresden Cluster of Excellence on Complexity and Topology in Quantum Matter - ct.qmat Project ID 390858490-EXC 2147. K.P. was supported by Hungarian NKFIH OTKA Grant No. K142652. Y.I. acknowledges support from the Abdus Salam International Centre for Theoretical Physics through the Associates Programme, from the Simons Foundation through Grant No. 284558FY19, from IIT Madras through the Institute of Eminence program for establishing QuCenDiEM (Project No. SP22231244CPETWOQCDHOC), and the International Centre for Theoretical Sciences for participation in the Discussion Meeting — Fractionalized Quantum Matter (code: ICTS/DMFQM2025/07). R.S. was supported by the Princeton Quantum Initiative Fellowship. The DMRG calculations presented in this article were implemented using the ITensor library [199] and performed on computational resources managed and supported by Princeton Research Computing, a consortium of groups including the Princeton Institute for Computational Science and Engineering (PICSciE) and the Office of Information Technology's High Performance Computing Center and Visualization Laboratory at Princeton University.

DATA AVAILABILITY STATEMENT

The data generated during the current study are available from the corresponding author upon reasonable request.

Appendix A: Algebraic symmetry relations

The projective realizations $W_{\mathcal{O}}$ of the symmetry elements $\mathcal{O}$ must satisfy the algebraic constraints specified in Eqs. (18)–(29). These constraints are enforced by replacing each occurrence of the identity symmetry element $\mathcal{I}$ on the right-hand sides with an element of the IGG, since the PSG associated with $\mathcal{I}$ coincides with the IGG. Consequently, the conditions on the projective gauge transformations $W_{\mathcal{O}}$ are

$$W_{T_1}(x,y,u)W_{T_2}(x-1,y,u)W_{T_1}^{-1}(x,y-1,u)W_{T_2}^{-1}(x,y,u) \in \mathrm{IGG} \tag{A1}$$

$$W_{T_1}(x,y,u)W_{C_2}^{-1}(-x+1,-y,\bar{u})W_{T_1}(-x+1,-y,\bar{u})W_{C_2}(-x,-y,\bar{u}) \in \mathrm{IGG}, \tag{A2}$$

$$W_{T_2}(x,y,u)W_{C_2}^{-1}(-x,-y+1,\bar{u})W_{T_2}(-x,-y+1,\bar{u})W_{C_2}(-x,-y,\bar{u}) \in \mathrm{IGG}, \tag{A3}$$

$$W_{T_1}^{-1}(x+1,y,u)W_{\sigma_x}^{-1}(x+y+1,-y,\bar{u})W_{T_1}(x+y+1,-y,\bar{u})W_{\sigma_x}(x+y,-y,\bar{u}) \in \mathrm{IGG}, \tag{A4}$$

$$W_{T_1}^{-1}(x+1,y,u)W_{T_2}(x+1,y,u)W_{\sigma_x}^{-1}(x+y,-y+1,\bar{u})W_{T_2}(x+y,-y+1,\bar{u})W_{\sigma_x}(x+y,-y,\bar{u}) \in \mathrm{IGG}, \tag{A5}$$

$$W_{C_2}(x,y,u)W_{\sigma_x}(-x,-y,\bar{u})W_{C_2}(-x-y,y,u)W_{\sigma_x}(x+y,-y,\bar{u}) \in \mathrm{IGG}, \tag{A6}$$

$$W_{C_2}(x,y,u)W_{C_2}(-x,-y,\bar{u}) \in \mathrm{IGG}, \tag{A7}$$

$$W_{\sigma_x}(x,y,u)W_{\sigma_x}(x+y,-y,\bar{u}) \in \mathrm{IGG}, \tag{A8}$$

$$\begin{aligned} &W_{T_1}^{-1}(x+1,y,u)W_{T_2}(x+1,y,u)W_{\sigma_x}(x+1,y-1,u)W_{T_1}(x+y,-y+1,\bar{u}) \\ &\times W_{\sigma_x}^{-1}(x,y-1,u)W_{T_2}^{-1}(x,y,u) \in \mathrm{IGG}, \end{aligned} \tag{A9}$$

$$\begin{aligned} &W_{C_2}(x,y,u)W_{T_1}(-x,-y,\bar{u})W_{T_2}^{-1}(-x-1,-y+1,\bar{u})W_{\sigma_x}(-x-1,-y+1,\bar{u}) \\ &\times W_{C_2}(-x-y,y-1,u)W_{T_2}(x+y,-y+1,\bar{u})W_{\sigma_x}(x+y,-y,\bar{u}) \in \mathrm{IGG}, \end{aligned} \tag{A10}$$

$$W_{\mathcal{T}}(x,y,u)W_{\mathcal{T}}(x,y,u) \in \mathrm{IGG}, \tag{A11}$$

$$W_{\mathcal{T}}(x,y,u)W_{T_1}(x,y,u)W_{\mathcal{T}}^{-1}(x-1,y,u)W_{T_1}^{-1}(x,y,u) \in \mathrm{IGG}, \tag{A12}$$

$$W_{\mathcal{T}}(x,y,u)W_{T_2}(x,y,u)W_{\mathcal{T}}^{-1}(x,y-1,u)W_{T_2}^{-1}(x,y,u) \in \mathrm{IGG}, \tag{A13}$$

$$W_{\mathcal{T}}(x,y,u)W_{C_2}(x,y,u)W_{\mathcal{T}}^{-1}(-x,-y,\bar{u})W_{C_2}^{-1}(x,y,u) \in \mathrm{IGG}, \tag{A14}$$

$$W_{\mathcal{T}}(x,y,u)W_{\sigma_x}(x,y,u)W_{\mathcal{T}}^{-1}(x+y,-y,\bar{u})W_{\sigma_x}^{-1}(x,y,u) \in \mathrm{IGG}. \tag{A15}$$

In the following sections, we explicitly demonstrate how the above equations are applied to determine the algebraic PSGs corresponding to different IGGs, namely U(1) and $\mathbb{Z}_2$. Before proceeding, we clarify the notation employed in the subsequent analysis. For the U(1) gauge group, the IGG elements are parametrized as $\exp(i\theta\tau^z)$ with $\theta \in [0, 2\pi)$. For the $\mathbb{Z}_2$ gauge group, the IGG elements are given by $\eta \in \{+1, -1\}$. In addition, any parameter labeled by "$n_{\ldots}$" is restricted to take values in $\{0, 1\}$.

Appendix B: U(1) projective symmetry groups

In this section, we derive the algebraic solutions of the PSG with IGG U(1). Any *Ansatz* with this IGG can be expressed solely in terms of hopping mean-field parameters,

$$u_{ij} = i\,\chi_{ij}^0\tau^0 + \chi_{ij}^3\tau^z, \tag{B1}$$

which corresponds to the canonical gauge where the U(1) IGG is explicit. In this gauge, elements of the IGG are global U(1) matrices of the form

$$W = \{\exp\{i\,\theta\,\tau^z\} \mid 0 \le \theta < 2\pi\}. \tag{B2}$$

The gauge transformations preserving this canonical form can be written as

$$W_{\mathcal{O}}(r,u) = \mathcal{F}_z(\phi_{\mathcal{O}}(r,u))(i\,\tau^x)^{w_{\mathcal{O}}}, \tag{B3}$$

where $\mathcal{F}_z(\xi) \equiv \exp(i\xi\,\tau^z)$ and $w_{\mathcal{O}} \in \{0, 1\}$ for the symmetry operations $\mathcal{O} \in \{T_1, T_2, C_2, \sigma_x, \mathcal{T}\}$. The reason behind including the factor $(i\,\tau^x)^{w_{\mathcal{O}}}$ on the right-hand side can be understood from the SU(2) flux operator $\mathcal{P}_{\mathcal{C}_i}(\varphi_i) = \mathcal{F}_z(\varphi_i)$, which transforms under projective operations as follows:

$$\begin{aligned} \mathcal{P}_{\mathcal{C}_i}(\varphi_i) &= W_{\mathcal{O}(i)}^{\dagger}\mathcal{P}_{\mathcal{C}_{\mathcal{O}(i)}}(\varphi_{\mathcal{O}(i)})W_{\mathcal{O}(i)} \\ &= (\tau_x)^{w_{\mathcal{O}}}\mathcal{P}_{\mathcal{C}_{\mathcal{O}(i)}}(\varphi_{\mathcal{O}(i)})(\tau_x)^{w_{\mathcal{O}}} \\ &= \mathcal{P}_{\mathcal{C}_{\mathcal{O}(i)}}((-)^{w_{\mathcal{O}}}\varphi_{\mathcal{O}(i)}) \end{aligned} \tag{B4}$$

Notice, that for $w_{\mathcal{O}} = 0$ ($w_{\mathcal{O}} = 1$), the flux $\varphi_{\mathcal{O}(i)} = \varphi_i$ ($\varphi_{\mathcal{O}(i)} = -\varphi_i$). Thus, if we do not consider the $w_{\mathcal{O}} = 1$ case, we would not be able to include those *Ansätze* for which the flux operators connected by the symmetry operation $\mathcal{O}$ have antiparallel orientations.

Specifically, for translations $\mathcal{O} \in \{T_1, T_2\}$, Eq. (B3) gives

$$W_{T_1}(x,y,u) = \mathcal{F}_z(\phi_{T_1}(x,y,u))(i\tau^x)^{w_{T_1}},$$
$$W_{T_2}(x,y,u) = \mathcal{F}_z(\phi_{T_2}(x,y,u))(i\tau^x)^{w_{T_2}}. \tag{B5}$$

Loop operators connected by translations T_i differ by a factor $(-1)^{w_{T_i}}$ in order to maintain translation invariance. Consequently, there are four possible choices for (w_{T_1}, w_{T_2}):

$$w_{T_1} = 0, \quad w_{T_2} = 0, \tag{B6}$$
$$w_{T_1} = 0, \quad w_{T_2} = 1, \tag{B7}$$
$$w_{T_1} = 1, \quad w_{T_2} = 0, \tag{B8}$$
$$w_{T_1} = 1, \quad w_{T_2} = 1. \tag{B9}$$

However, the cases in Eqs. (B8) and (B9) fail to satisfy condition (22), and are therefore excluded. Thus, we restrict our attention to cases (B6) and (B7), which we analyze in the subsequent sections.

1. U(1) class with $w_{T_1} = w_{T_2} = 0$

a. *Lattice symmetries*

Due to the SU(2) gauge redundancy, under a local gauge transformation $W(r,u)$, the projective symmetry operator $W_{\mathcal{O}}(r,u)$ transforms as

$$W_{\mathcal{O}}(r,u) \;\to\; W^\dagger(r,u)\, W_{\mathcal{O}}\, W[\mathcal{O}^{-1}(r,u)]. \tag{B10}$$

This transformation law allows significant simplification of the PSG solutions. To wit, by choosing $W(x,y,u) = \mathcal{F}_z(\phi(x,y,u))$, we obtain

$$W_{T_2}(x,y,u) = W_{T_1}(x,0,u) = \tau^0. \tag{B11}$$

Imposing the translation symmetry condition (A1), we find the translational PSGs

$$W_{T_1}(x,y,u) = \mathcal{F}_z(y\,\theta), \quad W_{T_2}(x,y,u) = \tau^0. \tag{B12}$$

Next, we analyze the point-group symmetries. For C_2, the PSG takes the form

$$W_{C_2}(x,y,u) = \mathcal{F}_z(\phi_{C_2}(x,y,u))(i\tau^x)^{w_{C_2}}. \tag{B13}$$

Defining $\Delta_i \phi(x,y,u) = \phi(x,y,u) - \phi(x-1,y,u)$, and using Eq. (B12) in Eqs. (A2) and (A3), we obtain

$$\Delta_1 \phi_{C_2}(x,y,u) = -(-1)^{w_{C_2}} \theta_{C_2 T_1} + y\theta[1-(-1)^{w_{C_2}}],$$
$$\Delta_2 \phi_{C_2}(x,y,u) = -(-1)^{w_{C_2}} \theta_{C_2 T_2}. \tag{B14}$$

These must further satisfy the consistency condition

$$\Delta_i \phi_{C_2}(x,y,u) + \Delta_{i+1}\phi_{C_2}(x-1,y,u)$$
$$= \Delta_{i+1}\phi_{C_2}(x,y,u) + \Delta_i \phi_{C_2}(x,y-1,u). \tag{B15}$$

For $i = 1$, inserting Eq. (B14) into Eq. (B15) yields the constraint

$$\left[1-(-1)^{w_{C_2}}\right]\theta = 0, \quad \begin{cases} \theta \in [0,2\pi) & \text{if } w_{C_2} = 0, \\ \theta = 0, \pi & \text{if } w_{C_2} = 1. \end{cases} \tag{B16}$$

Substituting back into Eq. (B14), we find that the general solution is

$$\phi_{C_2}(x,y,u) = -(-1)^{w_{C_2}}(x\theta_{C_2T_1} + y\theta_{C_2T_2}) + \rho_{C_2,u}, \tag{B17}$$

where $\rho_{C_2,u} \equiv \phi_{C_2}(0,0,u)$.

We now consider the PSG associated with σ_x. Using Eqs. (A4) and (A5) together with Eq. (B12), we obtain

$$\Delta_1 \phi_{\sigma_x}(x,y,u) = -(-1)^{w_{\sigma_x}} \theta_{\sigma_x T_1} + y\theta\big(1+(-1)^{w_{\sigma_x}}\big),$$
$$\Delta_2 \phi_{\sigma_x}(x,y,u) = -(-1)^{w_{\sigma_x}} \theta_{\sigma_x T_2} + (-1)^{w_{\sigma_x}}(y-1)\theta\,, \tag{B18}$$

which must satisfy the consistency relation analogous to Eq. (B15),

$$\Delta_i \phi_{\sigma_x}(x,y,u) + \Delta_{i+1}\phi_{\sigma_x}(x-1,y,u)$$
$$= \Delta_{i+1}\phi_{\sigma_x}(x,y,u) + \Delta_i \phi_{\sigma_x}(x,y-1,u)\,. \tag{B19}$$

For $i = 1, 2$ in Eq. (B19), substituting Eq. (B18) imposes the following constraints:

$$\left[1+(-1)^{w_{\sigma_x}}\right]\theta = 0, \quad \begin{cases} \theta = 0, \pi & \text{if } w_{\sigma_x} = 0, \\ \theta \in [0,2\pi) & \text{if } w_{\sigma_x} = 1\,. \end{cases} \tag{B20}$$

Combining these constraints with Eq. (B18), the general solution for $\phi_{\sigma_x}(x,y,u)$ is

$$\phi_{\sigma_x}(x,y,u) = -(-1)^{w_{\sigma_x}}\left[x\theta_{\sigma_x T_1} + y\theta_{\sigma_x T_2}\right]$$
$$+ (-1)^{w_{\sigma_x}}\frac{1}{2}y(y-1)\theta + \rho_{\sigma_x,u}\,, \tag{B21}$$

where $\rho_{\sigma_x,u} = \phi_{\sigma_x}(0,0,u)$. To summarize, the constraints obtained from Eqs. (B16) and (B20) are compiled in Table VII.

Continuing with our derivation, substituting Eq. (B17) into Eq. (A7) yields the conditions

$$\rho_{C_2,u} + (-1)^{w_{C_2}}\rho_{C_2,\bar{u}} = \theta_{C_2}$$
$$w_{C_2} = 1 : \theta_{C_2 T_i} = 0, \pi\,. \tag{B22}$$

Case	w_{C_2} (rotations)	w_{σ_x} (reflections)	Constraints on θ
(i)	0	0	$0, \pi$
(ii)	1	0	$0, \pi$
(iii)	0	1	$[0, 2\pi)$
(iv)	1	1	$0, \pi$

TABLE VII. Allowed values of θ for different combinations of (w_{C_2}, w_{σ_x}).

Similarly, substituting the solution (B21) into Eq. (A8) leads to

$$w_{\sigma_x} = 0 : \theta_{\sigma_x T_1} = \theta, \quad \rho_{\sigma_x,u} + \rho_{\sigma_x,\bar{u}} = \theta_{\sigma_x}, \tag{B23}$$

$$w_{\sigma_x} = 1 : \theta_{\sigma_x T_1} = 2\theta_{\sigma_x T_2} + \theta, \quad \rho_{\sigma_x,u} - \rho_{\sigma_x,\bar{u}} = \theta_{\sigma_x}\,. \tag{B24}$$

Furthermore, one can use Eq. (A9) to obtain

$$\rho_{\sigma_x,u} - \rho_{\sigma_x,u} = \theta_1 + (-1)^{w_{\sigma_x}}[\theta_{\sigma_x T_1} - \theta]\,, \tag{B25}$$

while Eq. (A10) leads to the following constraints depending on the different choices of (w_{C_2}, w_{σ_x}):

(i) $w_{C_2} = 0, w_{\sigma_x} = 0$:

$$2\theta_{C_2T_2} + \theta_{\sigma_x T_1} = 2\theta_{\sigma_x T_2} + \theta_{C_2T_1}, \tag{B26}$$

$$\rho_{C_2,u} + \rho_{\sigma_x,\bar{u}} + \rho_{C_2,u} + \rho_{\sigma_x,\bar{u}} = \theta_2 - \frac{\theta_{\sigma_x T_1}}{2}.$$

(ii) $w_{C_2} = 1, w_{\sigma_x} = 0$:

$$\theta_{C_2T_1} = \theta_{\sigma_x T_1}, \tag{B27}$$

$$\rho_{C_2,u} - \rho_{\sigma_x,\bar{u}} - \rho_{C_2,u} + \rho_{\sigma_x,\bar{u}} = \theta_2 - \theta_{\sigma_x T_2} - \theta_{C_2T_2}.$$

(iii) $w_{C_2} = 0, w_{\sigma_x} = 1$:

$$\theta_{C_2T_1} = -\theta_{\sigma_x T_1}, \tag{B28}$$

$$\rho_{C_2,u} + \rho_{\sigma_x,\bar{u}} - \rho_{C_2,u} - \rho_{\sigma_x,\bar{u}} = \theta_2 - \theta_{\sigma_x T_2} - \theta_{C_2T_2}.$$

(iv) $w_{C_2} = 1, w_{\sigma_x} = 1$:

$$\theta_{\sigma_x T_1} + \theta_{C_2T_1} = 2(\theta_{\sigma_x T_2} + \theta_{C_2T_2}), \tag{B29}$$

$$\rho_{C_2,u} - \rho_{\sigma_x,\bar{u}} + \rho_{C_2,u} - \rho_{\sigma_x,\bar{u}} = \theta_2 - \frac{\theta_{\sigma_x T_1}}{2}.$$

Finally, we are left with the constraint (A6), which yields the following conditions:

(i) $w_{C_2} = 0, w_{\sigma_x} = 0$:

$$2\theta_{\sigma_x T_2} + \theta_{C_2T_1} = 2\theta_{C_2T_2} + \theta_{\sigma_x T_1},$$

$$\rho_{C_2,u} + \rho_{\sigma_x,\bar{u}} + \rho_{C_2,u} + \rho_{\sigma_x,\bar{u}} = \theta_{C_2\sigma_x}. \tag{B30}$$

(ii) $w_{C_2} = 1, w_{\sigma_x} = 0$:

$$\theta_{C_2T_1} = \theta_{\sigma_x T_1},$$

$$\rho_{C_2,u} - \rho_{\sigma_x,\bar{u}} - \rho_{C_2,u} + \rho_{\sigma_x,\bar{u}} = \theta_{C_2\sigma_x}. \tag{B31}$$

(iii) $w_{C_2} = 0, w_{\sigma_x} = 1$:

$$\theta_{C_2T_1} = -\theta_{\sigma_x T_1},$$

$$\rho_{C_2,u} + \rho_{\sigma_x,\bar{u}} - \rho_{C_2,u} - \rho_{\sigma_x,\bar{u}} = \theta_{C_2\sigma_x}. \tag{B32}$$

(iv) $w_{C_2} = 1, w_{\sigma_x} = 1$:

$$2(\theta_{C_2T_2} + \theta_{\sigma_x T_2}) = \theta_{\sigma_x T_1} + \theta_{C_2T_1},$$

$$\rho_{C_2,u} - \rho_{\sigma_x,\bar{u}} + \rho_{C_2,u} - \rho_{\sigma_x,\bar{u}} = \theta_{C_2\sigma_x}. \tag{B33}$$

It is worth emphasizing that all the abovementioned U(1) phases may not be gauge independent. Some of them can be fixed using a local gauge transformation of the form

$$W(x, y, u) = \mathcal{F}_z(x\theta_x + y\theta_y). \tag{B34}$$

This transformation does not alter the structure of the translational gauges, except for introducing global phases. These global phases do not affect the *Ansatz* and are therefore irrelevant. The gauge transformations for C_2 and σ_x are now given by

$$\tilde{\phi}_{C_2} = x[-\theta_x - (-1)^{w_{C_2}}\theta_{C_2T_1} - (-1)^{w_{C_2}}\theta_x] + y[-\theta_y - (-1)^{w_{C_2}}\theta_{C_2T_2} - (-1)^{w_{C_2}}\theta_y] + \rho_{C_2,u} \tag{B35}$$

$$\tilde{\phi}_{\sigma_x} = x[-\theta_x - (-1)^{w_{\sigma_x}}\theta_{\sigma_x T_1} + (-1)^{w_{\sigma_x}}\theta_x] + y[-\theta_y - (-1)^{w_{\sigma_x}}\theta_{\sigma_x T_2} + (-1)^{w_{\sigma_x}}\theta_x - (-1)^{w_{\sigma_x}}\theta_y + \frac{1}{2}(-1)^{w_{\sigma_x}}(y-1)\theta] + \rho_{\sigma_x,u}\,. \tag{B36}$$

In the following, we provide the details of the gauge fixing for the four distinct cases of (w_{C_2}, w_{σ_x}) using the gauge-transformed solutions obtained above.

(i) $w_{C_2} = 0$, $w_{\sigma_x} = 0$:
Choosing $2\theta_x = -\theta_{C_2T_1}$ and $2\theta_y = -\theta_{C_2T_2}$ in Eq. (B23) yields

$$\tilde{\phi}_{C_2}(x, y, u) = \rho_{C_2,u}, \tag{B37}$$

$$\tilde{\phi}_{\sigma_x}(x, y, u) = -x\theta_{\sigma_x T_1} - y\theta_{\sigma_x T_2} + \tfrac{1}{2}y(y-1)\theta + \rho_{\sigma_x,u}\,. \tag{B38}$$

(ii) $w_{C_2}=1$, $w_{\sigma_x}=0$:
Here, selecting $\theta_x-2\theta_y=\theta_{\sigma_x T_2}$ sets $\theta_{\sigma_x T_2}=0$. From Eqs. (B22), (B23), and (B27) we obtain $\theta_{C_2T_1}=\theta_{\sigma_x T_1}=\theta=n\pi$ and $\theta_{C_2T_2}=n_{C_2T_2}\pi$. Thus,

$$\tilde{\phi}_{C_2}(x,y,u)=x\theta_{C_2T_1}+y\theta_{C_2T_2}+\rho_{C_2,u}, \tag{B39}$$
$$\tilde{\phi}_{\sigma_x}(x,y,u)=-x\theta_{\sigma_x T_1}+\tfrac{1}{2}y(y-1)\theta+\rho_{\sigma_x,u}\,. \tag{B40}$$

(iii) $w_{C_2}=0$, $w_{\sigma_x}=1$:
Upon choosing $2\theta_x=-\theta_{C_2T_1}$ and $2\theta_y=-\theta_{C_2T_2}$, and using (B24) and Eqs. (B28) , we find

$$\tilde{\phi}_{C_2}(x,y,u)=\rho_{C_2,u}, \tag{B41}$$
$$\tilde{\phi}_{\sigma_x}(x,y,u)=y\theta_{\sigma_x T_2}-\tfrac{1}{2}y(y-1)\theta+\rho_{\sigma_x,u}\,. \tag{B42}$$

(iv) $w_{C_2}=1$, $w_{\sigma_x}=1$:
From Eqs. (B22), (B24), and (B29), we have $\theta_{C_2T_i}=n_{C_2T_i}\pi$, $\theta_{\sigma_x T_1}=2\theta_{\sigma_x T_2}+\theta$, and $\theta_{\sigma_x T_1}+\theta_{C_2T_1}=2(\theta_{\sigma_x T_2}+\theta_{C_2T_2})$. The choice $\theta_x=\theta_{\sigma_x T_2}$ gives

$$\tilde{\phi}_{C_2}(x,y,u)=\theta_{C_2T_1}x+\theta_{C_2T_2}y+\rho_{C_2,u}, \tag{B43}$$
$$\tilde{\phi}_{\sigma_x}(x,y,u)=\theta_{C_2T_1}x-\tfrac{1}{2}y(y-1)\theta+\rho_{\sigma_x,u}\,. \tag{B44}$$

To fix the parameters $\rho_{\dots}$ for all relevant symmetry operations, i.e., σ_x and C_2, we apply a gauge transformation $W(r,u)=\mathcal{F}_z(\phi_u)$ that depends only on the sublattice index u. This yields

$$\tilde{\rho}_{C_2,u}=-\phi_u+\rho_{C_2,u}+(-1)^{w_{C_2}}\phi_{\bar{u}}, \tag{B45}$$
$$\tilde{\rho}_{\sigma_x,u}=-\phi_u+\rho_{\sigma_x,u}+(-1)^{w_{\sigma_x}}\phi_{\bar{u}}\,. \tag{B46}$$

From the cyclic relations (A7) and (A8), we obtain

$$\rho_{C_2,u}+(-1)^{w_{C_2}}\rho_{C_2,\bar{u}}=\theta_{C_2}, \tag{B47}$$
$$\rho_{\sigma_x,u}+(-1)^{w_{\sigma_x}}\rho_{\sigma_x,\bar{u}}=\theta_{\sigma_x}. \tag{B48}$$

Using Eq. (A6), we also find

$$\rho_{C_2,u}+(-1)^{w_{C_2}}\rho_{\sigma_x,\bar{u}} \tag{B49}$$
$$+(-1)^{w_{C_2}+w_{\sigma_x}}\rho_{C_2,u}+(-1)^{w_{\sigma_x}}\rho_{\sigma_x,\bar{u}}=\theta_{C_2\sigma_x}.$$

These conditions allow us to fix the ρ parameters for the four cases of (w_{C_2},w_{σ_x}):

(i) $w_{C_2}=0$, $w_{\sigma_x}=0$:
Choosing $\phi_2=\phi_1-\rho_{C_2,1}+\theta_{C_2}/2$ and combining with Eq. (B47) yields $\tilde{\rho}_{C_2,u}=\theta_{C_2}/2$. Using the IGG freedom to eliminate any global phase, we fix $\rho_{C_2,u}=0$. From Eq. (B49), we find $2\rho_{\sigma_x,u}=\theta_{C_2\sigma_x}$, which after fixing a global phase gives $\rho_{\sigma_x,u}=\{0,n_{\sigma_x}\pi\}$.

(ii) $w_{C_2}=0$, $w_{\sigma_x}=1$:
As in the previous case, we can set $\tilde{\rho}_{C_2,u}=0$. Equation (B48) then gives $\rho_{\sigma_x,2}=\rho_{\sigma_x,1}+n_{\sigma_x}\pi$. Using the IGG freedom to set $\rho_{\sigma_x,1}=0$, we obtain $\rho_{\sigma_x,u}=\{0,n_{\sigma_x}\pi\}$.

(iii) $w_{C_2}=1$, $w_{\sigma_x}=0$:
Choosing $\phi_1+\phi_2=\rho_{C_2,1}$ sets $\tilde{\rho}_{C_2,1}=0$. From Eq. (B47), we then obtain $\rho_{C_2,u}=\{0,n_{C_2}\pi\}$. Similarly, Eq. (B48) gives $\rho_{\sigma_x,u}=\{0,\theta_{\sigma_x}\}$.

(iv) $w_{C_2}=1$, $w_{\sigma_x}=1$:
As previously, we can set $\rho_{C_2,u}=\{0,n_{C_2}\pi\}$. Equation (B48) then implies $\rho_{\sigma_x,u}=\{0,n_{\sigma_x}\pi\}$.

b. *Time-reversal symmetry*

Having determined all solutions corresponding to the lattice space-group symmetries, we now turn to time-reversal symmetry. As a first step, we substitute the solution (B12) into Eqs. (A12) and (A13), yielding:

$$\Delta_1\phi_{\mathcal{T}}=\theta_{\mathcal{T}T_1}+y\theta[1-(-1)^{w_{\mathcal{T}}}] \tag{B50}$$
$$\Delta_2\phi_{\mathcal{T}}(x,y,u)=\theta_{\mathcal{T}T_2}\,. \tag{B51}$$

The consistency relations for time-reversal symmetry, analogous to Eqs. (B15) and (B19), are

$$\Delta_1\phi_{\mathcal{T}}(x,y,u)+\Delta_2\phi_{\mathcal{T}}(x-1,y,u)$$

$$= \Delta_2 \phi_{\mathcal{T}}(x,y,u) + \Delta_1 \phi_{\mathcal{T}}(x,y-1,u) \tag{B52}$$

which impose the following constraint:

$$\theta[1-(-1)^{w_{\mathcal{T}}}] = 0 \quad \begin{cases} \theta \in [0,2\pi) & \text{if } w_{\mathcal{T}} = 0, \\ \theta = 0,\pi & \text{if } w_{\mathcal{T}} = 1\,. \end{cases} \tag{B53}$$

Substituting these conditions into Eqs. (B50) and (B51), we obtain the general solution

$$\phi_{\mathcal{T}}(x,y,u) = x\theta_{\mathcal{T}T_1} + y\theta_{\mathcal{T}T_2} + \rho_{\mathcal{T},u}\,, \tag{B54}$$

where $\rho_{\mathcal{T},u} \equiv \phi_{\mathcal{T}}(0,0,u)$. We now consider the two cases $w_{\mathcal{T}} = 0$ and $w_{\mathcal{T}} = 1$ separately.

$w_{\mathcal{T}} = 0$**:** In this case, the consistency relation does not impose any constraint on θ. Equation (A11) further sets

$$\theta_{\mathcal{T}T_1}, \theta_{\mathcal{T},T_2} = 0, \pi\,. \tag{B55}$$

The condition from Eq. (A14) can be rewritten as

$$\phi_{\mathcal{T}}(x,y,u) - (-1)^{w_{C_2}} \phi_{\mathcal{T}}(-x,-y,\bar{u}) = \theta_{\mathcal{T}C_2} \tag{B56}$$

which yields

$$w_{C_2} = 0,\ \theta_{\mathcal{T}T_i} = n_{\mathcal{T}T_i}\pi \tag{B57}$$

$$w_{C_2} = 1,\ \theta_{\mathcal{T}T_i} \neq 0 \tag{B58}$$

$$\rho_{\mathcal{T},u} - (-1)^{w_{C_2}} \rho_{\mathcal{T},\bar{u}} = \theta_{\mathcal{T}C_2}\,. \tag{B59}$$

Similarly, Eq. (A15) becomes

$$\phi_{\mathcal{T}}(x,y,u) - (-1)^{w_{\sigma_x}} \phi_{\mathcal{T}}(x+y,-y,\bar{u}) = \theta_{\mathcal{T}\sigma_x} \tag{B60}$$

leading to

$$w_{\sigma_x} = 0,\ 2\theta_{\mathcal{T}T_2} = \theta_{\mathcal{T}T_1} \tag{B61}$$

$$w_{\sigma_x} = 1,\ \theta_{\mathcal{T}T_1} = 0 \tag{B62}$$

$$\rho_{\mathcal{T},u} - (-1)^{w_{\sigma_x}} \rho_{\mathcal{T},\bar{u}} = \theta_{\mathcal{T}\sigma_x}\,. \tag{B63}$$

The solutions for $\rho_{\mathcal{T},u}$ follow from Eqs. (B59) and (B63):

$$(w_{C_2}, w_{\sigma_x}) = (0,0): \quad \rho_{\mathcal{T},u} = \{0, n_{\mathcal{T}}\pi\}, \tag{B64}$$

$$(w_{C_2}, w_{\sigma_x}) = (1,0): \quad \rho_{\mathcal{T},u} = \{0, n_{\mathcal{T}}\pi\}, \tag{B65}$$

$$(w_{C_2}, w_{\sigma_x}) = (0,1): \quad \rho_{\mathcal{T},u} = \{0, n_{\mathcal{T}}\pi\}, \tag{B66}$$

$$(w_{C_2}, w_{\sigma_x}) = (1,1): \quad \rho_{\mathcal{T},u} = \{0, \theta_{\mathcal{T}C_2}\}\,. \tag{B67}$$

$w_{\mathcal{T}} = 1$**:** In this case, the consistency relation Eq. (B53) enforces $2\theta = 0$, leaving only $\theta = 0, \pi$. Here, Eq. (A11) does not impose further constraints, while Eqs. (A14) and (A15) become

$$\phi_{\mathcal{T}}(x,y,u) - (-1)^{w_{C_2}} \phi_{\mathcal{T}}(-x,-y,\bar{u}) - 2\phi_{C_2}(x,y,u) = \theta_{\mathcal{T}C_2} \tag{B68}$$

$$\phi_{\mathcal{T}}(x,y,u) - (-1)^{w_{\sigma_x}} \phi_{\mathcal{T}}(x+y,-y,\bar{u}) - 2\phi_{\sigma_x}(x,y,u) = \theta_{\mathcal{T}\sigma_x}\,. \tag{B69}$$

Then, solving Eqs. (B68) and (B69) for the four possible (w_{C_2}, w_{σ_x}) cases yields

$(w_{C_2}, w_{\sigma_x}) = (0,0)$:

$$\theta = n\pi, \theta_{C_2T_i} = 0,\ \rho_{\mathcal{T},u} = \{0, n_{\mathcal{T}}\pi\}, \tag{B70}$$

$$\theta_{\sigma_xT_1} = n\pi, \theta_{\sigma_xT_2} = \frac{\theta}{2} + n_{\sigma_xT_2}\pi, \tag{B71}$$

$$\theta_{\mathcal{T}T_1} = n\pi, \theta_{\mathcal{T}T_2} = n_{TT_2}\pi. \tag{B72}$$

$(w_{C_2}, w_{\sigma_x}) = (1,0)$:

$$\theta = n\pi,\ \rho_{\mathcal{T},u} = \{0, n_{\mathcal{T}}\pi\}, \tag{B73}$$

$$\theta_{C_2T_1} = n\pi, \theta_{C_2T_2} = n_{C_2T_2}\pi, \tag{B74}$$

$$\theta_{\sigma_xT_1} = n\pi, \theta_{\sigma_xT_2} = 0,\ 2\theta_{\mathcal{T}T_2} = \theta_{\mathcal{T}T_1}. \tag{B75}$$

$(w_{C_2}, w_{\sigma_x}) = (0,1)$:

$$\theta = n\pi,\ \rho_{\mathcal{T},u} = \{0, n_{\mathcal{T}}\pi\}, \tag{B76}$$

$$\theta_{C_2T_1} = 0, \theta_{C_2T_2} = 0 \tag{B77}$$

$$\theta_{\sigma_xT_1} = 0, \theta_{\sigma_xT_2} = n_{\sigma_xT_2}\pi - \frac{\theta}{2}, \tag{B78}$$

$$\theta_{\mathcal{T}T_1} = -n\pi,\ \theta_{\mathcal{T}T_2} = n_{\mathcal{T}T_2}\pi. \tag{B79}$$

$(w_{C_2}, w_{\sigma_x}) = (1,1)$:

$$\theta = n\pi,\ \theta_{\mathcal{T}T_1} = 0,\ \rho_{\mathcal{T},u} = \{0, \theta_{\mathcal{T}}\}, \tag{B80}$$

$$\theta_{C_2T_1} = n\pi, \theta_{C_2T_2} = n_{C_2T_2}\pi, \tag{B81}$$

$$\theta_{\sigma_xT_1} = n\pi, \theta_{\sigma_xT_2} = 0. \tag{B82}$$

It is possible, and often convenient, to choose a gauge such that $\phi_{\mathcal{T}}(x,y,u) = 0$ for $w_{\mathcal{T}} = 1$, which ensures the resulting *Ansätze* contain only real hopping parameters. The required gauge transformation is

$$W(x,y,u) = \mathcal{F}_z\left(\frac{x\theta_{\mathcal{T}T_1}}{2} + \frac{y\theta_{\mathcal{T}T_2}}{2} + \frac{\rho_{\mathcal{T},u}}{2}\right). \tag{B83}$$

Applying this transformation for $\mathcal{O} \in \{\mathcal{T}, C_2, \sigma_x\}$ gives

$$\tilde{\phi}_{\mathcal{T}}(x,y,u) = 0, \tag{B84}$$

$$\tilde{\phi}_{C_2}(x,y,u) = -\phi_T(x,y,u) + \phi_{C_2}(x,y,u) + (-1)^{w_{C_2}}\phi_T(-x,-y,\bar{u}), \tag{B85}$$

$$\tilde{\phi}_{\sigma_x}(x,y,u) = -\phi_T(x,y,u) + \phi_{\sigma_x}(x,y,u) + (-1)^{w_{\sigma_x}}\phi_T(x+y,-y,\bar{u})\,. \tag{B86}$$

The algebraic PSG solutions for $(w_{T_1}, w_{T_2}) = (0,0)$ are summarized in Eqs. (31)–(35) and in Table I (rows 1—8).

2. U(1) class with $w_{T_1} = 0$, $w_{T_2} = 1$

a. *Lattice symmetries*

In this class of U(1) PSGs, the translation gauge transformations take the general form

$$W_{T_1}(x,y,u) = \mathcal{F}_z(\phi_{T_1}(x,y,u)), \tag{B87}$$
$$W_{T_2}(x,y,u) = \mathcal{F}_z(\phi_{T_2}(x,y,u))(i\tau^1)\,. \tag{B88}$$

Analogous to the case with $w_{T_1} = w_{T_2} = 0$, one can perform a local gauge transformation such that

$$\phi_{T_2}(x,y,u) = \phi_{T_1}(x,0,u) = 0\,. \tag{B89}$$

To determine $\phi_{T_1}(x,y,u)$, we use Eq. (A1) together with the above gauge choice, which yields

$$\phi_{T_1}(x,y,u) = \tfrac{1}{2}\big(1-(-1)^{y+1}\big)\theta\,. \tag{B90}$$

After a global phase shift and redefining $\theta \to 2\theta$, the resulting projective translations are

$$W_{T_1}(x,y,u) = \mathcal{F}_z[(-1)^y\theta], \tag{B91}$$
$$W_{T_2}(x,y,u) = i\tau^x\,. \tag{B92}$$

Substituting Eqs. (B91) and (B92) into Eqs. (A2) and (A3), respectively, we obtain

$$\Delta_1\phi_{C_2}(x,y,u) = -(-1)^{w_{C_2}}\theta_{C_2T_1} + (-1)^y\theta\big[1+(-1)^{w_{C_2}}\big],$$
$$\Delta_2\phi_{C_2}(x,y,u) = (-1)^{w_{C_2}-y}\theta_{C_2T_2}\,, \tag{B93}$$

which must satisfy the consistency relation (B15). This leads to the following constraint on θ:

$$\big[1+(-1)^{w_{C_2}}\big]\theta = 0, \quad \begin{cases}\theta = 0,\pi & \text{if } w_{C_2}=0,\\ \theta\in[0,2\pi) & \text{if } w_{C_2}=1.\end{cases} \tag{B94}$$

Using this constraint, the solution for ϕ_{C_2} follows from Eq. (B93):

$$\phi_{C_2}(x,y,u) = -(-1)^{w_{C_2}}\Big(x\theta_{C_2T_1} - \zeta_y\theta_{C_2T_2}\Big) + \rho_{C_2,u}\,, \tag{B95}$$

where $\zeta_y = \frac{1}{2}\big(1+(-1)^y\big)$.

A similar analysis can be applied to σ_x using Eqs. (A4) and (A5), together with the consistency condition (B19), which imposes

$$\big(1-(-1)^{w_{\sigma_x}}\big)\theta = 0, \quad \begin{cases}\theta\in[0,2\pi) & \text{if } w_{\sigma_x}=0\,,\\ \theta = 0,\pi & \text{if } w_{\sigma_x}=1\,.\end{cases} \tag{B96}$$

This yields

$$\phi_{\sigma_x}(x,y,u) = -\,(-1)^{w_{\sigma_x}}\big[x\theta_{\sigma_xT_1} - \zeta_y\theta_{\sigma_xT_2}\big] - (-1)^{w_{\sigma_x}}y\theta + \rho_{\sigma_x,u}\,. \tag{B97}$$

Case	w_{C_2} (rotations)	w_{σ_x} (reflections)	Constraints on θ
(i)	0	0	$0,\pi$
(ii)	1	0	$[0,2\pi)$
(iii)	0	1	$0,\pi$
(iv)	1	1	$0,\pi$

TABLE VIII. Allowed values of θ for different combinations of (w_{C_2}, w_{σ_x}).

The combined constraints from Eqs. (B94) and (B96) are summarized in Table VIII.

We now substitute the solutions (B95) and (B97) into the cyclic relations (A7) and (A8), which yield the following constraints:

$$\begin{aligned} C_2:\quad & w_{C_2}=0 : \theta_{C_2T_1}\neq 0,\ \theta_{C_2T_2} = n_{C_2T_2}\pi,\\ & w_{C_2}=1 : \theta_{C_2T_1} = n_{C_2T_1}\pi,\\ & \rho_{C_2,u} + (-1)^{w_{C_2}}\rho_{C_2,\bar{u}} = \theta_{C_2}. \end{aligned} \tag{B98}$$

$$\begin{aligned} \sigma_x:\quad & w_{\sigma_x}=0 : \theta_{\sigma_xT_1}=0,\ \theta_{\sigma_xT_2} = n_{\sigma_xT_2}\pi,\\ & w_{\sigma_x}=1 : \theta_{\sigma_xT_1}=0,\\ & \rho_{\sigma_x,u} + (-1)^{w_{\sigma_x}}\rho_{\sigma_x,\bar{u}} = \theta_{\sigma_x}. \end{aligned} \tag{B99}$$

Next, we perform the gauge transformation

$$W(x,y,u) = \mathcal{F}_z\left[(-1)^y\phi_u\right], \tag{B100}$$

and choose the phases ϕ_u appropriately to simplify the solutions in each case:

(i) $w_{C_2}=0,\ w_{\sigma_x}=0$:
No particular choice of ϕ_u further simplifies the solutions.

(ii) $w_{C_2}=0,\ w_{\sigma_x}=1$:
Choosing $\phi_1+\phi_2 = -\theta_{\sigma_xT_2}/2$ sets $\theta_{\sigma_xT_2}=0$, yielding

$$\phi_{C_2}(x,y,u) = -x\theta_{C_2T_1} + \zeta_y\theta_{C_2T_2} + \rho_{C_2,u}, \tag{B101}$$
$$\phi_{\sigma_x}(x,y,u) = y\theta + \rho_{\sigma_x,u}. \tag{B102}$$

(iii) $w_{C_2}=1,\ w_{\sigma_x}=0$:
Choosing $\phi_u+\phi_{\bar{u}} = -\theta_{C_2T_2}/2$ sets $\theta_{C_2T_2}=0$, leading to

$$\phi_{C_2}(x,y,u) = x\theta_{C_2T_1} + \rho_{C_2,u}, \tag{B103}$$
$$\phi_{\sigma_x}(x,y,u) = \zeta_y\theta_{\sigma_xT_2} - y\theta + \rho_{\sigma_x,u}. \tag{B104}$$

(iv) $w_{C_2}=1,\ w_{\sigma_x}=1$:
Using the same choice and setting $\theta_{C_2T_2}=0$ gives

$$\phi_{C_2}(x,y,u) = x\theta_{C_2T_1} + \rho_{C_2,u}, \tag{B105}$$

$$\phi_{\sigma_x}(x,y,u) = -\zeta_y \theta_{\sigma_x T_2} + y\theta + \rho_{\sigma_x,u}. \tag{B106}$$

Furthermore, Eq. (A6) enforces $\theta_{C_2T_1} = 0$ for all four combinations of (w_{C_2}, w_{σ_x}), together with the following additional constraints:

$$w_{C_2} = w_{\sigma_x} = 0: \quad \theta_{C_2T_2} = m\pi - \theta_{\sigma_x T_2}, \tag{B107}$$
$$w_{C_2} = w_{\sigma_x} = 1: \quad \theta_{\sigma_x T_2} = n_{\sigma_x T_2}\pi. \tag{B108}$$

In addition, Eq. (A10) imposes:

$$w_{C_2} = 0,\ w_{\sigma_x} = 0: \quad \theta_{C_2T_2} = m\pi - \theta_{\sigma_x T_2}, \tag{B109}$$
$$w_{C_2} = 1,\ w_{\sigma_x} = 0: \quad \theta = n\pi, \tag{B110}$$
$$w_{C_2} = 0,\ w_{\sigma_x} = 1: \quad \theta = n\pi, \tag{B111}$$
$$w_{C_2} = 1,\ w_{\sigma_x} = 1: \quad \theta_{\sigma_x T_2} = n_{\sigma_x T_2}\pi. \tag{B112}$$

Last, let us discuss how to fix all the ρ parameters. From the constraints imposed by (A6), Eqs. (A7), (A8), and (A10), we obtain

$$\begin{aligned}
\rho_{C_2,u} + (-1)^{w_{C_2}}\rho_{C_2,\bar{u}} &= \theta_{C_2},\\
\rho_{\sigma_x,u} + (-1)^{w_{\sigma_x}}\rho_{\sigma_x,\bar{u}} &= \theta_{\sigma_x},\\
\rho_{C_2,u} + (-1)^{w_{C_2}}\rho_{\sigma_x,\bar{u}} + (-1)^{w_{C_2}+w_{\sigma_x}}\rho_{C_2,u} &\\
+(-1)^{w_{\sigma_x}}\rho_{\sigma_x,\bar{u}} &= \theta_{C_2\sigma_x},\\
\rho_{C_2,u} - (-1)^{w_{C_2}}\rho_{\sigma_x,\bar{u}} - (-1)^{w_{C_2}+w_{\sigma_x}}\rho_{C_2,u} &\\
+(-1)^{w_{\sigma_x}}\rho_{\sigma_x,\bar{u}} &= \theta_{C_2\sigma_x T_2}.
\end{aligned}$$

These relations yield the solutions

$$w_{C_2} = 0,\ w_{\sigma_x} = 0: \quad \begin{cases} \rho_{C_2,u} \in \{0,\ \theta_{C_2}\}, \\ \rho_{\sigma_x,u} \in \{0,\ \theta_{\sigma_x}\}, \end{cases} \tag{B113}$$

$$\text{All other cases}: \quad \begin{cases} \rho_{C_2,u} \in \{0,\ n_{C_2}\pi\}, \\ \rho_{\sigma_x,u} \in \{0,\ n_{\sigma_x}\pi\}. \end{cases} \tag{B114}$$

b. *Time-reversal symmetry*

We now analyze the PSG solutions associated with time-reversal symmetry. From Eqs. (A12) and (A13), we arrive at

$$\Delta_1\phi_{\mathcal{T}} = \theta_{\mathcal{T}T_1} + (-1)^y\theta[1-(-1)^{w_{\mathcal{T}}}], \tag{B115}$$
$$\Delta_2\phi_{\mathcal{T}} = (-1)^y\theta_{\mathcal{T}T_2}\,, \tag{B116}$$

which, when substituted into the consistency condition (B52), result in

$$\left(1-(-1)^{w_{\sigma_x}}\right) = 0, \quad \begin{cases} \theta \in [0,2\pi) & \text{if } w_{\mathcal{T}} = 0, \\ \theta = 0,\pi & \text{if } w_{\mathcal{T}} = 1. \end{cases} \tag{B117}$$

A general solution for $\phi_{\mathcal{T}}(x,y,u)$ can then be written by combining these constraints on θ with Eqs. (B115) and (B116):

$$\theta_{\mathcal{T}}(x,y,u) = x\theta_{\mathcal{T}T_1} + \zeta_y\theta_{\mathcal{T}T_2} + \rho_{\mathcal{T},u}\,. \tag{B118}$$

We now consider separately the two cases $w_{\mathcal{T}} = 0$ and $w_{\mathcal{T}} = 1$.

$w_{\mathcal{T}} = 0$: Equation (A11) requires $\theta_{\mathcal{T}T_i} = n_{\mathcal{T}T_i}\pi$. Furthermore, solving Eqs. (A14) and (A15) gives $\theta_{\mathcal{T}T_1} = 0$, with

$$w_{C_2} = 1,\ w_{\sigma_x} = 1: \quad \rho_{\mathcal{T},u} = \{0, \theta_{\mathcal{T}}\}, \tag{B119}$$
$$\text{All other cases}: \quad \rho_{\mathcal{T},u} = \{0, n_{\mathcal{T}}\pi\}\,. \tag{B120}$$

$w_{\mathcal{T}} = 1$: Solving Eqs. (A11), (A14), and (A15) yields $\theta_{\mathcal{T}T_1} = 0$, with the following possibilities:

$$\begin{aligned}
w_{C_2} = 0,\ w_{\sigma_x} = 0 &: \theta_{\mathcal{T}T_2} \in [0,2\pi), \quad \rho_{\mathcal{T},u} = \{0,\theta_{\mathcal{T}}\},\\
w_{C_2} = 0,\ w_{\sigma_x} = 1 &: \theta_{\mathcal{T}T_2} = n_{\mathcal{T}T_2}\pi, \quad \rho_{\mathcal{T},u} = \{0, n_{\mathcal{T}}\pi\},\\
w_{C_2} = 1,\ w_{\sigma_x} = 0 &: \theta_{\mathcal{T}T_2} = n_{\mathcal{T}T_2}\pi, \quad \rho_{\mathcal{T},u} = \{0, n_{\mathcal{T}}\pi\},\\
w_{C_2} = 1,\ w_{\sigma_x} = 1 &: \theta_{\mathcal{T}T_2} = n_{\mathcal{T}T_2}\pi, \quad \rho_{\mathcal{T},u} = \{0,\theta_{\mathcal{T}}\}\,.
\end{aligned}$$

Finally, the complete set of algebraic PSG solutions for the $(w_{T_1}, w_{T_2}) = (0,1)$ class is summarized in Eqs. (31)–(35) and in Table I (rows 9–16).

Appendix C: $\mathbb{Z}_2$ projective symmetry groups

In this section, we derive the algebraic solutions for projective symmetry groups assuming a $\mathbb{Z}_2$ invariant gauge group. The *Ansatz* now incorporates both hopping and pairing terms, leading to the general form

$$u_{ij} = i\chi^0_{ij}\tau^0 + \chi^3_{ij}\tau^3 + \Delta^1_{ij}\tau^1 + \Delta^2_{ij}\tau^2. \tag{C1}$$

Here, the coefficients of τ^3 and τ^0 correspond to real and imaginary hopping amplitudes, respectively, while the coefficients of τ^1 and τ^2 correspond to real and imaginary pairing amplitudes. The elements of the $\mathbb{Z}_2$ IGG are parameterized by $\eta_{\dots} \in \{\pm 1\}$. We derive the projective realizations of the lattice and time-reversal symmetries separately in the following subsections.

1. Lattice symmetries

Analogous to the U(1) case, an appropriate choice of local gauge allows one to set $W_{T_1}(x,0,u) = W_{T_2}(x,y,u) = \tau^0$. Substituting this into the gauge condition (A1) yields the projective representations of the translations:

$$W_{T_1}(x,y,u) = \eta^y_{T_1}\tau^0, \quad W_{T_2}(x,y,u) = \tau^0\,. \tag{C2}$$

Label	PSG No.	θ	$\theta_{C_2T_1}$	$\theta_{C_2T_2}$	$\theta_{\sigma_xT_1}$	$\theta_{\sigma_xT_2}$	$\theta_{\mathcal{T}T_2}$	$\rho_{C_2,u}$	$\rho_{\sigma_x,u}$	$\rho_{\mathcal{T},u}$
U1	5	0	0	0	0	0	0	0	0	0
U2	8	0	0	0	0	0	0	π	π	0
U3	5	π	π	0	0	0	0	0	0	0
U4	8	π	π	0	0	0	0	π	π	0
U5	13	0	-	π	-	π	0	0	0	0
U6	16	0	-	0	-	0	π	π	π	0
U7	2	θ	0	0	0	0	π	0	π	0

TABLE IX. PSG parameter values θ and ρ for the U(1) states on the trellis lattice, corresponding to the *Ansätze* illustrated in Fig. 3.

To determine the PSG for C_2, we insert Eq. (C2) into Eqs. (A2) and (A3), leading to the recursion relations

$$W_{C_2}(x,y,u) = \eta_{C_2T_1} W_{C_2}(x-1,y,u), \tag{C3}$$
$$W_{C_2}(x,y,u) = \eta_{C_2T_2} W_{C_2}(x,y-1,u), \tag{C4}$$

solving which gives

$$W_{C_2}(x,y,u) = \eta^y_{C_2T_2}\eta^x_{C_2T_1} W_{C_2}(0,0,u)\,. \tag{C5}$$

Similarly, using Eqs. (A4), (A5) and (C2), we obtain

$$W_{\sigma_x}(x,y,u) = \eta_{\sigma_xT_1} W_{\sigma_x}(x-1,y,u), \tag{C6}$$
$$W_{\sigma_x}(x,y,u) = \eta_{T_1}^{-y+1}\eta_{\sigma_xT_2} W_{\sigma_x}(x,y-1,u), \tag{C7}$$

which are solved by

$$W_{\sigma_x}(x,y,u) = \eta_{T_1}^{-\frac{y(y-1)}{2}}\eta^y_{\sigma_xT_2}\eta^x_{\sigma_xT_1} W_{\sigma_x}(0,0,u)\,. \tag{C8}$$

From Eq. (A6), we obtain

$$W_{C_2,u}W_{\sigma_x,\bar{u}}W_{C_2,u}W_{\sigma_x,\bar{u}} = \eta_{C_2\sigma_x}\tau^0, \tag{C9}$$
$$\eta_{C_2T_1} = \eta_{\sigma_xT_1}. \tag{C10}$$

Similarly, Eq. (A7) yields

$$W_{C_2,u}W_{C_2,\bar{u}} = \eta_{C_2}\tau^0, \tag{C11}$$

while Eq. (A8) gives

$$W_{\sigma_x,u}W_{\sigma_x,\bar{u}} = \eta_{\sigma_x}\tau^0, \tag{C12}$$
$$\eta_{\sigma_xT_1} = \eta_{T_1}. \tag{C13}$$

Further gauge fixing can be implemented through a transformation of the form

$$W(x,y,u) = \eta^x_x\eta^y_y\tau^0, \tag{C14}$$

which leaves the translational gauge structure unchanged, up to global sign factors. These global signs can be absorbed into the IGG freedom, allowing us to set one of them to $+1$ without loss of generality. Under this transformation, the operators $W_{C_2}(x,y,u)$ and $W_{\sigma_x}(x,y,u)$ transform as

$$\tilde{W}_{C_2}(x,y,u) = \eta^y_{C_2T_2}\eta^x_{C_2T_1} W_{C_2,u}, \tag{C15}$$
$$\tilde{W}_{\sigma_x}(x,y,u) = \eta^y_x\eta_{T_1}^{-\frac{y(y-1)}{2}}\eta^y_{\sigma_xT_2}\eta^x_{\sigma_xT_1} W_{\sigma_x,u}. \tag{C16}$$

We observe that $W_{C_2}(x,y,u)$ remains unaffected, while $W_{\sigma_x}(x,y,u)$ acquires an additional sign structure. By choosing $\eta_x = \eta_{\sigma_xT_2}$, one can eliminate the parameter $\eta_{\sigma_xT_2}$ from W_{σ_x}. In this gauge, the solutions take the form

$$W_{T_1}(x,y,u) = \eta^y_{T_1}\tau^0, \quad W_{T_2}(x,y,u) = \tau^0, \tag{C17}$$
$$W_{C_2}(x,y,u) = \eta^y_{C_2T_2}\eta^x_{T_1} W_{C_2,u}, \tag{C18}$$
$$W_{\sigma_x}(x,y,u) = \eta_{T_1}^{-\frac{y(y-1)}{2}+x} W_{\sigma_x,u}. \tag{C19}$$

For notational convenience, we omit the tilde in what follows.

Next, combining (A6)–(A8), we obtain the constraints

$$W_{C_2,u}W_{C_2,\bar{u}} = \eta_{C_2}\tau^0, \tag{C20}$$
$$W_{\sigma_x,u}W_{\sigma_x,\bar{u}} = \eta_{\sigma_x}\tau^0, \tag{C21}$$
$$W_{C_2,u}W_{\sigma_x,\bar{u}}W_{C_2,u}W_{\sigma_x,\bar{u}} = \eta_{C_2\sigma_x}\tau^0. \tag{C22}$$

At this stage, one may still perform a sublattice-dependent gauge transformation of the form $W(x,y,u) = W_u$, under which the sublattice-dependent components transform as

$$\tilde{W}_{C_2,u} = W_u^\dagger W_{C_2,u} W_{\bar{u}}, \tag{C23}$$
$$\tilde{W}_{\sigma_x,u} = W_u^\dagger W_{\sigma_x,u} W_{\bar{u}}. \tag{C24}$$

By choosing $W_1 = W_{\sigma_x,u}W_2$, we can fix $W_{\sigma_x,1} \to \tau^0$. Substituting into Eq. (C21), we obtain

$$W_{\sigma_x} = \{\tau^0, \eta_{\sigma_x}\tau^0\}. \tag{C25}$$

Combining Eq. (C20) with Eq. (C25), we find

$$W^2_{C_2,u} = \eta_{C_2\sigma_x}\tau^0 \;\Rightarrow\; W^2_{C_2,1} = W^2_{C_2,2} = \eta_{C_2\sigma_x}\tau^0, \tag{C26}$$

leading to two distinct cases:

$$\eta_{C_2\sigma_x} = +1 : W_{C_2,u} = \eta_{C,u}\tau^0, \tag{C27}$$
$$\eta_{C_2\sigma_x} = -1 : W_{C_2,u} = i\vec{\alpha}_{C_2,u}\cdot\vec{\tau}. \tag{C28}$$

Plugging Eq. (C27) back into Eq. (C20), we obtain the condition

$$\eta_{C,1}\eta_{C,2} = \eta_{C_2}, \tag{C29}$$

which implies

$$W_{C_2,u} = \{\tau^0, \eta_{C_2}\tau^0\}. \tag{C30}$$

On the other hand, substituting Eq. (C28) into Eq. (C20) gives

$$W_{C_2,u} = \{1, \eta_{C_2}\}\, i\,\tau^z. \tag{C31}$$

2. Time-reversal symmetry

Akin to the U(1) case, one can employ Eqs. (A11)–(A15) to determine the $\mathbb{Z}_2$ PSG associated with time-reversal symmetry. On substituting Eq. (C2) into Eqs. (A12) and (A13), we obtain

$$W_{\mathcal{T}}(x,y,u) = \eta^x_{\mathcal{T}x}\eta^y_{\mathcal{T}y}W_{\mathcal{T},u}. \tag{C32}$$

Next, inserting the solutions given by Eqs. (C5), (C8), and (C32) into Eqs. (A11), (A14), and (A15), we arrive at the following constraints:

$$W^2_{\mathcal{T},u} = \eta_{\mathcal{T}}\tau^0, \tag{C33}$$
$$W_{\mathcal{T},u}W_{C_2,u}W^{-1}_{\mathcal{T},\bar{u}}W^{-1}_{C_2,u} = \eta_{\mathcal{T}C_2}\tau^0\,, \tag{C34}$$
$$\eta_{\mathcal{T}x} = 1, \tag{C35}$$
$$W_{\mathcal{T},u}W_{\sigma_x,u}W^{-1}_{\mathcal{T},\bar{u}}W^{-1}_{\sigma_x,u} = \eta_{\mathcal{T}\sigma_x}\tau^0\,. \tag{C36}$$

From Eqs. (C25) and (C36), one deduces that

$$W_{\mathcal{T},2} = \eta_{\mathcal{T}\sigma_x}W_{\mathcal{T},1}. \tag{C37}$$

Combining this with Eq. (C33) leads to

$$\eta_{\mathcal{T}} = +1 : \quad W_{\mathcal{T},u} = \{1, \eta_{\mathcal{T}\sigma_x}\}\tau^0, \tag{C38}$$
$$\eta_{\mathcal{T}} = -1 : \quad W_{\mathcal{T},u} = \{1, \eta_{\mathcal{T}\sigma_x}\}\, i\,\hat{\boldsymbol{v}}\cdot\hat{\tau}, \tag{C39}$$

where $\hat{\boldsymbol{v}} \in \mathbb{R}^3$ is a unit vector. Importantly, the case $\eta_{\mathcal{T}\sigma_x} = +1$ with $\eta_{\mathcal{T}} = +1$ does not yield a PSG compatible with nonvanishing mean-field amplitudes, and is therefore excluded from the classification. The remaining ambiguity associated with $\hat{\boldsymbol{v}}$ is resolved through the constraint in Eq. (C34). All gauge-inequivalent solutions, including those derived here, are summarized in Table II.

Label	PSG No.	θ_{T_1}	$\theta_{C_2T_2}$	θ_{σ_x}	$\theta_{\mathcal{T}_y}$	θ_{C_2}	$\theta_{\mathcal{T}}$
Z1	2	0	0	0	0	0	0
Z2	2	0	0	0	π	0	0
Z3	2	π	0	0	0	0	0
Z4	2	π	0	0	π	0	0
Z5	2	0	π	0	π	0	0
Z6	2	π	π	0	π	0	0
Z7	2	0	0	0	0	0	π
Z8	2	π	0	0	0	0	π
Z9	2	0	0	π	0	π	π
Z10	2	π	0	π	0	π	π
Z11	2	0	π	0	0	0	π
Z12	2	0	π	π	0	π	π
Z13	2	π	π	π	0	π	π
Z14	2	0	π	π	π	π	π
Z15	2	π	0	0	π	0	π
Z16	2	0	0	0	π	0	π
Z17	2	π	π	π	π	π	π
Z18	5	0	π	0	π	0	0
Z19	5	π	π	0	π	0	0
Z20	5	0	0	0	π	π	0
Z21	5	π	0	0	π	π	0
Z22	5	0	0	0	0	π	π
Z23	5	π	0	0	0	π	π
Z24	5	0	0	π	0	π	π
Z25	5	π	0	π	0	π	π

TABLE X. Representative PSG phase parameters θ for $\mathbb{Z}_2$ states on the trellis lattice. Each row corresponds to a gauge-inequivalent *Ansatz* labeled Z1–Z25. The labeling scheme follows the U(1) case: each η_i is represented by its phase angle $\theta_i = \mathrm{Arg}(\eta_i)$. For example, $\eta_{T_1} = 1$ corresponds to $\theta_{T_1} = 0$, while $\eta_{T_1} = -1$ corresponds to $\theta_{T_1} = \pi$. This convention is applied to all η_i with $i = T_1, C_2T_2, \sigma_x, \mathcal{T}_y, C_2, \mathcal{T}$.

Appendix D: Construction of mean-field *Ansätze*

Having obtained all projective realizations of the space-group symmetry elements, one can construct lattice-symmetric mean-field *Ansätze* using the condition

$$W^\dagger_{\mathcal{O}}(\mathcal{O}(i))\, u_{\mathcal{O}(i)\mathcal{O}(j)}\, W_{\mathcal{O}}(\mathcal{O}(j)) = u_{ij}. \tag{D1}$$

For a composite symmetry operator $\mathcal{O}_3 = \mathcal{O}_2\mathcal{O}_1$, this condition becomes

$$W^\dagger_{\mathcal{O}_1}(\mathcal{O}_1(i))\, W^\dagger_{\mathcal{O}_2}(\mathcal{O}_3(i))\, u_{\mathcal{O}_3(i)\mathcal{O}_3(j)} \times W_{\mathcal{O}_2}(\mathcal{O}_3(j))\, W_{\mathcal{O}_1}(\mathcal{O}_1(j)) = u_{ij}. \tag{D2}$$

Analogous conditions can be derived for any *Ansatz* involving longer strings of symmetry operations.

We define symmetry-allowed mean-field parameters on representative bonds within a unit cell. The corresponding parameters on all other bonds are generated via translations:

$$\text{On } J_v \text{ bonds: } u_{(0,0,1),(0,0,2)} = u_v, \tag{D3}$$

$$\text{On } J_h \text{ bonds: } u_{(0,0,1),(1,0,1)} = u_h, \tag{D4}$$

$$u_{(0,0,2),(1,0,2)} = u'_h, \tag{D5}$$

$$\text{On } J_z \text{ bonds: } u_{(0,0,1),(0,1,2)} = u_z, \tag{D6}$$

$$u_{(0,0,1),(-1,1,2)} = u'_z. \tag{D7}$$

A symmetry operation $\mathcal{O}$ can affect a link field u_{ij} in one of three ways:

1. Leave it invariant: $\mathcal{O} : u_{ij} \to u_{ij}$.
2. Reverse its direction: $\mathcal{O} : u_{ij} \to u_{ji} = u_{ij}^\dagger$.
3. Map it to a different, symmetry-equivalent link: $\mathcal{O} : u_{ij} \to u_{i'j'}$, with $\langle i'j' \rangle \neq \langle ij \rangle$.

The first two scenarios determine symmetry-allowed mean-field parameters, while the third relates distinct but symmetry-equivalent bonds across the lattice.

The conditions relevant for our classification are

$$\sigma_x : \quad u_v \to u_v^\dagger, \tag{D8}$$

$$C_2 : \quad u_v \to u_v^\dagger, \tag{D9}$$

$$C_2\sigma_x : \quad u_v \to u_v, \tag{D10}$$

$$T_1\, C_2\sigma_x : \quad u_h \to u_h^\dagger, \tag{D11}$$

$$\sigma_x : \quad u_h \to u'_h, \tag{D12}$$

$$T_2\, C_2 : \quad u_z \to u_z^\dagger, \tag{D13}$$

$$\sigma_x C_2 : \quad u_z \to u'_z. \tag{D14}$$

The corresponding projective symmetry conditions read:

$$W^\dagger_{\sigma_x}(0,0,2) u_v^\dagger W_{\sigma_x}(0,0,1) = u_v, \tag{D15}$$

$$W^\dagger_{C_2}(0,0,2) u_v^\dagger W_{C_2}(0,0,1) = u_v, \tag{D16}$$

$$W^\dagger_{\sigma_x}(0,0,2) W^\dagger_{C_2}(0,0,1) u_v W_{C_2}(0,0,2) W_{\sigma_x}(0,0,1) = u_v, \tag{D17}$$

$$W^\dagger_{\sigma_x}(0,0,2) W^\dagger_{C_2}(0,0,1) W^\dagger_{T_1}(1,0,1) u_h^\dagger W_{T_1}(0,0,1) W_{C_2}(-1,0,1) W_{\sigma_x}(1,0,2) = u_h, \tag{D18}$$

$$W^\dagger_{\sigma_x}(0,0,2) u'^\dagger_h W_{\sigma_x}(1,0,2) = u_h, \tag{D19}$$

$$W^\dagger_{C_2}(0,0,2) W^\dagger_{T_2}(0,1,2) u_z^\dagger W_{T_2}(0,0,1) W_{C_2}(0,-1,1) = u_z, \tag{D20}$$

$$W^\dagger_{C_2}(0,0,2) W^\dagger_{\sigma_x}(0,0,1) u'^\dagger_z W_{\sigma_x}(-1,1,2) W_{C_2}(0,-1,1) = u_z\,. \tag{D21}$$

Additionally, time-reversal invariance dictates that

$$W^\dagger_{\mathcal{T}}(i)\, u_{ij}\, W_{\mathcal{T}}(j) = -u_{ij}. \tag{D22}$$

[1] A. Auerbach, *Interacting Electrons and Quantum Magnetism* (Springer Science & Business Media, New York, NY, 2012).

[2] S. Sachdev, *Quantum Phases of Matter* (Cambridge University Press, 2023).

[3] Y. Ran, M. Hermele, P. A. Lee, and X.-G. Wen, Projected-Wave-Function Study of the Spin-1/2 Heisenberg Model on the Kagomé Lattice, Phys. Rev. Lett. **98**, 117205 (2007).

[4] Y. Iqbal, F. Becca, S. Sorella, and D. Poilblanc, Gapless spin-liquid phase in the kagome spin-$\frac{1}{2}$ Heisenberg antiferromagnet, Phys. Rev. B **87**, 060405 (2013).

[5] Y. Iqbal, W.-J. Hu, R. Thomale, D. Poilblanc, and F. Becca, Spin liquid nature in the Heisenberg $J_1 - J_2$ triangular antiferromagnet, Phys. Rev. B **93**, 144411 (2016).

[6] Y. Iqbal, D. Poilblanc, and F. Becca, Vanishing spin gap in a competing spin-liquid phase in the kagome Heisenberg antiferromagnet, Phys. Rev. B **89**, 020407 (2014).

[7] Y. Iqbal, D. Poilblanc, and F. Becca, Spin-$\frac{1}{2}$ Heisenberg J_1–J_2 antiferromagnet on the kagome lattice, Phys. Rev. B **91**, 020402 (2015).

[8] S. Hu, W. Zhu, S. Eggert, and Y.-C. He, Dirac Spin Liquid on the Spin-1/2 Triangular Heisenberg Antiferromagnet, Phys. Rev. Lett. **123**, 207203 (2019).

[9] W.-J. Hu, W. Zhu, Y. Zhang, S. Gong, F. Becca, and D. N. Sheng, Variational Monte Carlo study of a chiral spin liquid in the extended Heisenberg model on the kagome lattice, Phys. Rev. B **91**, 041124 (2015).

[10] S.-S. Gong, W. Zhu, L. Balents, and D. N. Sheng, Global phase diagram of competing ordered and quantum spin-liquid phases on the kagome lattice, Phys. Rev. B **91**, 075112 (2015).

[11] Y.-C. He, M. P. Zaletel, M. Oshikawa, and F. Pollmann, Signatures of Dirac Cones in a DMRG Study of the Kagome Heisenberg Model, Phys. Rev. X **7**, 031020 (2017).

[12] L. Balents, Spin liquids in frustrated magnets, Nature **464**, 199 (2010).

[13] L. Savary and L. Balents, Quantum spin liquids: a review, Rep. Prog. Phys. **80**, 016502 (2017).

[14] S. A. Kivelson and S. Sondhi, 50 years of quantum spin liquids, Nat. Rev. Phys. **5**, 368 (2023).

[15] T. Arh, B. Sana, M. Pregelj, P. Khuntia, Z. Jagličić, M. Le, P. Biswas, P. Manuel, L. Mangin-Thro, A. Ozarowski, *et al.*, The Ising triangular-lattice antiferromagnet neodymium heptatantalate as a quantum spin liquid candidate, Nat. Mater. **21**, 416 (2022).

[16] B. Gao, T. Chen, D. W. Tam, C.-L. Huang, K. Sasmal, D. T. Adroja, F. Ye, H. Cao, G. Sala, M. B. Stone, *et al.*, Experimental signatures of a three-dimensional quantum spin liquid in effective spin-1/2 $Ce_2Zr_2O_7$ pyrochlore, Nat. Phys. **15**, 1052 (2019).

[17] F. Lu, L. Yuan, J. Zhang, B. Li, Y. Luo, and Y. Li, The observation of quantum fluctuations in a kagome Heisenberg antiferromagnet, Commun. Phys. **5**, 272 (2022).

[18] L. Clark, G. J. Nilsen, E. Kermarrec, G. Ehlers, K. S. Knight, A. Harrison, J. P. Attfield, and B. D. Gaulin, From Spin Glass to Quantum Spin Liquid Ground States in Molybdate Pyrochlores, Phys. Rev. Lett. **113**, 117201 (2014).

[19] K. Plumb, H. J. Changlani, A. Scheie, S. Zhang, J. Krizan, J. Rodriguez-Rivera, Y. Qiu, B. Winn, R. Cava, and C. L. Broholm, Continuum of quantum fluctuations in a three-dimensional $S = 1$ Heisenberg magnet, Nat. Phys. **15**, 54 (2019).

[20] E. M. Smith, O. Benton, D. R. Yahne, B. Placke, R. Schäfer, J. Gaudet, J. Dudemaine, A. Fitterman, J. Beare, A. R. Wildes, S. Bhattacharya, T. DeLazzer, C. R. C. Buhariwalla, N. P. Butch, R. Movshovich, J. D. Garrett, C. A. Marjerrison, J. P. Clancy, E. Kermarrec, G. M. Luke, A. D. Bianchi, K. A. Ross, and B. D. Gaulin, Case for a $U(1)_\pi$ Quantum Spin Liquid Ground State in the Dipole-Octupole Pyrochlore $Ce_2Zr_2O_7$, Phys. Rev. X **12**, 021015 (2022).

[21] R. Sibille, N. Gauthier, E. Lhotel, V. Porée, V. Pomjakushin, R. A. Ewings, T. G. Perring, J. Ollivier, A. Wildes, C. Ritter, *et al.*, A quantum liquid of magnetic octupoles on the pyrochlore lattice, Nat. Phys. **16**, 546 (2020).

[22] G. H. Wannier, Antiferromagnetism. The Triangular Ising Net, Phys. Rev. **79**, 357 (1950).

[23] J. Vannimenus and G. Toulouse, Theory of the frustration effect. II. Ising spins on a square lattice, J. Phys. C: Solid State Phys. **10**, L537 (1977).

[24] G. Toulouse, The frustration model, in *Modern Trends in the Theory of Condensed Matter* (Springer, Berlin, Heidelberg, 1980) pp. 195–203.

[25] D. J. J. Farnell, O. Götze, J. Richter, R. F. Bishop, and P. H. Y. Li, Quantum $s = \frac{1}{2}$ antiferromagnets on Archimedean lattices: The route from semiclassical magnetic order to nonmagnetic quantum states, Phys. Rev. B **89**, 184407 (2014).

[26] J. Oitmaa and D. D. Betts, The ground state of two quantum models of magnetism, Can. J. Phys. **56**, 897 (1978).

[27] N. Trivedi and D. M. Ceperley, Green-function Monte Carlo study of quantum antiferromagnets, Phys. Rev. B **40**, 2737 (1989).

[28] A. W. Sandvik, Finite-size scaling of the ground-state parameters of the two-dimensional Heisenberg model, Phys. Rev. B **56**, 11678 (1997).

[29] E. V. Castro, N. M. R. Peres, K. S. D. Beach, and A. W. Sandvik, Site dilution of quantum spins in the honeycomb lattice, Phys. Rev. B **73**, 054422 (2006).

[30] A. F. Albuquerque, D. Schwandt, B. Hetényi, S. Capponi, M. Mambrini, and A. M. Läuchli, Phase diagram of a frustrated quantum antiferromagnet on the honeycomb lattice: Magnetic order versus valence-bond crystal formation, Phys. Rev. B **84**, 024406 (2011).

[31] B. Sriram Shastry and B. Sutherland, Exact ground state of a quantum mechanical antiferromagnet, Physica B+C **108**, 1069 (1981).

[32] R. R. P. Singh and D. A. Huse, Three-sublattice order in triangular- and Kagomé-lattice spin-half antiferromagnets, Phys. Rev. Lett. **68**, 1766 (1992).

[33] B. Bernu, C. Lhuillier, and L. Pierre, Signature of Néel order in exact spectra of quantum antiferromagnets on finite lattices, Phys. Rev. Lett. **69**, 2590 (1992).

[34] L. Capriotti, A. E. Trumper, and S. Sorella, Long-range Néel order in the triangular Heisenberg model, Phys. Rev. Lett. **82**, 3899 (1999).

[35] G. Misguich, C. Lhuillier, B. Bernu, and C. Waldtmann, Spin-liquid phase of the multiple-spin exchange Hamiltonian on the triangular lattice, Phys. Rev. B **60**, 1064 (1999).

[36] D. Schmalfuß, P. Tomczak, J. Schulenburg, and J. Richter, The spin-$\frac{1}{2}$ Heisenberg antiferromagnet on a $\frac{1}{7}$-depleted triangular lattice: Ground-state properties, Phys. Rev. B **65**, 224405 (2002).

[37] D. J. J. Farnell, R. Darradi, R. Schmidt, and J. Richter, Spin-half Heisenberg antiferromagnet on two archimedian lattices: From the bounce lattice to the maple-leaf lattice and beyond, Phys. Rev. B **84**, 104406 (2011).

[38] J. Beck, J. Bodky, J. Motruk, T. Müller, R. Thomale, and P. Ghosh, Phase diagram of the $J{-}J_d$ Heisenberg model on the maple leaf lattice: Neural networks and density matrix renormalization group, Phys. Rev. B **109**, 184422 (2024).

[39] P. Ghosh, T. Müller, and R. Thomale, Another exact ground state of a two-dimensional quantum antiferromagnet, Phys. Rev. B **105**, L180412 (2022).

[40] L. Gresista, C. Hickey, S. Trebst, and Y. Iqbal, Candidate quantum disordered intermediate phase in the Heisenberg antiferromagnet on the maple-leaf lattice, Phys. Rev. B **108**, L241116 (2023).

[41] P. Ghosh, Where is the spin liquid in maple-leaf quantum magnet?, arXiv:2401.09422.

[42] M. Gembé, L. Gresista, H.-J. Schmidt, C. Hickey, Y. Iqbal, and S. Trebst, Noncoplanar orders and quantum disordered states in maple-leaf antiferromagnets, Phys. Rev. B **110**, 085151 (2024).

[43] J. Sonnenschein, A. Maity, C. Liu, R. Thomale, F. Ferrari, and Y. Iqbal, Candidate quantum spin liquids on the maple-leaf lattice, Phys. Rev. B **110**, 014414 (2024).

[44] J. Richter, J. Schulenburg, and A. Honecker, Quantum magnetism in two dimensions: From semi-classical Néel order to magnetic disorder, in *Quantum Magnetism*, edited by U. Schollwöck, J. Richter, D. J. J. Farnell, and R. F. Bishop (Springer, Berlin, Heidelberg, 2004) pp. 85–153.

[45] B. Normand, K. Penc, M. Albrecht, and F. Mila, Phase diagram of the $S{=}\frac{1}{2}$ frustrated coupled ladder system, Phys. Rev. B **56**, R5736 (1997).

[46] S. Dalosto and J. Riera, Magnetic order in ferromagnetically coupled spin ladders, Phys. Rev. B **62**, 928 (2000).

[47] D. Maiti and M. Kumar, Melting of ferromagnetic order on a trellis ladder, J. Magn. Magn. Mater. **486**, 165266 (2019).

[48] I. Rabuffo, M. Mercaldo, L. De Cesare, and A. Caramico

D'Auria, Field-induced quantum criticality of systems with ferromagnetically coupled structural spin units, Phys. Lett. A **356**, 174 (2006).
[49] S. Gopalan, T. M. Rice, and M. Sigrist, Spin ladders with spin gaps: A description of a class of cuprates, Phys. Rev. B **49**, 8901 (1994).
[50] D. C. Johnston, M. Troyer, S. Miyahara, D. Lidsky, K. Ueda, M. Azuma, Z. Hiroi, M. Takano, M. Isobe, Y. Ueda, M. A. Korotin, V. I. Anisimov, A. V. Mahajan, and L. L. Miller, Magnetic Susceptibilities of Spin-$\frac{1}{2}$ Antiferromagnetic Heisenberg Ladders and Applications to Ladder Oxide Compounds, arXiv:cond-mat/0001147 [cond-mat.str-el].
[51] S. Miyahara, M. Troyer, D. C. Johnston, and K. Ueda, Quantum Monte Carlo Simulation of the Trellis Lattice Heisenberg Model for $SrCu_2O_3$ and CaV_2O_5, J. Phys. Soc. Jpn. **67**, 3918 (1998).
[52] J. A. Riera and S. D. Dalosto, Effects of interladder couplings in the trellis lattice, Phys. Rev. B **63**, 144431 (2001).
[53] K. P. Schmidt and G. S. Uhrig, Two dimensionality of magnetic excitations on the trellis lattice: $(La, Sr, Ca)_{14}Cu_{24}O_{41}$ and $SrCu_2O_3$, Phys. Rev. B **75**, 224414 (2007).
[54] R. Zinke, S.-L. Drechsler, and J. Richter, Influence of interchain coupling on spiral ground-state correlations in frustrated spin-$\frac{1}{2}$ J_1-J_2 Heisenberg chains, Phys. Rev. B **79**, 094425 (2009).
[55] D. Maiti and M. Kumar, Quantum phase diagram of a frustrated spin-$\frac{1}{2}$ system on a trellis ladder, Phys. Rev. B **100**, 245118 (2019).
[56] K. Sakakida and H. Shimahara, Spin Structures and Phase Diagrams of Extended Spatially Completely Anisotropic Triangular Lattice Antiferromagnets, J. Phys. Soc. Jpn. **86**, 124709 (2017).
[57] M. Azuma, Z. Hiroi, M. Takano, K. Ishida, and Y. Kitaoka, Observation of a Spin Gap in $SrCu_2O_3$ Comprising Spin-$\frac{1}{2}$ Quasi-1D Two-Leg Ladders, Phys. Rev. Lett. **73**, 3463 (1994).
[58] H. Kontani and K. Ueda, Electronic Properties of the Trellis-Lattice Hubbard Model: Pseudogap and Superconductivity, Phys. Rev. Lett. **80**, 5619 (1998).
[59] H. Iwase, M. Isobe, Y. Ueda, and H. Yasuoka, Observation of Spin Gap in CaV_2O_5 by NMR, J. Phys. Soc. Jpn. **65**, 2397 (1996).
[60] P. Millet, C. Satto, J. Bonvoisin, B. Normand, K. Penc, M. Albrecht, and F. Mila, Magnetic properties of the coupled ladder system MgV_2O_5, Phys. Rev. B **57**, 5005 (1998).
[61] A. A. Tsirlin, R. V. Shpanchenko, E. V. Antipov, C. Bougerol, J. Hadermann, G. Van Tendeloo, W. Schnelle, and H. Rosner, Spin ladder compound $Pb_{0.55}Cd_{0.45}V_2O_5$: Synthesis and investigation, Phys. Rev. B **76**, 104429 (2007).
[62] M. A. Korotin, I. S. Elfimov, V. I. Anisimov, M. Troyer, and D. I. Khomskii, Exchange interactions and magnetic properties of the layered vanadates CaV_2O_5, MgV_2O_5, CaV_3O_7, and CaV_4O_9, Phys. Rev. Lett. **83**, 1387 (1999).
[63] M. A. Korotin, V. I. Anisimov, T. Saha-Dasgupta, and I. Dasgupta, Electronic structure and exchange interactions of the ladder vanadates CaV_2O_5 and MgV_2O_5, J. Phys.: Condens. Matter **12**, 113 (2000).
[64] P. Lemmens, M. Fischer, G. Els, G. Güntherodt, A. S. Mishchenko, M. Weiden, R. Hauptmann, C. Geibel, and F. Steglich, Magnetic bound states in the quarter-filled ladder system $\alpha' - NaV_2O_5$, Phys. Rev. B **58**, 14159 (1998).
[65] M. J. Konstantinović, Z. V. Popović, M. Isobe, and Y. Ueda, Raman scattering from magnetic excitations in the spin-ladder compounds CaV_2O_5 and MgV_2O_5, Phys. Rev. B **61**, 15185 (2000).
[66] Y. Kono, S. Kittaka, H. Yamaguchi, Y. Hosokoshi, and T. Sakakibara, Low Temperature Magnetic Properties of a New Quasi-one-dimensional Organic Magnet α-2-Cl-4-F-V, Phys. Procedia **75**, 679 (2015).
[67] H. Yamaguchi, D. Yoshizawa, T. Kida, M. Hagiwara, A. Matsuo, Y. Kono, T. Sakakibara, Y. Tamekuni, H. Miyagai, and Y. Hosokoshi, Magnetic-field-induced Quantum Phase in $S = 1/2$ Frustrated Trellis Lattice, J. Phys. Soc. Jpn. **87**, 043701 (2018).
[68] G. Misguich, Quantum Spin Liquids and Fractionalization, in *Introduction to Frustrated Magnetism: Materials, Experiments, Theory*, Vol. 164, edited by C. Lacroix, P. Mendels, and F. Mila (Springer, Berlin, Heidelberg, 2011) pp. 407–435.
[69] X.-G. Wen, Quantum orders and symmetric spin liquids, Phys. Rev. B **65**, 165113 (2002).
[70] X.-G. Wen, *Quantum Field Theory of Many-Body Systems: From the Origin of Sound to an Origin of Light and Electrons* (Oxford University Press, 2007).
[71] F. Yang and H. Yao, Frustrated Resonating Valence Bond States in Two Dimensions: Classification and Short-Range Correlations, Phys. Rev. Lett. **109**, 147209 (2012).
[72] X. Yang and F. Wang, Schwinger boson spin-liquid states on square lattice, Phys. Rev. B **94**, 035160 (2016).
[73] F. Wang and A. Vishwanath, Spin-liquid states on the triangular and Kagomé lattices: A projective-symmetry-group analysis of Schwinger boson states, Phys. Rev. B **74**, 174423 (2006).
[74] Y.-M. Lu, Symmetric Z_2 spin liquids and their neighboring phases on triangular lattice, Phys. Rev. B **93**, 165113 (2016).
[75] Y.-M. Lu, Symmetry-protected gapless $\mathbb{Z}_2$ spin liquids, Phys. Rev. B **97**, 094422 (2018).
[76] F. Wang, Schwinger boson mean field theories of spin liquid states on a honeycomb lattice: Projective symmetry group analysis and critical field theory, Phys. Rev. B **82**, 024419 (2010).
[77] Y.-M. Lu and Y. Ran, $\mathbb{Z}_2$ spin liquid and chiral antiferromagnetic phase in the Hubbard model on a honeycomb lattice, Phys. Rev. B **84**, 024420 (2011).
[78] Y.-M. Lu, Y. Ran, and P. A. Lee, $\mathbb{Z}_2$ spin liquids in the $S = \frac{1}{2}$ Heisenberg model on the kagome lattice: A projective symmetry-group study of Schwinger fermion mean-field states, Phys. Rev. B **83**, 224413 (2011).
[79] S. Bieri, L. Messio, B. Bernu, and C. Lhuillier, Gapless chiral spin liquid in a kagome Heisenberg model, Phys. Rev. B **92**, 060407 (2015).
[80] S. Bieri, C. Lhuillier, and L. Messio, Projective symmetry group classification of chiral spin liquids, Phys. Rev. B **93**, 094437 (2016).
[81] T.-P. Choy and Y. B. Kim, Classification of quantum

phases for the star-lattice antiferromagnet via a projective symmetry group analysis, Phys. Rev. B **80**, 064404 (2009).

[82] B.-J. Yang, A. Paramekanti, and Y. B. Kim, Competing quantum paramagnetic ground states of the Heisenberg antiferromagnet on the star lattice, Phys. Rev. B **81**, 134418 (2010).

[83] A. Maity, F. Ferrari, R. Thomale, S. Mandal, and Y. Iqbal, Projective symmetry group classification of Abrikosov fermion mean-field ansätze on the square-octagon lattice, Phys. Rev. B **107**, 134438 (2023).

[84] K. Liu and F. Wang, Schwinger boson symmetric spin liquids of Shastry-Sutherland model, Phys. Rev. B **109**, 134409 (2024).

[85] A. Maity, F. Ferrari, J. Y. Lee, J. Potten, T. Müller, R. Thomale, R. Samajdar, and Y. Iqbal, Evidence for a $\mathbb{Z}_2$ Dirac spin liquid in the generalized Shastry-Sutherland model, (2024), arXiv:2501.00096.

[86] A. Maity, Y. Iqbal, and R. Samajdar, Fermionic parton theory of Rydberg $\mathbb{Z}_2$ quantum spin liquids, (2024), arXiv:2409.17219.

[87] A. Maity, R. Samajdar, and Y. Iqbal, Gapped and gapless quantum spin liquids on the ruby lattice, (2024), arXiv:2409.16344.

[88] Y. Shao, S. Moon, A. N. Rudenko, J. Wang, J. Herzog-Arbeitman, M. Ozerov, D. Graf, Z. Sun, R. Queiroz, S. H. Lee, Y. Zhu, Z. Mao, M. I. Katsnelson, B. A. Bernevig, D. Smirnov, A. J. Millis, and D. N. Basov, Semi-Dirac Fermions in a Topological Metal, Phys. Rev. X **14**, 041057 (2024).

[89] P. Dietl, F. Piéchon, and G. Montambaux, New Magnetic Field Dependence of Landau Levels in a Graphene-like Structure, Phys. Rev. Lett. **100**, 236405 (2008).

[90] S. Banerjee, R. R. P. Singh, V. Pardo, and W. E. Pickett, Tight-Binding Modeling and Low-Energy Behavior of the Semi-Dirac Point, Phys. Rev. Lett. **103**, 016402 (2009).

[91] G. Montambaux, F. Piéchon, J.-N. Fuchs, and M. O. Goerbig, Merging of Dirac points in a two-dimensional crystal, Phys. Rev. B **80**, 153412 (2009).

[92] P. Delplace and G. Montambaux, Semi-Dirac point in the Hofstadter spectrum, Phys. Rev. B **82**, 035438 (2010).

[93] B. Dóra, I. F. Herbut, and R. Moessner, Coupling, merging, and splitting Dirac points by electron-electron interaction, Phys. Rev. B **88**, 075126 (2013).

[94] K. Saha, Photoinduced Chern insulating states in semi-Dirac materials, Phys. Rev. B **94**, 081103 (2016).

[95] B. Roy and M. S. Foster, Quantum Multicriticality near the Dirac-Semimetal to Band-Insulator Critical Point in Two Dimensions: A Controlled Ascent from One Dimension, Phys. Rev. X **8**, 011049 (2018).

[96] M. D. Uryszek, E. Christou, A. Jaefari, F. Krüger, and B. Uchoa, Quantum criticality of semi-Dirac fermions in $2+1$ dimensions, Phys. Rev. B **100**, 155101 (2019).

[97] V. N. Kotov, B. Uchoa, and O. P. Sushkov, Coulomb interactions and renormalization of semi-Dirac fermions near a topological Lifshitz transition, Phys. Rev. B **103**, 045403 (2021).

[98] X. Yuan, C. Zhang, Y. Liu, A. Narayan, C. Song, S. Shen, X. Sui, J. Xu, H. Yu, Z. An, J. Zhao, S. Sanvito, H. Yan, and F. Xiu, Observation of quasi-two-dimensional Dirac fermions in $ZrTe_5$, NPG Asia Mater. **8**, e325 (2016).

[99] M. D. Uryszek, F. Krüger, and E. Christou, Fermionic criticality of anisotropic nodal point semimetals away from the upper critical dimension: Exact exponents to leading order in $\frac{1}{N_f}$, Phys. Rev. Res. **2**, 043265 (2020).

[100] J. Kim, S. S. Baik, S. H. Ryu, Y. Sohn, S. Park, B.-G. Park, J. Denlinger, Y. Yi, H. J. Choi, and K. S. Kim, Observation of tunable band gap and anisotropic Dirac semimetal state in black phosphorus, Science **349**, 723 (2015).

[101] J. Kim, S. S. Baik, S. W. Jung, Y. Sohn, S. H. Ryu, H. J. Choi, B.-J. Yang, and K. S. Kim, Two-Dimensional Dirac Fermions Protected by Space-Time Inversion Symmetry in Black Phosphorus, Phys. Rev. Lett. **119**, 226801 (2017).

[102] A. N. Rudenko, S. Yuan, and M. I. Katsnelson, Toward a realistic description of multilayer black phosphorus: From *GW* approximation to large-scale tight-binding simulations, Phys. Rev. B **92**, 085419 (2015).

[103] M. Bellec, U. Kuhl, G. Montambaux, and F. Mortessagne, Topological Transition of Dirac Points in a Microwave Experiment, Phys. Rev. Lett. **110**, 033902 (2013).

[104] M. C. Rechtsman, Y. Plotnik, J. M. Zeuner, D. Song, Z. Chen, A. Szameit, and M. Segev, Topological Creation and Destruction of Edge States in Photonic Graphene, Phys. Rev. Lett. **111**, 103901 (2013).

[105] B. Real, O. Jamadi, M. Milićević, N. Pernet, P. St-Jean, T. Ozawa, G. Montambaux, I. Sagnes, A. Lemaître, L. Le Gratiet, A. Harouri, S. Ravets, J. Bloch, and A. Amo, Semi-Dirac Transport and Anisotropic Localization in Polariton Honeycomb Lattices, Phys. Rev. Lett. **125**, 186601 (2020).

[106] W.-Y. He and P. A. Lee, Electronic density of states of a U(1) quantum spin liquid with spinon Fermi surface. I. Orbital magnetic field effects, Phys. Rev. B **107**, 195155 (2023).

[107] Y. Xu, J. Zhang, Y. S. Li, Y. J. Yu, X. C. Hong, Q. M. Zhang, and S. Y. Li, Absence of Magnetic Thermal Conductivity in the Quantum Spin-Liquid Candidate $YbMgGaO_4$, Phys. Rev. Lett. **117**, 267202 (2016).

[108] P. Bourgeois-Hope, F. Laliberté, E. Lefrançois, G. Grissonnanche, S. R. de Cotret, R. Gordon, S. Kitou, H. Sawa, H. Cui, R. Kato, L. Taillefer, and N. Doiron-Leyraud, Thermal Conductivity of the Quantum Spin Liquid Candidate $EtMe_3Sb[Pd(dmit)_2]_2$: No Evidence of Mobile Gapless Excitations, Phys. Rev. X **9**, 041051 (2019).

[109] M. Yamashita, N. Nakata, Y. Senshu, M. Nagata, H. M. Yamamoto, R. Kato, T. Shibauchi, and Y. Matsuda, Highly Mobile Gapless Excitations in a Two-Dimensional Candidate Quantum Spin Liquid, Science **328**, 1246 (2010).

[110] G. Baskaran and P. W. Anderson, Gauge theory of high-temperature superconductors and strongly correlated Fermi systems, Phys. Rev. B **37**, 580 (1988).

[111] A. A. Abrikosov, Electron scattering on magnetic impurities in metals and anomalous resistivity effects, Phys. Phys. Fiz. **2**, 5 (1965).

[112] Y.-Z. You, I. Kimchi, and A. Vishwanath, Doping a spin-orbit Mott insulator: Topological superconductiv-

ity from the Kitaev-Heisenberg model and possible application to $(Na_2/Li_2)IrO_3$, Phys. Rev. B **86**, 085145 (2012).
[113] M. Hermele, Y. Ran, P. A. Lee, and X.-G. Wen, Properties of an algebraic spin liquid on the kagome lattice, Phys. Rev. B **77**, 224413 (2008).
[114] C. Zhong, Y. Chen, Y. Xie, Y.-Y. Sun, and S. Zhang, Semi-Dirac semimetal in silicene oxide, Phys. Chem. Chem. Phys. **19**, 3820 (2017).
[115] M. A. J. Herrera and D. Bercioux, Tunable Dirac points in a two-dimensional non-symmorphic wallpaper group lattice, Commun. Phys. **6**, 42 (2023).
[116] H. Hu and F. Krüger, Nature of Topological Phase Transition of Kitaev Quantum Spin Liquids, Phys. Rev. Lett. **133**, 146603 (2024).
[117] J. Kruthoff, J. de Boer, J. van Wezel, C. L. Kane, and R.-J. Slager, Topological Classification of Crystalline Insulators through Band Structure Combinatorics, Phys. Rev. X **7**, 041069 (2017).
[118] B. J. Wieder, B. Bradlyn, Z. Wang, J. Cano, Y. Kim, H.-S. D. Kim, A. M. Rappe, C. L. Kane, and B. A. Bernevig, Wallpaper fermions and the nonsymmorphic Dirac insulator, Science **361**, 246 (2018).
[119] A. N. Rudenko and M. I. Katsnelson, Anisotropic effects in two-dimensional materials, 2D Mater. **11**, 042002 (2024).
[120] H. Isobe, B.-J. Yang, A. Chubukov, J. Schmalian, and N. Nagaosa, Emergent Non-Fermi-Liquid at the Quantum Critical Point of a Topological Phase Transition in Two Dimensions, Phys. Rev. Lett. **116**, 076803 (2016).
[121] C. Bena and L. Simon, Dirac point metamorphosis from third-neighbor couplings in graphene and related materials, Phys. Rev. B **83**, 115404 (2011).
[122] M. M. Elsayed and V. N. Kotov, Microscopic lattice model for quartic semi-Dirac fermions in two dimensions, J. Phys. Condens. Matter **37**, 315501 (2025).
[123] S. Katayama, A. Kobayashi, and Y. Suzumura, Pressure-induced zero-gap semiconducting state in organic conductor α-(BEDT-TTF)$_2$I$_3$ salt, J. Phys. Soc. Jpn. **75**, 054705 (2006).
[124] M. Milićević, G. Montambaux, T. Ozawa, O. Jamadi, B. Real, I. Sagnes, A. Lemaître, L. Le Gratiet, A. Harouri, J. Bloch, and A. Amo, Type-III and Tilted Dirac Cones Emerging from Flat Bands in Photonic Orbital Graphene, Phys. Rev. X **9**, 031010 (2019).
[125] O. I. Motrunich, Variational study of triangular lattice spin-1/2 model with ring exchanges and spin liquid state in $\kappa-(ET)_2Cu_2(CN)_3$, Phys. Rev. B **72**, 045105 (2005).
[126] H.-H. Lai and O. I. Motrunich, SU(2)-invariant Majorana spin liquid with stable parton Fermi surfaces in an exactly solvable model, Phys. Rev. B **84**, 085141 (2011).
[127] R. R. Biswas, L. Fu, C. R. Laumann, and S. Sachdev, SU(2)-invariant spin liquids on the triangular lattice with spinful Majorana excitations, Phys. Rev. B **83**, 245131 (2011).
[128] W. Rantner and X.-G. Wen, Spin correlations in the algebraic spin liquid: Implications for high-T_c superconductors, Phys. Rev. B **66**, 144501 (2002).
[129] P. C. Hohenberg and W. F. Brinkman, Sum rules for the frequency spectrum of linear magnetic chains, Phys. Rev. B **10**, 128 (1974).
[130] J. Reuther and R. Thomale, Finite-temperature functional renormalization group for quantum spin systems, Phys. Rev. B **83**, 024402 (2011).
[131] J. Willsher and J. Knolle, Dynamics and stability of U(1) spin liquids beyond mean-field theory: Triangular-lattice J_1-J_2 Heisenberg model, arXiv:2503.13831.
[132] P. Rao, R. Moessner, and J. Knolle, Dynamical response theory of interacting Majorana fermions and its application to generic Kitaev quantum spin liquids in a field, Phys. Rev. B **112**, 024440 (2025).
[133] J. Potten, Y. Iqbal, R. Thomale, and T. Müller, Keldysh pseudofermion functional renormalization group for quantum magnetism, Phys. Rev. B **112**, 235132 (2025).
[134] T. Müller, D. Kiese, N. Niggemann, B. Sbierski, J. Reuther, S. Trebst, R. Thomale, and Y. Iqbal, Pseudo-fermion functional renormalization group for spin models, Rep. Prog. Phys. **87**, 036501 (2024).
[135] S. R. White, Density matrix formulation for quantum renormalization groups, Phys. Rev. Lett. **69**, 2863 (1992).
[136] S. R. White, Density-matrix algorithms for quantum renormalization groups, Phys. Rev. B **48**, 10345 (1993).
[137] U. Schollwöck, The density-matrix renormalization group, Rev. Mod. Phys. **77**, 259 (2005).
[138] S. R. White, Density matrix renormalization group algorithms with a single center site, Phys. Rev. B **72**, 180403 (2005).
[139] H. Yamamoto, T. Sakakura, H. O. Jeschke, N. Kabeya, K. Hayashi, Y. Ishikawa, Y. Fujii, S. Kishimoto, H. Sagayama, K. Shigematsu, M. Azuma, A. Ochiai, Y. Noda, and H. Kimura, Quantum spin fluctuations and hydrogen bond network in the antiferromagnetic natural mineral henmilite, Phys. Rev. Mater. **5**, 104405 (2021).
[140] M. Hering, F. Ferrari, A. Razpopov, I. I. Mazin, R. Valentí, H. O. Jeschke, and J. Reuther, Phase diagram of a distorted kagome antiferromagnet and application to Y-kapellasite, npj Comput. Mater. **8**, 10 (2022).
[141] M. Fujihala, H. O. Jeschke, K. Morita, T. Kuwai, A. Koda, H. Okabe, A. Matsuo, K. Kindo, and S. Mitsuda, Birchite $Cd_2Cu_2(PO_4)_2SO_4{\cdot}5H_2O$ as a model antiferromagnetic spin-1/2 Heisenberg J_1-J_2 chain, Phys. Rev. Mater. **6**, 114408 (2022).
[142] K. Koepernik and H. Eschrig, Full-potential nonorthogonal local-orbital minimum-basis band-structure scheme, Phys. Rev. B **59**, 1743 (1999).
[143] J. P. Perdew, K. Burke, and M. Ernzerhof, Generalized gradient approximation made simple, Phys. Rev. Lett. **77**, 3865 (1996).
[144] A. I. Liechtenstein, V. I. Anisimov, and J. Zaanen, Density-functional theory and strong interactions: Orbital ordering in Mott-Hubbard insulators, Phys. Rev. B **52**, R5467 (1995).
[145] H. O. Jeschke, F. Salvat-Pujol, and R. Valentí, First-principles determination of Heisenberg Hamiltonian parameters for the spin-$\frac{1}{2}$ kagome antiferromagnet $ZnCu_3(OH)_6Cl_2$, Phys. Rev. B **88**, 075106 (2013).
[146] T. Mizokawa and A. Fujimori, Electronic structure and orbital ordering in perovskite-type 3*d* transition-metal oxides studied by Hartree-Fock band-structure calculations, Phys. Rev. B **54**, 5368 (1996).
[147] K. Sparta, A. Löffert, C. Gross, W. Aßmus, and G. Roth, Single crystal X-ray structure analysis of the

spin ladder compounds $SrCu_2O_3$ and $Sr_2Cu_3O_5$ between 300 K and 100 K, Z. Kristallogr. Cryst. Mater. **221**, 782 (2006).
[148] K. Ishida, Y. Kitaoka, K. Asayama, M. Azuma, Z. Hiroi, and M. Takano, Spin Gap Behavior in Ladder-Type of Quasi-One-Dimensional Spin ($S = 1/2$) System $SrCu_2O_3$, J. Phys. Soc. Jpn. **63**, 3222 (1994).
[149] R. Pohle and L. D. C. Jaubert, Curie-law crossover in spin liquids, Phys. Rev. B **108**, 024411 (2023).
[150] M. Troyer, H. Tsunetsugu, and D. Würtz, Thermodynamics and spin gap of the Heisenberg ladder calculated by the look-ahead Lanczos algorithm, Phys. Rev. B **50**, 13515 (1994).
[151] A. W. Sandvik, E. Dagotto, and D. J. Scalapino, Spin dynamics of $SrCu_2O_3$ and the Heisenberg ladder, Phys. Rev. B **53**, R2934 (1996).
[152] D. C. Johnston, Antiferromagnetic exchange in two-leg spin-1/2 ladders, Phys. Rev. B **54**, 13009 (1996).
[153] C. de Graaf, I. de P. R. Moreira, F. Illas, and R. L. Martin, Ab initio study of the magnetic interactions in the spin-ladder compound $SrCu_2O_3$, Phys. Rev. B **60**, 3457 (1999).
[154] B. Lake, A. M. Tsvelik, S. Notbohm, D. Alan Tennant, T. G. Perring, M. Reehuis, C. Sekar, G. Krabbes, and B. Büchner, Confinement of fractional quantum number particles in a condensed-matter system, Nat. Phys. **6**, 50 (2010).
[155] K. P. Schmidt and G. S. Uhrig, Spectral properties of magnetic excitations in cuprate two-leg ladder systems, Mod. Phys. Lett. B **19**, 1179 (2005).
[156] V. Kiryukhin, Y. J. Kim, K. J. Thomas, F. C. Chou, R. W. Erwin, Q. Huang, M. A. Kastner, and R. J. Birgeneau, Magnetic properties of the $S = \frac{1}{2}$ quasi-one-dimensional antiferromagnet $CaCu_2O_3$, Phys. Rev. B **63**, 144418 (2001).
[157] C. J. Calzado, C. de Graaf, E. Bordas, R. Caballol, and J.-P. Malrieu, Four-spin cyclic exchange in spin ladder cuprates, Phys. Rev. B **67**, 132409 (2003).
[158] E. Bordas, C. de Graaf, R. Caballol, and C. J. Calzado, Electronic structure of $CaCu_2O_3$: Spin ladder versus one-dimensional spin chain, Phys. Rev. B **71**, 045108 (2005).
[159] P. Millet, C. Satto, P. Sciau, and J. Galy, MgV_2O_5 and $\delta Li_xV_2O_5$: A Comparative Structural Investigation, J. Solid State Chem. **136**, 56 (1998).
[160] M. Onoda and N. Nishiguchi, LETTER TO THE EDITOR: Crystal Structure and Spin Gap State of CaV_2O_5, J. Solid State Chem. **127**, 359 (1996).
[161] H.-J. Koo and M.-H. Whangbo, Analysis of the spin–spin interactions in layered oxides α'-NaV_2O_5, CaV_2O_5 and MgV_2O_5 and the spin-Peierls distortion in α'-NaV_2O_5 by molecular orbital, Madelung energy and bond valence sum calculations, Solid State Commun. **111**, 353 (1999).
[162] C. de Graaf, L. Hozoi, and R. Broer, Magnetic interactions in calcium and sodium ladder vanadates, J. Chem. Phys. **120**, 961 (2004).
[163] X. Ming, X.-L. Wang, J.-W. Yin, C.-Z. Wang, Z.-F. Huang, and G. Chen, Electronic structure and magnetic coupling in CaV_2O_5: spin dimer versus spin ladder, Eur. Phys. J. B **75**, 179 (2010).
[164] S. Notbohm, P. Ribeiro, B. Lake, D. A. Tennant, K. P. Schmidt, G. S. Uhrig, C. Hess, R. Klingeler, G. Behr, B. Büchner, M. Reehuis, R. I. Bewley, C. D. Frost, P. Manuel, and R. S. Eccleston, One- and Two-Triplon Spectra of a Cuprate Ladder, Phys. Rev. Lett. **98**, 027403 (2007).
[165] Z. Hiroi, M. Azuma, M. Takano, and Y. Bando, A new homologous series $Sr_{n-1}Cu_{n+1}O_{2n}$ found in the SrO-CuO system treated under high pressure, J. Solid State Chem. **95**, 230 (1991).
[166] M. Azuma, M. Takano, and R. S. Eccleston, Disappearance of the Spin Gap in a Zn-Doped 2-Leg Ladder Compound $Sr(Cu_{1-x}Zn_x)_2O_3$, J. Phys. Soc. Jpn. **67**, 740 (1998).
[167] J. Reuther and P. Wölfle, J_1-J_2 frustrated two-dimensional Heisenberg model: Random phase approximation and functional renormalization group, Phys. Rev. B **81**, 144410 (2010).
[168] F. Ferrari and F. Becca, Dynamical Structure Factor of the J_1-J_2 Heisenberg Model on the Triangular Lattice: Magnons, Spinons, and Gauge Fields, Phys. Rev. X **9**, 031026 (2019).
[169] D. Kiese, F. Ferrari, N. Astrakhantsev, N. Niggemann, P. Ghosh, T. Müller, R. Thomale, T. Neupert, J. Reuther, M. J. P. Gingras, S. Trebst, and Y. Iqbal, Pinch-points to half-moons and up in the stars: The kagome skymap, Phys. Rev. Res. **5**, L012025 (2023).
[170] F. Ferrari, S. Niu, J. Hasik, Y. Iqbal, D. Poilblanc, and F. Becca, Static and dynamical signatures of Dzyaloshinskii-Moriya interactions in the Heisenberg model on the kagome lattice, SciPost Phys. **14**, 139 (2023).
[171] N. Niggemann, Y. Iqbal, and J. Reuther, Quantum Effects on Unconventional Pinch Point Singularities, Phys. Rev. Lett. **130**, 196601 (2023).
[172] Y. Iqbal, F. Becca, and D. Poilblanc, Projected wave function study of $\mathbb{Z}_2$ spin liquids on the kagome lattice for the spin-$\frac{1}{2}$ quantum Heisenberg antiferromagnet, Phys. Rev. B **84**, 020407 (2011).
[173] Y. Iqbal, D. Poilblanc, R. Thomale, and F. Becca, Persistence of the gapless spin liquid in the breathing kagome Heisenberg antiferromagnet, Phys. Rev. B **97**, 115127 (2018).
[174] Y. Iqbal, F. Ferrari, A. Chauhan, A. Parola, D. Poilblanc, and F. Becca, Gutzwiller projected states for the $J_1 - J_2$ Heisenberg model on the Kagome lattice: Achievements and pitfalls, Phys. Rev. B **104**, 144406 (2021).
[175] Y. Iqbal, F. Becca, and D. Poilblanc, Valence-bond crystal in the extended kagome spin-$\frac{1}{2}$ quantum Heisenberg antiferromagnet: A variational Monte Carlo approach, Phys. Rev. B **83**, 100404 (2011).
[176] Y. Iqbal, F. Becca, and D. Poilblanc, Valence-bond crystals in the kagome spin-1/2 Heisenberg antiferromagnet: a symmetry classification and projected wave function study, New J. Phys. **14**, 115031 (2012).
[177] S. Budaraju, Y. Iqbal, F. Becca, and D. Poilblanc, Piercing the Dirac spin liquid: From a single monopole to chiral states, Phys. Rev. B **108**, L201116 (2023).
[178] S. Budaraju, A. Parola, Y. Iqbal, F. Becca, and D. Poilblanc, Monopole excitations in the $U(1)$ Dirac spin liquid on the triangular lattice, Phys. Rev. B **111**, 125150 (2025).

[179] M. M. Elsayed, B. Uchoa, and V. N. Kotov, Coulomb interactions in systems of generalized semi-Dirac fermions, Phys. Rev. B **111**, 165127 (2025).

[180] F. Ferrari, A. Parola, and F. Becca, Gapless spin liquids in disguise, Phys. Rev. B **103**, 195140 (2021).

[181] H. S. Kim, H.-J. Yang, K. Penc, and S. Lee, Spin liquid landscapes in the kagome lattice: A variational monte carlo study of the chiral heisenberg model and experimental signatures, Phys. Rev. B , (2025).

[182] T. Li, Antiferromagnetic long-range order in the uniform resonating valence bond state on the square lattice, EPL **103**, 57002 (2013).

[183] X.-Y. Song, C. Wang, A. Vishwanath, and Y.-C. He, Unifying description of competing orders in two-dimensional quantum magnets, Nat. Commun. **10**, 4254 (2019).

[184] H. Huang, Z. Liu, H. Zhang, W. Duan, and D. Vanderbilt, Emergence of a Chern-insulating state from a semi-Dirac dispersion, Phys. Rev. B **92**, 161115 (2015).

[185] J.-M. Hou, Hidden-Symmetry-Protected Topological Semimetals on a Square Lattice, Phys. Rev. Lett. **111**, 130403 (2013).

[186] J.-M. Hou and W. Chen, Hidden symmetry and protection of Dirac points on the honeycomb lattice, Sci. Rep. **5**, 17571 (2015).

[187] A. Das, R. K. Kaul, and G. Murthy, Stability of zero-energy Dirac touchings in the honeycomb Hofstadter problem, Phys. Rev. B **101**, 165416 (2020).

[188] F. Dusel, T. Hofmann, A. Maity, R. Mosseri, J. Vidal, Y. Iqbal, M. Greiter, and R. Thomale, Chiral Gapless Spin Liquid in Hyperbolic Space, Phys. Rev. Lett. **134**, 256604 (2025).

[189] R. Mosseri, Y. Iqbal, R. Vogeler, and J. Vidal, Kitaev model on Hurwitz hyperbolic tilings: A non-Abelian gapped chiral spin liquid, Phys. Rev. B **111**, L060408 (2025).

[190] P. M. Lenggenhager, S. Dey, T. Bzdušek, and J. Maciejko, Hyperbolic Spin Liquids, Phys. Rev. Lett. **135**, 076604 (2025).

[191] J. Vidal and R. Mosseri, Kitaev model in regular hyperbolic tilings, Phys. Rev. B **112**, 195106 (2025).

[192] J.-S. Bernier, C.-H. Chung, Y. B. Kim, and S. Sachdev, Planar pyrochlore antiferromagnet: A large-N analysis, Phys. Rev. B **69**, 214427 (2004).

[193] L. Capriotti and S. Sachdev, Low-Temperature Broken-Symmetry Phases of Spiral Antiferromagnets, Phys. Rev. Lett. **93**, 257206 (2004).

[194] M. Bintz, V. S. Liu, J. Hauschild, A. Khalifa, S. Chatterjee, M. P. Zaletel, and N. Y. Yao, Dirac spin liquid in quantum dipole arrays, arXiv:2406.00098.

[195] M. Tian, R. Samajdar, and B. Gadway, Engineering Frustrated Rydberg Spin Models by Graphical Floquet Modulation, Phys. Rev. Lett. **135**, 253001 (2025).

[196] G. Semeghini, H. Levine, A. Keesling, S. Ebadi, T. T. Wang, D. Bluvstein, R. Verresen, H. Pichler, M. Kalinowski, R. Samajdar, A. Omran, S. Sachdev, A. Vishwanath, M. Greiner, V. Vuletić, and M. D. Lukin, Probing topological spin liquids on a programmable quantum simulator, Science **374**, 1242 (2021).

[197] Y. Teng, R. Samajdar, K. Van Kirk, F. Wilde, S. Sachdev, J. Eisert, R. Sweke, and K. Najafi, Learning Topological States from Randomized Measurements Using Variational Tensor-Network Tomography, PRX Quantum **6**, 040303 (2025).

[198] R. Ott, T. V. Zache, N. Maskara, M. D. Lukin, P. Zoller, and H. Pichler, Probing Topological Entanglement on Large Scales, Phys. Rev. Lett. **135**, 090401 (2025).

[199] M. Fishman, S. R. White, and E. M. Stoudenmire, The ITensor Software Library for Tensor Network Calculations, SciPost Phys. Codebases , 4 (2022).